

## REVIEW

[View Article Online](#)  
[View Journal](#) | [View Issue](#)




Cite this: *Mater. Horiz.*, 2025,  
12, 5594

Received 22nd February 2025,  
Accepted 28th April 2025

DOI: 10.1039/d5mh00323g

[rsc.li/materials-horizons](https://rsc.li/materials-horizons)

# Recent advances in atomic layer deposition of superconducting thin films: a review

Getnet Kacha Deyu, <sup>a</sup> Marc Wenskat, <sup>ab</sup> Isabel González Díaz-Palacio,<sup>ac</sup>  
Robert H. Blick,<sup>c</sup> Robert Zierold <sup>c</sup> and Wolfgang Hillert <sup>a</sup>

The development of superconducting thin films has opened new avenues in electronic and quantum technologies, offering potential breakthroughs in performance due to their unique properties such as zero electrical DC resistance and perfect diamagnetism. Atomic layer deposition (ALD) stands out as a highly precise and uniform technique for fabricating these films based on sequential, and self-limiting gas-solid surface reactions, offering distinct advantages over other deposition methods. This review explores the role of ALD in the production of superconducting thin films, highlighting its ability to control film thickness at the atomic level, ensuring superior uniformity and conformality. The fundamentals of superconductors and the ALD process are discussed, along with a review of various materials used in the field. It also examines the existing and potential applications of these films and considers future prospects and challenges in the field.

## Wider impact

This article is expected to generate significant interest within the materials science community due to the rising focus on atomic layer deposition (ALD) as a precise method for fabricating superconducting thin films. ALD's ability to deposit films with atomic-scale precision enables unparalleled control over microstructure, which is critical for optimizing superconducting properties. Recent advancements have demonstrated ALD's potential for improving film uniformity, interface quality, and composition control, making it a transformative tool for applications in quantum computing and high-frequency electronics. Additionally, ALD's scalability and ability to coat complex geometries distinguish it from other deposition techniques, positioning it as a key enabler for the large-scale manufacturing of superconducting devices. Despite the growing research in this field, a comprehensive review on ALD for superconducting films is still lacking. This work fills that gap by providing a detailed overview of superconducting ALD processes, recent breakthroughs, and emerging applications. It also identifies critical challenges, such as material selection, deposition conditions, and integration with device architectures. By outlining future research directions, this review serves as a valuable resource for both academia and industry, guiding efforts toward next-generation superconducting technologies and shaping the future of materials science through ALD-driven innovations.

## 1 Introduction

### 1.1 Quest for thin film superconductors

Superconducting materials exhibit extraordinary electrical and magnetic properties that make them ideal for various high-performance applications, including quantum computing, magnetic sensing, advanced electronics and particle accelerators (cavities and magnets) or medical diagnostics (magnetic resonance imaging-MRI). The development of thin film superconductors aims to harness these properties in compact, scalable

formats suitable for integration into various devices. Thin films enable the exploration of new superconducting phenomena and improve device performance by reducing size and weight while preserving or enhancing superconducting properties. Additionally, thin films offer advantages such as flexibility, reduced material usage, and easier integration into complex circuits. However, this pursuit is not without its challenges. As the thickness of a superconducting film decreases, it becomes increasingly difficult to maintain its critical temperature—the point at which the material becomes superconducting. Defects, impurities, and grain boundaries in the thin films can disrupt the superconducting state. Furthermore, the interaction between the film and its substrate can cause strain and alter the materials electronic properties, complicating the preservation of superconductivity.

Despite these challenges, thin film superconductors have found critical applications in various advanced technologies.

<sup>a</sup> Institute of Experimental Physics, Universität Hamburg, Luruper Chaussee 149, D-22761, Hamburg, Germany. E-mail: [getnet.kacha.deyu@desy.de](mailto:getnet.kacha.deyu@desy.de)

<sup>b</sup> Deutsches Elektronen-Synchrotron DESY, Notkestrasse 85 D-22607, Hamburg, Germany

<sup>c</sup> Institute for Nanostructure and Solid State Physics & Center for Hybrid Nanostructures, Universität Hamburg, Luruper Chaussee 149, D-22761, Hamburg, Germany



They are essential in the fabrication of superconducting quantum interference devices (SQUIDs),<sup>1</sup> which are used in highly sensitive magnetometers. In quantum computing, thin film superconductors are used to create qubits,<sup>2–4</sup> the fundamental units of quantum information. These films are also employed in high-performance microelectronics,<sup>5</sup> where they enable faster and more efficient components.

Recent advancements have focused on finding new materials that can sustain superconductivity at higher temperatures and in thinner films. In parallel, significant efforts are being directed towards enhancing the scalability and robustness of thin film superconductors, with proper fabrication techniques playing a crucial role in achieving these goals.<sup>6</sup> Although challenges persist, the progress made to date has already driven significant advancements across various high-tech industries. As research continues, thin film superconductors are set to become integral to the future of quantum computing, energy-efficient technologies, medical imaging, and more.

## 1.2 Significance of fabrication techniques

For most current and future applications of materials in advanced technologies, it is essential to fabricate the active material as high-quality thin films or conformal coatings. Conventional physical vapor deposition (PVD) methods are suitable for thicker layers. However, for layers thinner than 50 nm, these methods are not viable due to issues with conformality.<sup>7</sup> While chemical vapor deposition (CVD) has been explored as a solution, challenges such as controlling nucleation, ensuring strong interfacial adhesion of metals to common barrier layers on various substrates, and the toxicity, scarcity, and difficult handling of precursors (the chemical substances that are introduced into the reaction chamber) have limited its success. Atomic layer deposition (ALD), the state-of-the-art thin-film technology, has proven to be superior in overcoming many of these challenges, particularly in advanced

applications. ALD can produce highly conformal thin films that adhere perfectly to even the most complex 3D surface architectures with nanometer precision.<sup>7–9</sup>

Superconducting thin films require precise control over thickness, composition, and uniformity to achieve optimal performance. ALD has become a preferred method because it enables atomic-level precision and excellent conformality, even on complex geometries. Unlike traditional techniques such as sputtering or CVD, ALD allows for controlled material growth at low temperatures, thereby preserving the integrity and superconducting properties of sensitive films.

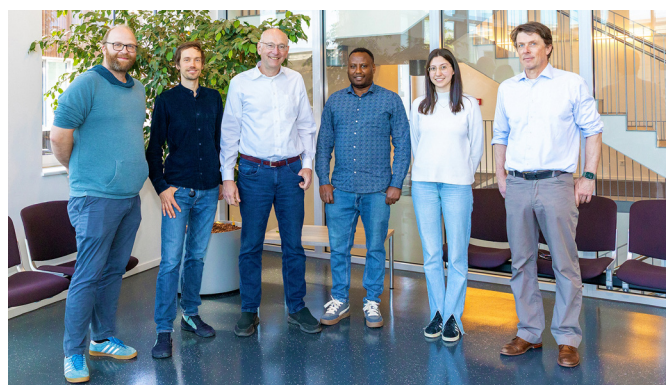
## 1.3 Scope of the review

Despite the growing interest in this topic, there is a lack of comprehensive reviews on the use of ALD for depositing superconducting thin films. This overview seeks to address that gap by presenting the current state of research in the field. It specifically highlights the ALD processes developed for coating various superconducting materials and explores the wide range of applications for these coated films in high-performance environments. Furthermore, this review examines the challenges and future directions in the field, with an emphasis on areas needing further research and development.

# 2 Superconductors in brief

## 2.1 Fundamentals of superconductivity

Superconductivity was first discovered in 1911 by H. Kamerlingh-Onnes while examining materials like mercury, lead, and tin. He found that these materials exhibited vanishing electrical DC resistance below a specific critical temperature, known as  $T_c$ . This discovery came after he successfully liquefied helium and investigated the behavior of electrical resistivity. Kamerlingh-Onnes measured the resistance of a mercury sample as the temperature changed and observed a



Left to right: Marc Wenskat (MW), Robert Zierold (RZ), Wolfgang Hillert (WH), Getnet Kacha Deyu (GD), Isabel González Díaz-Palacio (IP), Robert H. Blick (RB)

partnership not only reflects a strong commitment to scientific excellence but also underscores the critical importance of multidisciplinary collaboration in driving forward technological innovations crucial for the future of high-energy physics and material science research and bringing the methods for fabricating superconducting thin film materials to the next level.

Established in 2018, the collaborative consortium among the Institute of Experimental Physics (IEP–WH, MW, IG, GD) and the Center for Hybrid Nanostructures (CHyN–RB, RZ, IG), both at the University of Hamburg, along with the Deutsches Elektronen-Synchrotron (DESY–MW), targets research into the future of superconducting radio-frequency (SRF) cavities. Making use of the broad expertise in accelerator physics (WH), state-of-the-art SRF cavity design (MW), advanced materials science (GD, IG, RZ), and quantum transport physics (RB), the consortium is well positioned to tackle key challenges in this field. The collaboration, focusing on superconductor–insulator–superconductor structures, utilizes atomic layer deposition to improve cavity performance, with the goal of pushing the limits of next-generation accelerators. The synergy between the University of Hamburg's famous experimental capabilities at IEP and CHyN together with DESY's accelerator facilities enables the group to pioneer advancements. This



sharp drop to a level indistinguishable from zero  $\approx 4$  K. He named this phenomenon superconductivity. In the 1950s, the BCS theory, developed by Bardeen, Cooper, and Schrieffer, provided a comprehensive theoretical framework for classical superconductors. This advancement led to the discovery of numerous elements and compounds that display superconducting properties. In addition to BCS theory, the Ginzburg–Landau Theory and the London equations also contributed to our understanding of superconductivity. While BCS theory is a microscopic model, Ginzburg–Landau offers a more thermodynamic perspective, akin to the Bose–Einstein condensation (BEC) approach. The London equations, originating in the 1930s, represent the earliest theoretical model in this field.<sup>10,11</sup>

**2.1.1 Perfect diamagnetism.** A perfect conductor, when placed in an external direct current (DC) magnetic field  $H_{\text{ext}}$ , demonstrates the ability to prevent magnetic flux from penetrating its interior as long as the temperature remains below the critical temperature ( $T_c$ ). However, if magnetic field lines are present inside the material before it is cooled below  $T_c$ , they become trapped and cannot be expelled. In strong contrast, the Meissner effect, discovered by Meissner and Ochsenfeld in 1933, reveals that superconductors actively expel all magnetic flux from their interior when they transition into the superconducting state.<sup>10–12</sup> This expulsion occurs regardless of whether the magnetic field is applied during cooling or afterward, indicating that superconductors are not merely perfect conductors but represent a distinct thermodynamic phase characterized by the complete exclusion of magnetic fields. This reversible transition allows superconductors to revert to their normal state, enabling magnetic fields to penetrate if conditions change. The schematic of Meissner effect is shown in Fig. 1(a).

### 2.1.2 Theories of superconductivity

**2.1.2.1 London theory.** In 1935, Fritz and Heinz London quantitatively analyzed the ability of superconductors to expel magnetic fields,<sup>13</sup> building on the two-fluid model by Gorter and Casimir.<sup>10,11,14</sup> This model describes how, below the ( $T_c$ ), a fraction of conduction electrons,  $n_s(T)$ , forms a supercurrent

that flows without resistance, while the remaining electrons,  $n - n_s(T)$ , behave as a normal fluid incapable of carrying current without resistance. The Londons showed that the magnetic field does not vanish abruptly at a superconductor's surface but instead decreases exponentially into the bulk, characterized by the London penetration depth,  $\lambda_L$ , which in most pure metals is typically on the order of 10 to 100 nm. The magnetic flux at a distance  $x$  inside the superconductor follows the relationship:

$$B(x) = B_0 \exp\left(-\frac{x}{\lambda_L}\right) \quad (1)$$

with

$$\lambda_L = \sqrt{\frac{mc^2}{4\pi n_s e^2}} \quad (2)$$

where  $m$  is mass of electron and  $e$  is electron charge.

**2.1.2.2 The BCS theory.** In 1957, Bardeen, Cooper, and Schrieffer proposed the BCS theory, providing a microscopic explanation for superconductivity.<sup>15</sup> This theory posits that superconductivity arises from an attractive interaction between electrons near the Fermi surface, mediated by lattice vibrations known as phonons. When electrons traverse a metal, they distort the lattice, generating a positively charged region that attracts another electron, resulting in the formation of a Cooper pair. These pairs form when the energies of two electrons are close to the Fermi energy, within an energy range approximately equal to the Debye energy,  $\hbar\omega_D$ , which corresponds to the typical phonon energy. Acting as bosons, Cooper pairs can occupy the same quantum state, avoiding the restrictions of the Pauli Exclusion Principle. Collectively, these pairs create a ground state where each electron influences the available wave vectors and contributes to the pairing process. The spatial extent of a pair's wave function is known as the coherence length,  $\xi_0$ .

The Cooper pair interaction can be broken by thermal activation, leading to the concept of the superconducting

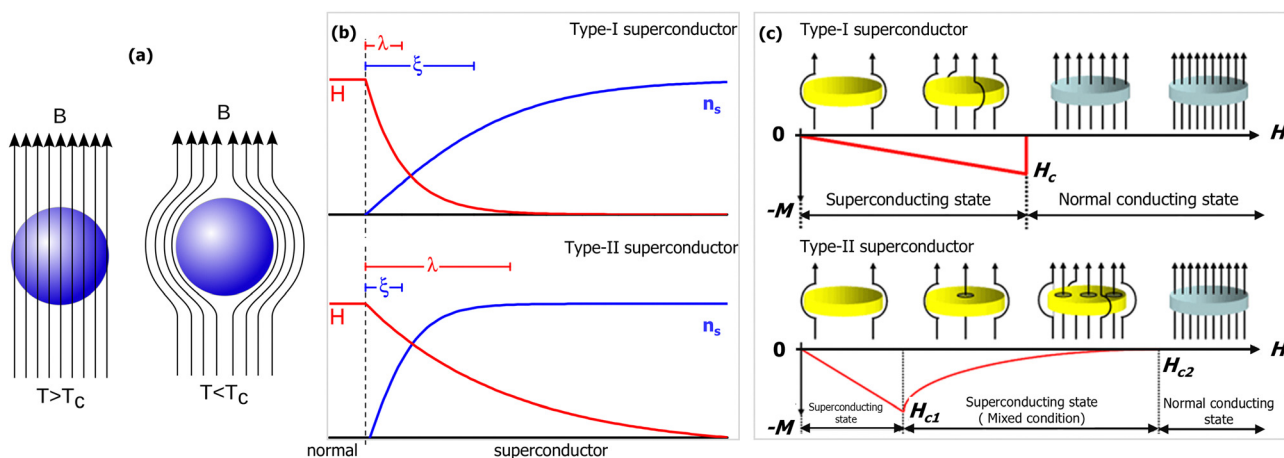


**Fig. 1** (a) Diagram illustrating the Meissner effect, where the blue sphere represents a superconductor. (b) Representation of the coherence length ( $\xi$ ) and penetration depth ( $\lambda$ ) at the boundary between a normal region and a superconducting one for Type I and Type II superconductors. (c) Magnetization as a function of applied field for Type I and Type II superconductors.



energy gap ( $\Delta$ ). This gap represents the energy required to restore a superconducting electron to its normal state and is expressed at  $T = 0$  as:

$$\frac{\Delta(0)}{k_B T_c} = 1.76 \quad (3)$$

where  $k_B$  is the Boltzmann constant. The energy gap is maximum at  $T = 0$  K and becomes zero when  $T$  reaches the critical temperature ( $T_c$ ).

**2.1.3 Classes of superconductors.** Superconductors are classified into two types: Type I and Type II, based on their behavior in a magnetic field and the surface energy at the boundary between superconducting and normal-conducting regions.<sup>10,11</sup>

Type I superconductors such as Pb, Hg, and Zn have a positive surface energy at the boundary, which results in a complete expulsion of magnetic fields (Meissner effect) until a critical field  $H_c$  is reached. Beyond  $H_c$ , they transition abruptly to a normal state, see Fig. 1(b) and (c).

Type II superconductors, such as Nb, TiN, NbN, and NbTiN, have a negative surface energy, making it favorable to form superconducting-normal boundaries. They fully expel the magnetic field up to a lower critical field  $H_{c1}$ , then enter a mixed state where magnetic flux vortices form. The density of these vortices increases until the superconducting state is destroyed at the upper critical field  $H_{c2}$ , see Fig. 1(c).

**2.1.3.1 Ginzburg–Landau parameter.** Ginzburg–Landau Theory gives a quantitative description of superconductors near the transition point.<sup>10,11</sup> A superconductor type is defined by the Ginzburg–Landau (GL) parameter  $\kappa$  as:

$$\kappa = \frac{\lambda_L}{\xi_0} \quad (4)$$

The distinction between the two types of superconductors is as follow:

$$\begin{aligned} \kappa &< \frac{1}{\sqrt{2}} && \text{Type I} \\ \kappa &> \frac{1}{\sqrt{2}} && \text{Type II} \end{aligned} \quad (5)$$

The schematics of surface energy for Type I and Type II superconductors is shown in Fig. 1(b).

**2.1.3.2 Critical fields.** The elementary BCS prediction for the temperature dependence of  $\mathcal{H}_c(\mathcal{T})$  is often expressed by using the empirical formula:

$$\frac{H_c(T)}{H_c(0)} = 1 - \left(\frac{T}{T_c}\right)^2 \quad (6)$$

Eqn (6) is valid for temperatures in the range of  $0 \leq T \leq T_c$ .

**2.1.4 Superconductivity in the radio-frequency domain.** The radio frequency (RF) superconductivity refers to the phenomenon where superconducting materials are used to sustain and enhance RF electromagnetic fields with minimal energy loss.<sup>10,11</sup> The RF response of superconductors is characterized by near-zero electrical resistance and perfect diamagnetism (Meissner effect), making them ideal for high-frequency

applications. In the superconducting state, RF currents flow without dissipation due to Cooper pairs, which experience negligible resistance. However, at finite frequencies, surface resistance arises from residual normal electrons and weak quasiparticle excitations, increasing with frequency and temperature. The RF frequency range for different superconducting applications varies: superconducting radio frequency (SRF) cavities operate in the MHz–GHz range (e.g.,  $\approx 1.3$  GHz for particle accelerators), quantum computing resonators typically work in the GHz range (4–8 GHz), and telecommunications filters extend into tens of GHz.

**2.1.4.1 Surface resistance.** At temperatures above absolute zero, a fraction of normal electrons remains unpaired, which can potentially dissipate energy if set into motion. In the DC regime, superconductors exhibit zero electrical resistance because Cooper pairs fully take over charge transport. However, in the RF regime, a time-varying electric field is present, which forces both normal electrons and Cooper pairs into oscillatory motion. As normal electrons move, they contribute a non-zero resistance to the material. As this movement is confined in a thin surface layer (skin effect) the according resistance is called surface resistance ( $R_s$ ) and consists of two main components:

$$R_s = R_{\text{BCS}}(T) + R_{\text{res}} \quad (7)$$

The BCS surface resistance ( $R_{\text{BCS}}$ ) turns out to be a temperature and frequency dependent. In contrast, the residual surface resistance ( $R_{\text{res}}$ ) is temperature-independent and arises from parasitic losses, though its precise origin remains unclear. Both intrinsic factors—such as non-ideal surface quality, metallic inclusions, surface oxides, and grain boundaries—and accidental mechanisms, like particulates, chemical residues, or surface defects, contribute to these losses. Additionally, extrinsic factors, such as flux trapped during cooling, play a role. Given the diversity of contributing phenomena,  $R_{\text{res}}$  cannot be predicted with a single formula. However, empirical studies suggest that  $R_{\text{res}}$  is at least proportional to  $r_n$ , the normal-state resistance. Between two materials with identical BCS resistance, the one with a lower  $r_n$  typically exhibits smaller residual resistance.

**2.1.4.2 Residual resistivity ratio (RRR).** Is a key measure of metal purity, which is expressed as the ratio of electrical resistivity at 295 K to that at 0 K. For SRF cavities, a minimum RRR of 200 is required, while high-gradient cavities typically have an RRR of 300.<sup>16</sup> Impurities such as oxygen, nitrogen, hydrogen, and carbon (O, N, H, C) act as scattering centers for conduction electrons, reducing RRR and thermal conductivity.<sup>17</sup>

## 3 Atomic layer deposition

### 3.1 Fundamentals

Atomic layer deposition (ALD) is a vapor-phase deposition technique renowned for its capability to synthesize ultra-thin films. These films are typically grown sub-monolayer by sub-monolayer, achieved through the repeated execution of two distinct half-reactions.<sup>8,18–25</sup> The principles of ALD can be





illustrated by considering the deposition of superconducting TiN, as shown in the schematics of Fig. 2. In a typical ALD process, alternating pulses of gaseous chemical precursors react with the substrate surface in a sequential manner. For instance for TiN deposition, this can be achieved using either thermal or plasma-enhanced ALD (PEALD) systems. In thermal ALD,  $\text{TiCl}_4$  and  $\text{NH}_3$  are the common precursors,<sup>5,26</sup> whereas in PEALD,  $\text{TiCl}_4$  is combined with  $\text{H}_2/\text{N}_2$ -plasma.<sup>27</sup> Each precursor pulse introduces a half-reaction, during which the precursor reacts with the substrate in a self-limiting manner, ensuring that only a maximum of monolayer of material per cycle is deposited. After each precursor pulse, the chamber is purged with an inert carrier gas, such as nitrogen ( $\text{N}_2$ ) or argon (Ar), to remove any unreacted precursor or reaction by-products. The process is then repeated with a counter-reactant precursor—such as  $\text{NH}_3$  or  $\text{H}_2/\text{N}_2$ -plasma—in the next half-reaction. This cycle continues until the desired TiN film thickness is achieved.<sup>5,26,27</sup> The self-limiting nature of ALD allows for precise control over film thickness, uniformity, and quality, making it an ideal technique for growing materials.<sup>8,18–25</sup> However, the process faces challenges due to steric and electrostatic hindrance from ligands, particularly those associated with the chemisorbed first reactant. This hindrance can shield portions of the surface, limiting accessibility for the second reactant. As a result, the growth per cycle (GPC) in ALD, especially when using compound reactants like those examined in this review, is often significantly less than a full monolayer. Experimental GPC values exhibit variability up to 30% of a monolayer, contingent upon the growth temperature.<sup>19,28</sup> Despite these challenges, ALD technology offers the possibility to prepare thin films of high quality materials with no line-of-sight deposition, precise thickness control, high uniformity, and excellent conformality.

ALD processes are usually conducted at moderate temperatures (below 350 °C).<sup>25</sup> The specific temperature range where

growth is saturated is known as the “ALD temperature window” and varies depending on the process.<sup>19</sup> Operating outside of this window can lead to poor growth rates and non-ALD-type deposition due to issues such as slow reaction kinetics or precursor condensation at low temperatures, and thermal decomposition or rapid desorption of the precursor at high temperatures. To maximize the advantages of ALD, it is crucial to operate within the designated ALD temperature window for each deposition process.<sup>19,25</sup>

### 3.2 Types of ALD

In general, when selecting an ALD process for depositing superconducting thin films, several critical criteria must be considered to achieve optimal performance. The material composition is paramount, as the superconducting properties depend on precise stoichiometry and phase purity, which necessitates the use of carefully chosen precursors that can deliver the desired elements in the correct ratios. Temperature control is crucial since the deposition temperature must be low enough to prevent degradation of the superconducting properties while still allowing for sufficient surface reactions. Additionally, film uniformity and conformality are essential, particularly for applications in microelectronics or quantum devices, where even slight variations in thickness can significantly impact device performance.<sup>29</sup> The substrate compatibility is another key factor, as the substrate must not only withstand the deposition process but also have to ensure surface group termination. This surface termination is vital for enabling the self-limiting reactions that characterize ALD, ensuring uniform and controlled film growth. Finally, process throughput and scalability are important for commercial applications, where consistent and high-quality films need to be produced efficiently. Balancing these factors is essential to selecting the most suitable ALD process for superconducting thin films.

There are several types of ALD processes, each optimized for different applications and materials. Below are some commonly used ALD methods, as well as others that show potential for application in the field of superconductivity, along with brief descriptions. The primary properties and superconducting materials deposited by these ALD techniques are summarized in Fig. 3.

**3.2.1 Thermal ALD.** Relies on heat to facilitate the chemical reactions between gaseous precursors and the substrate surface. This method is relatively straightforward because it does not require additional equipment, such as plasma generators. Thermal ALD provides excellent step coverage and conformality on complex geometries and is suitable for depositing a wide range of materials, including oxides, nitrides, and metals.<sup>8,9,19,21,23,24</sup> However, it has some limitations, such as the need for higher temperatures, which might not be ideal for temperature-sensitive substrates. Additionally, some precursors may not react efficiently at lower temperatures. Several superconducting thin films including TiN,<sup>5</sup> NbN,<sup>30,31</sup> NbSi,<sup>31</sup> NbC,<sup>31,32</sup> NbTiN,<sup>33,34</sup> CuO,<sup>35</sup> MoN,<sup>33</sup> and MoC,<sup>36</sup> have been deposited using this technique. However, these films typically exhibit lower superconducting transition temperatures compared to those deposited using other methods.

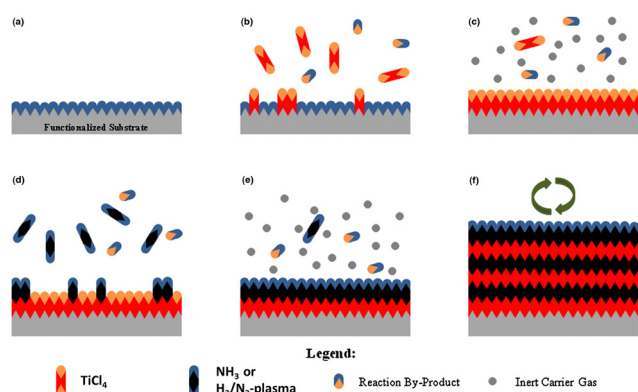


Fig. 2 Schematic of ALD process for superconducting TiN films. (a) Substrate surface has natural functionalization or is treated to functionalize the surface. (b) Precursor A ( $\text{TiCl}_4$ ) is pulsed and reacts with surface. (c) Excess precursor and reaction by-products are purged with inert carrier gas. (d) Precursor B ( $\text{NH}_3$  or  $\text{H}_2/\text{N}_2$ -plasma) is pulsed and reacts with surface. (e) Excess precursor and reaction by-products are purged with inert carrier gas. (f) Steps 2–5 are repeated until the desired material thickness is achieved. Adopted from ref. 25. Copyright 2014, Elsevier Publishing.



ALD Process Type	Uniformity & Conformality	Substrate Compatibility	Process Throughput & Scalability	Coating superconducting films		
				Advantage	Disadvantage	Materials
Thermal ALD	★★★★	● Robust substrates	⌚ Moderate	✓ Excellent coverage on complex shapes	✗ High temp. can degrade sensitive materials	TiN, NbN, NbSi, NbC, NbTiN, CuO, MoN, MoC
Plasma Enhanced ALD (PEALD)	★★★	● Temperature-sensitive	⌚ Moderate	✓ Low-temp. deposition	✗ Plasma may damage substrates	TiN, NbN, NbTiN, MoCN, TaCN, LaSrCuO
Spatial ALD	★★	● Large-area substrates	🚀 High	✓ Ideal for large-scale production	✗ Lower film thickness control	-
Hot-Wire ALD (HWALD)	★★	● Temperature-sensitive	⌚ Moderate	✓ Low-temp, good for sensitive materials	✗ Risk of wire contamination	-
Area-Selective ALD (ASALD)	★★★★	● Complex geometries/patterns	🚚 Low	✓ High-resolution patterning, multi-layering	✗ Complex, costly, preparation intensive	-

Fig. 3 Comparison of main ALD process types, evaluated for coating uniformity and conformality, substrate compatibility, process throughput, and scalability. The table also outlines the advantages and disadvantages of each method and the reported materials of superconducting thin films. Star ratings (2, 3, and 4 stars) denote moderate, good, and excellent film uniformity and conformality, respectively.

**3.2.2 PEALD-plasma enhanced-ALD.** Uses plasma to increase the chemical reactivity of precursors, enabling deposition at lower temperatures than thermal ALD. This technique is suitable for depositing materials on temperature-sensitive substrates such as polymers and certain metals. By enhancing precursor reactivity, plasma potentially broadens the range of materials that can be used.<sup>20,37</sup> However, PEALD requires additional equipment and precise control over plasma parameters. Moreover, the plasma can potentially damage sensitive substrates or underlying layers. A wide variety of superconducting thin films, including complex materials with higher superconducting transition temperatures ( $T_c$ ) than those achieved with thermal ALD, have been reported using this method.<sup>38–42</sup>

**3.2.3 Spatial ALD.** Involves moving the substrate through distinct zones where it is exposed to separate precursors, allowing for continuous processing and high throughput.<sup>43</sup> This method can process large areas quickly, making it well-suited for industrial-scale applications. The continuous processing feature reduces cycle times and increases throughput. Nevertheless, it requires precise control over substrate movement and the separation of precursor zones. Additionally, it may offer less control over film thickness compared to conventional ALD.

**3.2.4 Hot-wire ALD-HWALD.** Employs a heated wire to decompose precursors into reactive species, enabling low-temperature deposition. This approach is ideal for substrates that are sensitive to high temperatures.<sup>44</sup> The heated wire enhances the decomposition and reactivity of the precursors. However, there is a risk of contamination from the heated wire. Additionally, this method requires extra hardware to heat and control the wire effectively.

**3.2.5 Area-selective atomic layer deposition-ASALD.** Involves precisely controlling the deposition process so that thin films form only on specified regions of a substrate.<sup>45</sup> This selectivity is achieved through various methods, including surface modification, chemical blocking, selective precursors, and patterned substrates. ASALD allows for high-resolution patterning of films, which is crucial for advanced systems. It also supports the creation of complex multi-layer structures with exact control over layer placement, enhancing device efficiency and reliability by preventing deposition on non-active areas.

However, the process requires additional steps and controls to ensure precise patterning and selectivity, which can complicate the procedure and increase costs. Additionally, achieving the desired selectivity often necessitates meticulous surface preparation and treatment, which can be challenging.

### 3.3 Comparison of ALD with other deposition techniques

ALD stands out among thin-film deposition techniques for superconducting materials due to its exceptional uniformity, conformality, and atomic level growth control. Unlike sputtering, arc-PVD, and spin coating, which suffer from poor conformality, ALD ensures a highly uniform and precise coating even on complex surfaces. Compared to CVD and pulsed laser deposition (PLD), which offer good film quality but lower conformality, ALD provides superior thickness control and defect-free layers. While Molecular Beam Epitaxy (MBE) also achieves atomic-level precision and excellent quality, it is significantly more expensive than ALD. In terms of cost, ALD is classified as a high-cost method due to its slow deposition rate, but it remains more affordable than MBE. Sputtering and PLD provide high-quality films at medium-to-high costs, whereas spin coating, dip coating, and spray pyrolysis are low-cost methods that result in lower film quality. Although ALD has a slow deposition rate, its ability to produce high-quality, uniform superconducting films makes it a preferred choice for applications requiring precision and reliability over speed and low-cost production.<sup>46–48</sup> These comparisons are summarized in Table 1.

## 4 ALD of superconductors

### 4.1 General observation

ALD has been successfully used to deposit various superconducting materials. Its capability to precisely control film thickness and composition makes it ideal for exploring the superconducting properties of thin films. However, compared to other deposition techniques, only a limited range of superconducting thin films have been reported using ALD. Generally, ALD can produce films with good superconducting properties, but careful optimization of deposition parameters is essential



**Table 1** Comparison of ALD with other thin film deposition techniques for superconducting materials

Technique	Deposition principle	Growth control	Uniformity	Conformality	Deposition rate	Temp. range (°C)	Cost	Film quality	SF <sup>f</sup>
ALD <sup>a</sup>	Self-limiting surface reactions	Atomic level precision	Excellent	Excellent	Slow	RT-400	High	High	NbN, TiN, MoN <sup>3,30–33</sup>
Sputtering	Plasma based physical deposition	Moderate	Good	Poor	Medium	RT-800	Medium	High	NbN, MgB <sub>2</sub> , Nb <sub>3</sub> Sn <sup>49–51</sup>
CVD <sup>b</sup>	Gas phase chemical reaction	Moderate	Good	Good	High	300–1100	High	High	BSCCO, MgB <sub>2</sub> <sup>52–54</sup>
MBE <sup>c</sup>	Atom by atom deposition in UHV	Atomic level	Excellent	Moderate	Slow	200–800	Very high	Very high	MgB <sub>2</sub> , SrFeAs <sup>55,56</sup>
Spray pyrolysis	Aerosol precursor decomposition	Poor	Poor	Moderate	Medium	200–600	Low	Low-medium	MgB <sub>2</sub> , <sup>57</sup> YBCO <sup>46,58</sup>
Spin coating	Solution based film spreading	Poor	Moderate	Poor	Fast	RT-500	Low	Low	YBCO <sup>59,60</sup>
PLD <sup>d</sup>	Laser ablation of target	Good	Good	Moderate	Medium	300–900	High	High	FeSe/STO, Nb <sup>61,62</sup>
Dip coating	Solution immersion	Poor	Poor	Poor	Fast	RT-300	Low	Low	YBCO <sup>63</sup>
Arc-PVD <sup>e</sup>	Cathodic arc vaporization	Moderate	Moderate	Poor	High	200–800	Medium	High	BSCCO, Pb, Nb <sup>64,65</sup>

<sup>a</sup> ALD – atomic layer deposition. <sup>b</sup> CVD – chemical vapor deposition. <sup>c</sup> MBE – molecular-beam epitaxy. <sup>d</sup> PLD – pulsed laser deposition. <sup>e</sup> Arc-PVD – cathodic arc deposition. <sup>f</sup> SF – selected superconducting films grown by the technique.

to achieve the desired results. This section will discuss and compare various reported ALD superconducting thin films with respect to their superconducting properties.

## 4.2 Superconducting compounds

**4.2.1 Binary nitrides.** Superconducting binary transition metal nitrides are compounds formed between nitrogen and transition metals, known for their remarkable superconducting, mechanical, and thermal properties.<sup>66</sup> These materials exhibit high critical temperatures, exceptional stability, and hardness, with most adopting rock-salt or hexagonal crystal structures. Nitrogen atoms in these superconductors provide strong bonding and large electron–phonon coupling (EPC), resulting in superconductivity. Notable examples include NbN with  $T_c \sim 17$  K,<sup>67,68</sup> VN with  $T_c \sim 10$ –11 K,<sup>69,70</sup> TiN with  $T_c \sim 4$ –5 K,<sup>71</sup> TaN with  $T_c \sim 10$ –12 K,<sup>72–74</sup> MoN with  $T_c \sim 12$ –14 K,<sup>75</sup> and ZrN with  $T_c \sim 10$ –11 K.<sup>76</sup> Of these, superconducting NbN, TiN, and MoN grown by ALD have been reported and will be detailed in the following subsection.

**4.2.1.1 TiN.** There are handful reports on superconducting TiN thin films grown using both thermal and plasma-enhanced ALD.<sup>3,5,27,38,77–79</sup> The choice of precursors, deposition temperatures, film thicknesses, and specific deposition techniques have led to variations in the  $T_c$  of these films. Among these studies, the highest  $T_c$  of 4.62 K for TiN films grown using the ALD process was reported by Shearrow *et al.*<sup>38</sup>

Femi-Oyetoro *et al.*<sup>77</sup> reported a superconducting TiN films grown by PEALD using tetrakis(dimethylamido)titanium (TDMAT) as the precursor and a nitrogen/argon mixture for the plasma step with a deposition temperature of 300 °C. In order to quantify the purity of grown films, they performed Secondary Ion Mass Spectrometer (SIMS) measurement, see Fig. 4(a). SIMS quantify the following impurities, H, C, and O levels of approximately 2.5%, 1%, and 0.3%, respectively. X-ray Photoelectron Spectroscopy (XPS) depth profiling indicated an average Ti:N ratio of 0.95. In addition, they examined the

crystallinity of deposited films by Grazing Incidence-X-ray Diffraction (GI-XRD), see Fig. 4(b). The film show a crystalline structure with a preferred (111) orientation, with a measured lattice constant of 4.283 Å. High-resolution transmission electron microscopy (HRTEM) of an 80 nm TiN film showed columnar grain structures with grain widths up to 60 nm, see Fig. 4(d<sub>a</sub>). X-ray diffraction (XRD) estimated crystallite sizes in various directions as 20 nm, 10 nm, 8 nm, and 7 nm. The overall film exhibited a smooth, multilayer structure, composed of a silicon nitride (SiN<sub>x</sub>) layer, a TiN nucleation layer, and a bulk TiN layer, as observed in the scanning transmission electron microscopy (STEM) image in Fig. 4(d<sub>b</sub>). Furthermore, a 2 nm SiN<sub>x</sub> interface layer was detected between the TiN film and the silicon wafer, which was confirmed through energy-loss spectroscopy (EELS), Fig. 4(d<sub>c–f</sub>) and energy-dispersive spectroscopy (EDS), Fig. 4(d<sub>g</sub>). The formation of this interface layer was linked to the incubation period associated with nitrogen plasma exposure, which likely promotes silicon nitridation, a common phenomenon in nitrogen-based TiN growth processes. Fig. 4(c) compares the  $T_c$  between PEALD and sputtered TiN, with values of 4.35 K and 4.0 K, respectively. They attribute the lower  $T_c$  in their sputtered TiN to surface oxidation, intergranular voids, and a reduced N ratio.<sup>77</sup>

The superconducting TiN films grown by PEALD using TDMAT and N<sub>2</sub> plasma as the precursors, with a deposition temperature of 270 °C on hydrogen-terminated Si substrate, have been reported by Shearrow *et al.*<sup>38</sup> Fig. 4(e), along with Table 2, illustrates the evolution of the  $T_c$  as a function of the number of ALD cycles and corresponding film thickness. The resistivity ( $\rho$ ) plots reveal that films with more ALD cycles, and therefore thicker films, exhibit higher  $T_c$  values. The table provides data extracted from Fig. 4(e), showing that as the film thickness increases from 5.6 nm (62 cycles) to 109 nm (1250 cycles), the  $T_c$  rises from  $\approx 3.01$  K to 4.62 K. The resistivity behavior in the figure matches these trends. This is attributed to disorder enhanced Coulomb repulsions.<sup>80,81</sup> Notably, the thinnest film (62 cycles, 5.6 nm), shown in the bottom plot,





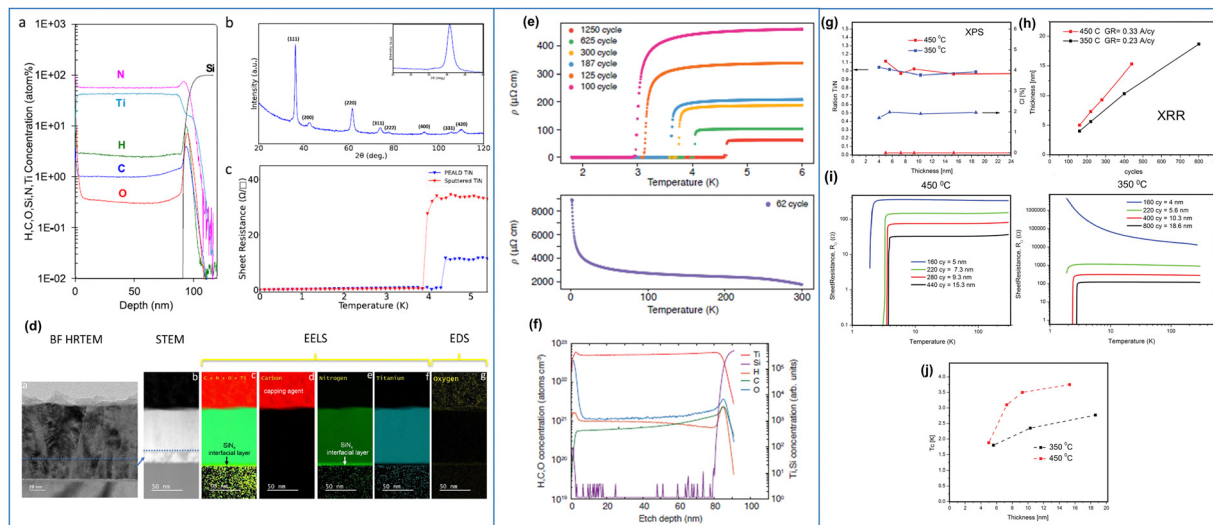


**Fig. 4** TiN films grown by PEALD using TDMAT as the precursor and a nitrogen/argon mixture for the plasma step with a deposition temperature of 300 °C (a) SIMS spectra reveal contamination and composition profiles, displaying atomic concentrations of H, C, O, N, and Ti in an 80 nm PEALD TiN film. The TiN number density (1023 atoms per cc) serves as the basis for conversion to atom% units. (b) GI-XRD scan identifies the phase, with the inset showing the preferential (111) orientation at  $2\theta$  36.5° of an 80 nm PEALD TiN film. (c) Resistance vs. temperature on 40 nm PEALD and sputtered TiN films demonstrates  $T_c$  values of 4.35 and 4.0 K, respectively.<sup>77</sup> Copyright 2011, AIP Publishing. TiN films also grown by PEALD using TDMAT and  $N_2$  plasma as the precursor with a deposition temperature of 270 °C (e) Resistivity as a function of temperature for various TiN film thicknesses given by their quantities of ALD cycles. (f) SIMS of TiN film grown by ALD for 1250 cycles.<sup>38</sup> Copyright 2018, AIP Publishing. TiN films grown via thermal ALD using  $TiCl_4$  and  $NH_3$  precursors with different deposition temperatures. (g) Ti/N atomic ratio and % of Cl contamination measured in XPS, as a function of film thickness. (h) growth rate of films grown at 350 and 450 °C extracted from XRR measurements. (i)  $T_c$  vs. sheet resistance for the films grown at 350 and 450 °C. (j)  $T_c$  vs. film thickness for the films grown at 350 and 450 °C.<sup>26</sup> Copyright 2013, JACOW Publishing.

does not exhibit a clear superconducting transition, reflecting the absence of a measurable  $T_c$ . Nevertheless, other groups<sup>27,80</sup> have reported on the successful fabrication and characterization of superconducting TiN films using ALD, achieving thicknesses below 8.9 nm while maintaining superconducting properties. Additionally, Hossain *et al.*<sup>78</sup> reported slightly lower  $T_c$  of 3.22 K for 60 nm thick TiN film deposited using the same precursors but at elevated deposition temperature of 350 °C, emphasizing the significant role that deposition conditions play in determining the superconducting properties of TiN films.

Additionally, SIMS analysis of a 1250-cycles thick TiN film, as shown in Fig. 4(f), reveals that the concentrations of H, C, and O remain relatively stable, with variations of less than a few percent throughout the entire thickness of the TiN film.<sup>78</sup> This indicates that the impurity levels are consistent across the film, demonstrating a controlled deposition process with minimal fluctuation in impurity content.

**Table 2** Evolution of  $T_c$  as a function of the number of ALD cycles (film thickness) of TiN films, extracted from Fig. 4(e).<sup>38</sup>

Cycles	$d$ (nm)	$T_c$ (K)
62	5.6	—
100	8.9	3.01
125	10.7	3.17
187	14.2	3.63
300	25.79	3.76
625	49.8	4.05
1250	109	4.62

Proslier,<sup>26</sup> reported superconducting TiN films grown by thermal ALD using  $TiCl_4$  and  $NH_3$  precursors. The study compares the properties of TiN films processed at two different temperatures: 350 °C and 450 °C, with characterization performed through DC electrical measurements and X-ray techniques. Fig. 4(g) illustrates the elemental composition of the films grown at different temperatures as a function of film thickness, particularly focusing on the ratio of titanium to nitrogen (Ti/N) and the concentration of chlorine (Cl). The Ti/N ratio, denoted on the left axis, appears to stabilize around 1 for both deposition temperatures. Meanwhile, films deposited at 350 °C show 2% chlorine impurities (denoted on the right axis), while the films deposited at 450 °C show near zero Cl impurity, suggesting that higher temperatures result in films with fewer impurities and a more stable stoichiometric composition. The XRR plot reveals linear growth trend indicating consistent film deposition as cycles increase with growth rates of 0.33 Å per cycle for the films deposited at 450 °C and 0.23 Å per cycle for films grown at 350 °C, see Fig. 4(h). Fig. 4(i) depict the sheet resistance as a function of temperature for films deposited at 450 °C (left) and 350 °C (right). For both temperatures, multiple curves are shown, corresponding to different thicknesses (given by cycle numbers). At 450 °C, thicker films show a sharper decrease in sheet resistance as temperature drops, indicating a clear superconducting transition, while thinner films have higher residual resistance and a more gradual transition. Films grown at 350 °C exhibit higher sheet resistance and a less pronounced superconducting transition, especially for thinner films. Higher deposition temperatures





result in better electrical properties, as shown by lower resistance and sharper transitions at 450 °C. Fig. 4(j) shows  $T_c$  values for both temperatures, with  $T_c$  peaking at intermediate thicknesses before slightly declining. Films deposited at 450 °C exhibit higher  $T_c$  values, reaching a maximum of 3.8 K, compared to 1.6 K (Grigoros *et al.*<sup>79</sup>) and 3.4 K (Jhabvala *et al.*<sup>5</sup>) under similar conditions. Films deposited at 350 °C have a lower  $T_c$  maximum of 2.75 K. This suggests that higher deposition temperatures result in films with superior superconducting properties. In conclusion, higher deposition temperatures (450 °C) produce thicker films with fewer impurities, better compositional control, and enhanced superconducting properties compared to those deposited at 350 °C.

**4.2.1.2 MoN.** Molybdenum nitride (MoN) has garnered attention for its mechanical properties, such as extreme hardness,<sup>82</sup> and the prediction of the cubic B1 phase as a potential high-temperature superconductor with a  $T_c$  of approximately 29 K.<sup>83,84</sup> However, the B1 phase is thermodynamically and mechanically unstable and does not appear on the MoN equilibrium phase diagram.<sup>85,86</sup> Numerous attempts to synthesize a metastable B1 phase through various techniques have resulted in significantly lower  $T_c$  values than predicted.<sup>87,88</sup> This discrepancy is attributed to the presence of nitrogen vacancies and defects, which induce distortions in both the nitrogen and metal sublattices.<sup>89</sup> While theoretical models account for nitrogen vacancies, they often neglect potential distortions in the metal sublattice. MoN can crystallize in several distinct structures, each associated with different superconducting properties: including  $\gamma$ -Mo<sub>2</sub>N (cubic) with  $T_c \sim 5$  K,  $\beta$ -Mo<sub>2</sub>N (tetragonal)  $T_c \sim 5$  K, and  $\delta$ -MoN (hexagonal)  $T_c \sim 12$  K.<sup>90,91</sup> Several studies have explored the deposition of superconducting MoN films using various techniques,<sup>91–93</sup> with only one group reporting on films produced via ALD.<sup>33</sup>

The research conducted by Groll *et al.*,<sup>26,33</sup> offers detailed insights into the fabrication and superconducting properties of MoN thin films grown using thermal ALD. In this process, MoCl<sub>5</sub> and NH<sub>3</sub> were employed as chemical precursors, and the films were deposited at a relatively high temperature of 450 °C. The authors investigated how the structural and superconducting characteristics of MoN films evolved with increasing the number of ALD cycles, which directly correlate with film thickness. Additionally, the study explores the effects of introducing elemental zinc during the ALD process, which offers further insights into material optimization for enhanced film quality.

The XRD analysis reveals a significant improvement in the crystallinity of the MoN films as the number of ALD cycles increases, ranging from 120 to 800 cycles, see Fig. 5 (left). As more cycles are performed, the diffraction peaks in the XRD patterns become sharper and more intense, indicating enhanced structural order. The peaks correspond to the (200) and (002) crystallographic planes, which are indicative of the  $\delta$ -MoN with  $T_c \sim 4$  K and  $\gamma$ -Mo<sub>2</sub>N with  $T_c \sim 12$  K phases, respectively.<sup>26</sup> At higher number of ALD cycles, the films exhibit better-defined phase separation and crystallinity, as evidenced by the intensity and sharpness of the peaks at 800 cycles,

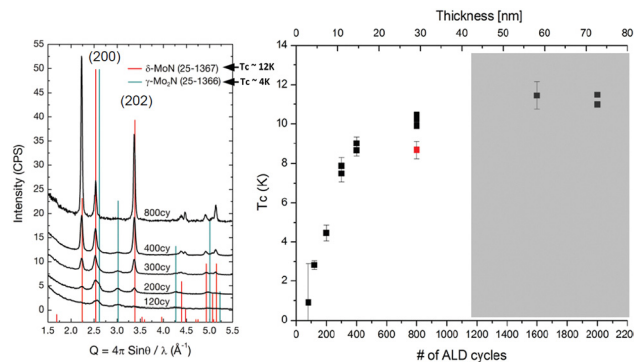


Fig. 5 (left), GIXRD: evolution of structure with thickness for the films deposited at 450 °C (b),  $T_c$  as a function of film thickness and the number of ALD cycles<sup>26,33</sup> Copyright 2013, JACOW Publishing.

suggesting that extended deposition enhances the formation of these phases.<sup>26</sup>

The evolution of  $T_c$  is shown to be closely linked to the film thickness, which increases with the number of ALD cycles, see Fig. 5 (right). Films with fewer cycles, and thus lower thicknesses, tend to exhibit lower  $T_c$  values, which can be attributed to insufficient crystallinity and incomplete phase development at these early stages of growth. As the number of ALD cycles increase and the films grow thicker, the crystallinity improves and the desired phases become more fully realized, resulting in a rise in  $T_c$ . The critical temperature eventually stabilizes within a range of 8–12 K at higher thicknesses (60–70 nm), reflecting the establishment of a robust superconducting phase. The shaded region in the Fig. 5 (right) indicates that beyond a certain threshold thickness,  $T_c$  no longer significantly increases and plateaus. This suggests that optimal superconducting properties are achieved once the film reaches a certain level of thickness (30 nm) and crystalline quality.<sup>26</sup>

Further investigation by Proslir *et al.*<sup>94</sup> into the impact of introducing elemental zinc during the ALD process reveals additional improvements in key material properties such as phase purity, density, and  $T_c$ . While XRD analysis revealed that both Zn-free and Zn-containing films exhibited the same  $\gamma$ -Mo<sub>2</sub>N phase, the Zn introduction caused a shift in the preferred crystal orientation from (100) to (101), which may have implications for the films structural and electronic properties.<sup>94</sup> Despite no detectable change in stoichiometry or chlorine contamination, with Mo/N ratios remaining consistent and Cl concentrations below the detection limit, the film density increased from 8.1 to 8.6 g cm<sup>−3</sup>, suggesting that Zn improves packing efficiency or reduces defects. This was accompanied by an enhancement in  $T_c$ , potentially due to Zn's role in removing hydrogen impurities that can negatively impact superconductivity. Additionally, the room temperature resistivity decreased, further indicating improved film quality. These results suggest that Zn improves the purity, density, and superconducting properties of MoN films without altering their chemical composition.<sup>94</sup>

**4.2.1.3 NbN.** ALD of superconducting niobium nitride (NbN) films have been a topic of study for almost 35 years and it involves the sequential introduction of niobium and nitrogen



precursors to form highly uniform and conformal coatings.<sup>29–31,39,95–105</sup> The ALD processes utilizes various precursors, substrates, and plasma treatments to optimize NbN film deposition. Key precursors such as  $\text{NbCl}_5$ ,  $\text{NbF}_5$ , and tris(diethylamido)(*tert*-butylimido)niobium (TBTDEN) combined with nitrogen sources like  $\text{NH}_3$ ,  $\text{H}_2$ ,  $\text{N}_2$ , and Ar plasmas at temperatures ranging from 100 °C to 500 °C.<sup>29–31,39,99–105</sup> The growth rates, surface uniformity, and electrical properties of the films, both in their as-deposited and post-deposition treated states, underscore the critical role of process parameters in determining NbN film quality. These versatile ALD techniques are particularly valuable for applications in microelectronics and superconducting technologies, where NbN is one of the most extensively studied materials. The selected researches are reviewed in the following paragraphs with the aim of addressing all the processing parameter changes.

Sowa *et al.*<sup>104</sup> reported on the influences of deposition temperature,  $\text{H}_2$  flow rate and plasma power on the  $T_c$  of NbN films grown by PEALD using TBTDEN and  $\text{H}_2/\text{N}_2$  plasma. The relationship between deposition temperature and the resistivity ( $\rho$ ) as well as  $T_c$  of NbN films is described in Fig. 6(a). The resistivity starts at a high value of 3118  $\mu\Omega\text{ cm}$  at 100 °C and decreases significantly to 183  $\mu\Omega\text{ cm}$  at 300 °C. Meanwhile, the  $T_c$  rises from 6.4 K at 150 °C to 13.7 K at 300 °C, with no superconducting transition observed for the film deposited at 100 °C. A similar trend was reported by Ziegler *et al.*,<sup>100</sup> where the resistivity of NbN films dropped from 750  $\mu\Omega\text{ cm}$  at 200 °C to 250  $\mu\Omega\text{ cm}$  at 400 °C, and  $T_c$  increased from 4.5 K to 10.2 K for 40 nm thick films deposited with a plasma time of 50 seconds.

For NbN films grown at 300 °C and 300 W plasma power, increasing the  $\text{H}_2$  flow rate from 10 to 40 sccm resulted in lower

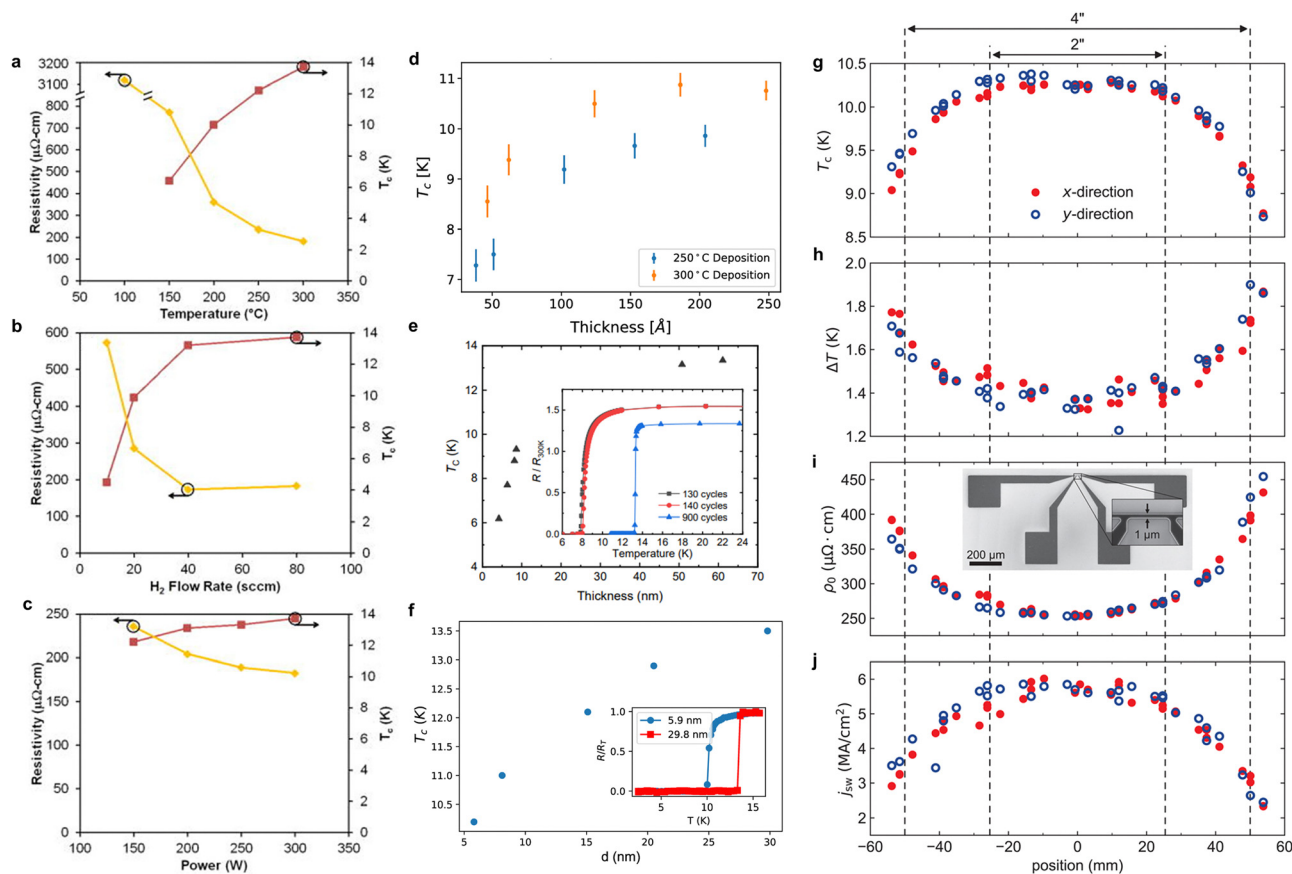


**Fig. 6** The influences of deposition temperature,  $\text{H}_2$  flow rate and plasma power on the  $T_c$  of NbN films grown by PEALD using TBTDEN and  $\text{H}_2/\text{N}_2$  plasma. Room temperature resistivity and  $T_c$  as a function of the (a) substrate temperature at 80 sccm  $\text{H}_2$  and 300 W, (b)  $\text{H}_2$  flow rate at 300 °C and 300 W, and (c) plasma power at 300 °C and 80 sccm  $\text{H}_2$ .<sup>104</sup> Copyright 2017, AIP Publishing. (d)  $T_c$  of NbN samples as a function of thickness, with deposition temperature noted.<sup>99</sup> Copyright 2020, Springer Publishing. (e) NbN films prepared from TBTDEN and  $\text{N}_2/\text{H}_2$  plasma at the substrate temperature of 300 °C and the plasma power of 300 W.  $T_c$  of the NbN films vs. the thickness. Inset: Resistance of three NbN films vs. temperature showing the superconducting transition. The resistance is normalized by the room temperature value  $R_{300\text{K}}$ .<sup>102</sup> Copyright 2020, AIP Publishing. (f)  $T_c$  versus measured film thickness,  $d$ , for thickness series. Inset: Normalised resistance resistance/room temperature resistance ( $(R/R_{300\text{K}})$ ) versus temperature for  $d = 5.9\text{ nm}$  and  $d = 29.8\text{ nm}$  films.<sup>103</sup> Copyright 2017, IOP Publishing. NbN films deposited by PEALD using TBTDEN as precursor and hydrogen radical for the plasma step with a deposition temperature 380 °C. (g) Distribution of critical temperature, (h) superconducting transition width, (i) residual resistivity at 25 K, and (j) switching current density at 4.2 K over the samples position on the wafer along the x- and y-axis. The measurements were conducted on microbridges of 1  $\mu\text{m}$  width and 6.1 nm thickness (see the scanning electron micrograph in the inset). The vertical dashed lines illustrate wafer edges of the denoted sizes.<sup>29</sup> Copyright 2021, AIP Publishing.



resistivity and higher  $T_c$ , as shown in Fig. 6(b). However, when the  $H_2$  flow was doubled from 40 to 80 sccm, there were slight increases in both resistivity and  $T_c$ . Consequently, the lowest resistivity (173  $\mu\Omega$  at 40 sccm  $H_2$ ) and the highest  $T_c$  (13.7 K at 80 sccm  $H_2$ ) observed in the study did not occur simultaneously, which they attributed to a difference in grain size and oxygen contamination.<sup>100,104</sup>

The influence of plasma power on room temperature resistivity and  $T_c$  was also studied at a constant deposition temperature of 300 °C and  $H_2$  flow rate of 80 sccm.<sup>104</sup> As shown in Fig. 6(c), increasing plasma power slightly improved both resistivity and  $T_c$ . The authors suggested that plasma power might have a more pronounced effect if the deposition temperature and  $H_2$  flow rate were further away from their optimal values.<sup>104</sup>

Shegren *et al.*<sup>99</sup> studied the influence of deposition temperature (for 250 °C and 300 °C) and film thickness on the  $T_c$  of NbN films deposited by PEALD using TBTDEN and Ar-plasma as precursor materials and plasma power of 300 W, see Fig. 6(d). Films grown both at 250 °C and 300 °C exhibited crystalline structure. The  $T_c$  increases with both film thickness and deposition temperature. For thinner films around 50 Å,  $T_c$  is relatively low, around 7 to 8 K, but it rises as thickness increases, reaching values above 10 K for films thicker than 150 Å. Films deposited at 300 °C generally exhibit higher  $T_c$  values compared to those deposited at 250 °C, with the maximum  $T_c$  = 10.87 K at 300 °C and around 250 Å thickness. This indicates a strong correlation between thickness, deposition temperature, and the superconducting properties of NbN films. However, the maximum  $T_c$  reported in this study is lower than other ALD NbN processes.<sup>101,102,104</sup>

The superconducting properties of NbN films prepared from TBTDEN and  $N_2/H_2$  plasma at the substrate temperature of 300 °C, growth rate of 0.68 Å per cycle and the plasma power of 300 W has been reported by Cheng *et al.*<sup>102</sup> The study focuses on the relationship between  $T_c$  of the NbN films and their thickness, as illustrated in Fig. 6(e). As anticipated by other researches, a higher  $T_c$  is observed for thicker films, reaching a saturation point of 13.3 K at a thickness of 61 nm (900 cycles).<sup>102</sup> The inset of Fig. 6(e) provides a closer look at the resistance vs. temperature curves around the superconducting transition region. The remarkably sharp transition observed in the 900-cycles film, with a transition width of only 0.15 K (90% to 10% of resistance), indicates a high level of homogeneity and uniformity in the deposited film.<sup>102</sup> In contrast, the 130-cycles and 140-cycles films exhibit a reduced  $T_c$  around 8 K and a broader transition width of 1.7 K, suggesting less uniformity in those samples.<sup>102</sup>

The superconducting properties of NbN films grown from TBTDEN precursor with  $Ar/H_2$  plasma with lower deposition temperature of 250 °C is reported by Lennon *et al.*,<sup>103</sup> see Fig. 6(f). As the thickness increases,  $T_c$  also rises, nearing a saturation point of 13.5 K for films with a thickness of 29.8 nm. In the ultrathin regime, films exhibit  $T_c$  values of 10.2 K for a 5.9 nm thickness and 11.0 K for 8.0 nm. These  $T_c$  values are higher to counter reported sputtered NbN films which show

$T_c$  values of 8.1 K and 10.3 K for 9 nm films.<sup>106</sup> As film thickness decreases, superconducting transition width ( $\Delta T_c$ ) increases, indicating reduced uniformity,<sup>103</sup> but the PEALD films still show narrower transition widths (0.8 K) compared to sputtered films (1.4 K).<sup>106</sup>

Knehr *et al.*<sup>29</sup> investigated the wafer-level uniformity of superconducting properties in NbN films deposited *via* PEALD using the TBTDEN precursor and hydrogen radicals during the plasma step, with a deposition temperature of 380 °C. The uniformity of several superconducting metrics across the NbN film is shown in Fig. 6(e)–(j), revealing minimal variation over a 2-inch diameter wafer. Electrical parameters such as resistivity and critical temperature show only slight deviations near the wafer center. However, as distance from the center increases, especially towards the edges of a 4-inch wafer, a degradation in film quality is observed. At these edges, resistivity increases by an average of 53%, and the switching current density decreases by 45%. The  $T_c$ , however, is more stable across the deposition area, showing only a 10% reduction near the edges. They attributed this stability to  $T_c$  being determined by contiguous, high-quality regions within the microbridge.<sup>29</sup> In contrast, the transition width ( $\Delta T_c$ ) provides a better measure of film homogeneity as it reflects the spread of superconducting properties across various regions. Moving from the center to the edge of the 4-inch wafer,  $\Delta T_c$  increases by a notable percentage, indicating reduced homogeneity in different grains and regions of the film. Within the more uniform central region, the  $T_c$  aligns with other reports for similar deposition parameters and thicknesses on sapphire substrates.<sup>107</sup> However, for other metrics, ALD-NbN films deposited on thermal oxide appear to perform slightly better as superconducting materials, showing a 20% higher switching current density and lower resistivity and transition width by comparable percentages. When compared to slightly thicker ALD-NbN films deposited on SiN, as reported by Cheng *et al.*,<sup>102</sup> the results were similar in most parameters, although  $T_c$  was  $\approx 2$ –3 K higher and the transition width slightly lower (by about 0.3 K).<sup>107</sup> The discrepancies could be attributed to differences in deposition temperatures (380 °C *vs.* 300 °C), plasma gas compositions (pure hydrogen *vs.* mixed nitrogen/hydrogen), and substrate materials (thermally oxidized silicon *vs.* LPCVD-grown SiN).<sup>102,107</sup>

There are only few reports on superconducting NbN films grown by thermal ALD, likely due to their inferior superconducting properties compared to those grown by PEALD. Most efforts in thermal ALD have focused on using  $NbCl_5$  and  $NH_3$  process chemistry.<sup>94,95,97,98</sup> One approach to improve the superconducting properties of thermal ALD NbN films involves introducing Zn vapor between the  $NbCl_5$  and  $NH_3$  pulses. This technique has been shown to reduce room-temperature resistivity by nearly a factor of two.<sup>95,96</sup> Moreover, adding an intermediate Zn pulse increased the  $T_c$  of thermal ALD NbN films deposited at 450 °C from 3 K to 5 K.<sup>94</sup>

#### 4.2.2 Ternary nitrides

**4.2.2.1 NbTiN.** The binary niobium nitride (NbN) possesses a NaCl-like cubic structure ( $\delta$ -phase) with a bulk  $T_c$  of up to 17.3 K.<sup>108</sup> However, this phase exists within a narrow nitrogen





content window; outside of this range, other superconducting with lower  $T_c$  and non-superconducting phases can form, resulting in films with lower  $T_c$ . Additionally, NbN exhibits high normal conducting resistivity and low RRR values due to the presence of vacancies in the lattice.<sup>6</sup> In contrast, niobium titanium nitride (NbTiN) retains all the advantages of NbN, particularly the high  $T_c$  of 17.8 K,<sup>109</sup> while offering significantly lower resistivity and high RRR in the normal state due to the incorporation of Ti atoms into the lattice.<sup>6,34,40,110</sup> NbTiN results from the miscible nature of the binary NbN and TiN compounds. Notably, TiN appears to be much less prone to nitrogen off-stoichiometry compared to NbN. Thus, the addition of Ti, which serves as an effective nitrogen getter, stabilizes the  $\delta$ -phase NbN, resulting in a compound with lower resistivity while maintaining a high critical temperature.<sup>6,34,40,110</sup> NbTiN compounds have been deposited using both thermal and plasma enhanced ALD systems. The selected research works from both techniques, focusing on how composition and post deposition treatments can tune the superconducting properties is discussed below.

The superconducting properties of NbTiN films fabricated by PEALD using TBTDEN and TDMAT precursors as Nb and Ti sources and  $H_2/N_2$ -plasma at a deposition temperature 250 °C is reported by Gonzalez *et al.*<sup>40</sup> The  $T_c$  and  $\Delta T_c$  of as deposited films as a function of Nb content on NbTiN thin films with eight different compositions is shown in Fig. 7(a). The  $T_c$  increases with increasing Nb content in the composition and the maximum  $T_c$  of 7 K is reported for Nb<sub>0.66</sub>Ti<sub>0.33</sub>N

composition, but decreased for the highest Nb concentrations. These findings contradict other studies, where  $T_c$  either increases monotonically<sup>110</sup> or stabilizes<sup>111</sup> for Nb concentrations higher than the ratio 1:1. The observed lower  $T_c$  may stem from the reduced deposition temperature of 250 °C compare to others that exceed 300 °C.<sup>34,110</sup> Higher deposition temperatures may induce the growth of denser and more crystalline films leading to higher  $T_c$ , whereas a deficit or excess of nitrogen can impact  $T_c$ .<sup>6</sup> The transition width, remains nearly constant up to the maximum observed  $T_c$ , after which it increases slightly but noticeably. Despite this slight increase, all studied concentrations of the ternary compounds exhibit a sharp superconducting transition, with a  $\Delta T_c$  of less than 0.3 K. This narrow transition width is a strong indication of high compositional homogeneity and the excellent quality of the films.<sup>40</sup> The Nb<sub>0.75</sub>Ti<sub>0.25</sub>N film composition was chosen to investigate the superconducting properties across different film thicknesses, ranging from 6 to 74 nm. The thinnest film does not exhibit a superconducting transition. However, as the thickness increases, the Nb<sub>0.75</sub>Ti<sub>0.25</sub>N films become superconducting, with  $T_c$  rising and the transition becoming sharper, see Fig. 7(b). Post-deposition annealing was employed to enhance film quality by promoting grain growth, recrystallization, or reducing defects, thereby improving the superconducting critical temperature  $T_c$ . Two different thermal treatments were applied to Nb<sub>0.75</sub>Ti<sub>0.25</sub>N thin films of varying thicknesses, followed by measurements of their resistance as a function of temperature. From the analysis of the thickest film (74 nm), as shown in Fig. 7(c), two key

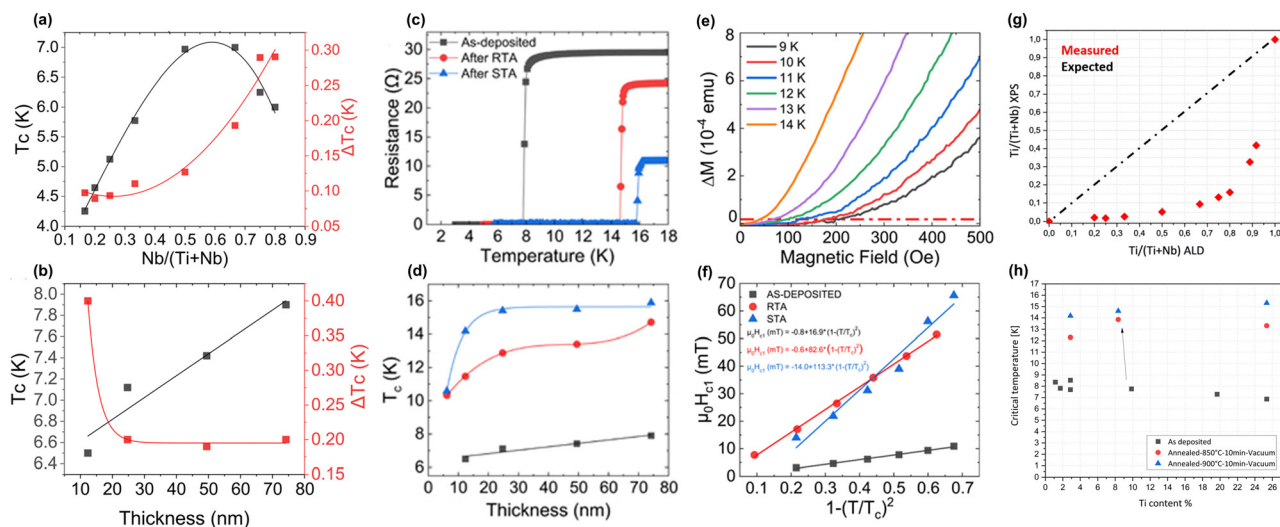


**Fig. 7** (a)  $T_c$  and  $\Delta T_c$  as a function of Nb content on NbTiN thin films with eight different compositions. Solid lines represent a polynomial fit as a guide to the eye. (b)  $T_c$  in black and  $\Delta T_c$  in red as a function of Nb<sub>0.75</sub>Ti<sub>0.25</sub>N thin film thickness. (c) Resistance as a function of temperature for the thickest Nb<sub>0.75</sub>Ti<sub>0.25</sub>N thin film as-deposited (black), and RTA- (red) and STA-treated (blue). (d)  $T_c$  as a function of the thickness for as-deposited (black), and RTA- (red) and STA-treated (blue) films. (e) Magnetization curve after subtracting the Meissner line as a function of the applied magnetic field for six different temperatures for the thickest Nb<sub>0.75</sub>Ti<sub>0.25</sub>N thin film STA-treated. The red dashed line marks the criterion  $\Delta m = 1.810 \times 10^{-5}$  (emu). (f)  $\Delta \mu_0 H_{c1}$  vs.  $1 - (T/T_c)^2$  for the thickest Nb<sub>0.75</sub>Ti<sub>0.25</sub>N thin-film as-deposited, and RTA- and STA-treated. The linear fit functions are given in the same color-code. The geometrical effect on the evaluation of  $H_{c1}$  has been taken into account with a demagnetization factor  $N = 0.68$ .<sup>40</sup> Copyright 2023, AIP Publishing. NbTiN films deposited using thermal ALD with alternating cycles of NbN and TiN using NbCl<sub>5</sub>, TiCl<sub>4</sub> and NH<sub>3</sub> precursors at 450 °C. (g) The chemical composition of NbTiN films obtained from XPS analysis as a function of the ALD ratios of NbN and TiN cycles (in red). The dashed line presents the expected composition from the TiN and NbN ratios used in the ALD recipe. (h)  $T_c$  of the NbTiN films before and after different annealing treatments measured on sapphire substrates as a function of the Ti content.<sup>34,113</sup> Copyright 2023, JACOW Publishing.



observations can be made: first, the resistance at low temperatures decreases, and second,  $T_c$  shifts to significantly higher values.<sup>40</sup> Additionally, the room-temperature resistivity is similar for both rapid thermal annealing (RTA) and slow thermal annealing (STA) at this thickness, which suggests that the STA treatment increases the RRR of the film.<sup>40</sup> Notably, the thinnest film (6 nm) becomes superconducting after both annealing procedures, with  $T_c$  exceeding 10 K, as seen in Fig. 7(d). This indicates that the as-deposited thinnest film is likely amorphous, and only after thermal treatment it does become polycrystalline, thereby exhibiting superconductivity. In contrast, thicker films ( $\geq 10$  nm) are already polycrystalline in their as-deposited form and display a superconducting transition. It is important to note that while  $T_c$  increases with film thickness after RTA, it stabilizes for films thicker than 25 nm after STA. Overall, both post-deposition thermal treatments significantly improve the properties of the films, with STA yielding a better outcome, achieving a maximum  $T_c$  of 15.9 K—the highest value reported to date for both thermal ALD and PEALD techniques. In-plane DC magnetization studies on the thickest Nb<sub>0.75</sub>Ti<sub>0.25</sub>N film were performed using a vibrating sample magnetometer (VSM). Fig. 7(e) shows magnetization difference ( $\Delta m$ ) vs. magnetic field ( $H$ ) curves, with the first penetration field  $H_{fp}$  determined for six temperatures (9–14 K). Since  $H_{fp}$  underestimates  $H_{c1}$ , demagnetization effects ( $N = 0.68$ ) were considered for accurate evaluation. Measurements allowed determination of the  $H_{c1}(T)$  trend for as-deposited and annealed films. Fig. 7(f) presents  $\mu_0 H_{c1}$  vs.  $1 - (T/T_c)^2$ , with  $\mu_0 H_{c1}$  at 2 K obtained *via* linear fit: 15 mT for as-deposited, increasing to 81 mT (RTA) and 98 mT (STA),<sup>40</sup> aligning with previous reports on PEALD NbTiN films.<sup>110,112</sup>

Kalboussi *et al.*<sup>34,113</sup> reported the deposition of NbTiN films using thermal ALD with alternating cycles of NbN and TiN, employing NbCl<sub>5</sub>, TiCl<sub>4</sub> and NH<sub>3</sub> as precursors at 450 °C. They measured the average titanium and niobium content across the depth profile of the films and analyzed it as a function of the Ti/(Ti + Nb) ratio in the ALD recipe, as shown in their XPS data of Fig. 7(g). The results demonstrated that increasing the number of TiN cycles in the ALD process led to a rise in the Ti/(Ti + Nb) content, following a power-law trend rather than a linear one. Notably, the chemical composition only exceeded a Ti/(Ti + Nb) value of 0.13 when the ALD ratio was above 0.7, consistent with density measurements that showed films with a Ti/(Ti + Nb) ALD ratio below 0.7 had a density similar to pure NbN. To achieve a 25% titanium content, an ALD recipe with 11 TiN cycles and 1 NbN cycle, corresponding to a Ti/(Ti + Nb) ALD ratio of 0.92, was required. They attributed this non-linear behavior to the use of chloride precursors, as films deposited with organometallic precursors like TDMAT and TBTDEN exhibit a linear trend,<sup>40</sup> whereas chloride-based precursors suggest that Ti etching occurs during ALD growth.<sup>34,113</sup> The as-deposited NbTiN films exhibited low  $T_c$ , ranging from 7 to 8 K, significantly lower than the typical 17 K for NbTiN, as summarized in Fig. 7(h). Despite increasing the Ti content, no clear trend in  $T_c$  was observed, although resistivity decreased. Structural analysis using XRD and Rutherford Backscattering

Spectrometry (RBS) revealed that the films were nitrogen-rich due to the reactions of NbCl<sub>5</sub> and TiCl<sub>4</sub> with NH<sub>3</sub> leading to smaller lattice constants and reduced  $T_c$ .<sup>34,113</sup> Contrary to the belief that Ti stabilizes the cubic phase of NbN to achieve higher  $T_c$ , their ALD-grown films with up to 25% Ti still showed small lattice constants and low  $T_c$  values. To address these limitations, they performed post-deposition heat treatments in a vacuum oven, significantly enhancing  $T_c$  from 8 K to 15.5 K<sup>34,113</sup> and lowering the resistivity of the films, approaching the highest ALD-reported  $T_c$  of 15.9 K.<sup>40</sup>

In an attempt to improve the superconducting response of thermal ALD NbTiN films, zinc (Zn) is added during the growth process, significantly influencing their  $T_c$ .<sup>31</sup> The incorporation of Zn enhances several key properties of the films, including density and surface roughness, while notably increasing  $T_c$ . This effect is particularly pronounced when comparing films with varying Nb/Ti ratios, with an optimal  $T_c$  of 12 K achieved at a Nb/Ti ratio of 2, despite TiN being a low-temperature superconductor with a  $T_c$  of only  $< 5$  K.<sup>26,38,77</sup> Interestingly, pure NbN films grown with Zn exhibit a  $T_c$  of only 5 K,<sup>31</sup> much lower than the expected 16 K for pure NbN. This suggests that Zn indirectly affects  $T_c$  by promoting the segregation of impurities, such as hydrogen, with Ti acting as a getter. As the hydrogen content decreases with increasing Ti concentration,  $T_c$  improves, doubling from 5 K to 12 K as hydrogen levels drop from 40% to 10%. Therefore, Zn plays a critical role in enhancing the superconducting properties of NbTiN films by improving purity and stabilizing the films structure.<sup>31</sup>

**4.2.2.2 MoC<sub>x</sub>N<sub>y</sub>.** Molybdenum carbonitride (MoCN) films are attracting significant interest for various applications due to their outstanding electrical conductivity, high thermal and chemical stabilities, superior mechanical strength, and superconductivity.<sup>114,115</sup> In the MoCN system, metal atoms form a closely-packed structure with nitrogen and carbon atoms occupying interstitial positions, resulting in several crystalline phases, most of which exhibit superconductivity. Variability in the  $T_c$  is influenced by factors such as disorder in crystalline phases and stoichiometric variations, which are intern influenced by films fabrication conditions such as the Mo/(C,N) ratio, deposition temperature, deposition pressure, and deposition method. MoCN films can be fabricated using techniques like CVD, PVD, solid-state reactions, and and ALD.<sup>116–118</sup> For films grown by ALD, only one group<sup>41</sup> has reported the superconducting behavior of films produced using PEALD.

Bertuch *et al.*<sup>41</sup> reported the synthesis of superconducting molybdenum carbonitride (MoC<sub>x</sub>N<sub>y</sub>) films using PE-ALD with the precursor (<sup>t</sup>BuN)<sub>2</sub>(NMe<sub>2</sub>)<sub>2</sub>Mo and H<sub>2</sub>/N<sub>2</sub> plasma at deposition temperatures between 80 °C and 300 °C. By adjusting these parameters, they controlled the composition and properties of the films. Their study focused on understanding how plasma composition and temperature influenced the chemical structure, as well as the electrical, optical, and superconducting properties of the films, particularly highlighting the correlation between composition and performance. The XPS analysis



revealed that the composition of the molybdenum carbonitride films varied significantly based on the nitrogen percentage in the  $N_2/H_2$  gas mixture and the deposition temperature. Increasing the  $N_2$  concentration resulted in a higher proportion of Mo–N bonds and a decrease in Mo–C bonds.<sup>41</sup> Conversely, at higher deposition temperatures with a plasma gas mixture of 5.9%  $N_2$  in  $H_2$ , nitrogen incorporation decreased while carbon content increased, suggesting that elevated temperatures enhance carbon ligand removal from the precursor, promoting Mo–C bond formation. Thus, the interplay between plasma composition and deposition temperature significantly influences the films' chemical structure and stoichiometry. The study also examined the electrical and optical properties of the films, such as resistivity, refractive index, and dielectric constant, based on plasma exposure time, nitrogen concentration, and deposition temperature. Films deposited at 150 °C with 11%  $N_2$  in  $H_2$  exhibited decreased resistivity with longer plasma exposure, indicating enhanced conductivity, as shown in Fig. 8(a). Increasing  $N_2$  concentration at this temperature with 40 seconds of plasma exposure at 300 W, also reduced resistivity, likely due to increased Mo–N bond formation, while the refractive index and dielectric constant increased, suggesting denser films Fig. 8(b). Similarly, resistivity decreased with higher deposition temperatures, particularly between 80 °C and 150 °C, stabilizing at elevated temperatures, which also correlated with increases in refractive index and dielectric constant Fig. 8(c). These findings underscore the ability to finely tune the electrical and optical properties of  $MoC_xN_y$  films for advanced electronic and optoelectronic applications. They reported a  $T_c$  of 8.8 K for the molybdenum carbonitride film with a composition of  $MoC_{0.45}N_{0.08}$ , deposited at 150 °C Fig. 8(d). This value is consistent with the range of  $T_c$  values reported for molybdenum

carbide deposited using other deposition technique, which typically falls in the range 5.1–12 K.<sup>119–121</sup> The superconducting properties were closely linked to the film's composition, particularly the ratio of carbon to nitrogen, and the deposition conditions, emphasizing the importance of precise control over the synthesis process to achieve desired superconducting characteristics.

**4.2.2.3  $TaC_xN_{1-x}$ .** Tantalum carbonitride ( $TaC_xN_{1-x}$ ) exhibits intriguing superconducting properties that are closely tied to its crystalline structure. Its  $T_c$  is governed by its electronic structure, lattice dynamics, and the interplay between its carbon and nitrogen composition.<sup>123</sup> The rock-salt cubic structure, typical of this material, creates a high density of electronic states at the Fermi level, which is crucial for the electron–phonon coupling mechanism that drives superconductivity.<sup>124</sup> Variations in the  $x$  value (carbon to nitrogen ratio) alter the lattice constants and, consequently, the vibrational modes of the crystal lattice, influencing the critical temperature. The superconductivity as a function of chemical composition and lattice parameters for the different TaCN is first reported by Thorwarth *et al.*<sup>123</sup> with  $T_c$  varies in the range of 8–12 K. TaCN films are typically fabricated using methods such as PVD, CVD and ALD.<sup>122,125–129</sup> While ALD techniques have been extensively used to produce high-quality TaCN films, superconducting properties have been reported by only one research group,<sup>122</sup> emphasizing the need for further investigation into this material's superconductivity when synthesized through ALD.

Peeters *et al.*<sup>122</sup> investigated the deposition of superconducting  $TaC_xN_{1-x}$  thin films using PEALD. The deposition process involved alternating exposures to a tantalum precursor (TBTDMT) and a  $N_2$  plasma source, with the use of Ar as a carrier gas. A key factor in controlling film properties was the

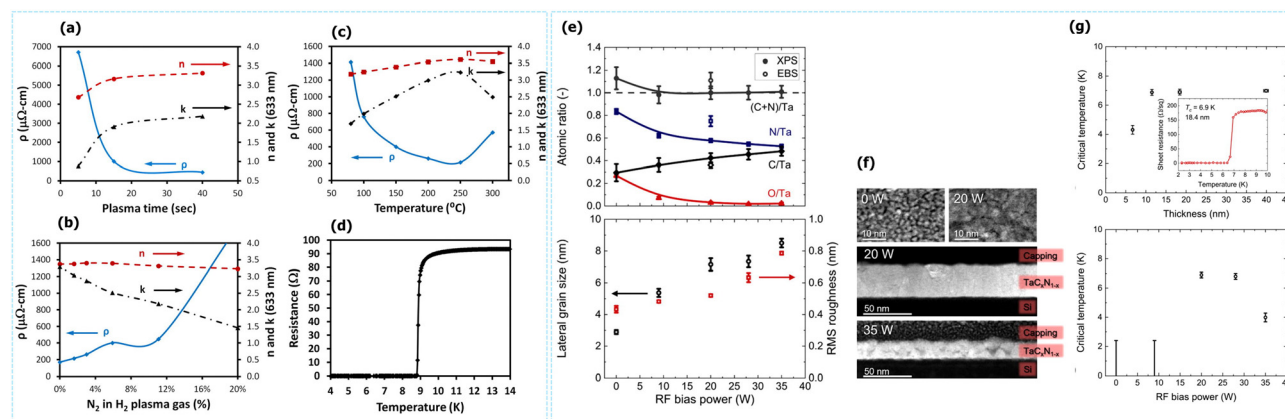


**Fig. 8** Resistivity, refractive index, and dielectric constant of  $MoC_xN_y$  films as a function of (a), the plasma exposure time for 150 °C deposition with 11%  $N_2$  in  $H_2$ . (b) percentage of  $N_2$  in  $H_2$  with 40 s, 300 W plasma for 150 °C deposition. (c) Deposition temperature with 5.9%  $N_2$  in  $H_2$ , 40 s, 300 W plasma. (d) Superconductivity measurement of 150 °C PE-ALD deposition with 100%  $H_2$ , 40 s, 300 W plasma.<sup>41</sup> Copyright 2017, AIP Publishing. (e) (top) Atomic ratios measured by XPS (closed symbols), with guides to the eye, and EBS (open symbols). (bottom) Lateral grain size (black) and RMS surface roughness (red) of  $TaC_xN_{1-x}$  films of 19 nm thickness for various applied RF bias powers. (f) Top-view HAADF-STEM images for films prepared with 0 and 20 W RF bias power and cross-sectional HAADF-STEM images for films prepared with 20 and 35 W RF bias power, where the capping layer is prepared by electron beam-induced deposition. The values of film thicknesses, varying between 11 and 35 nm. (g) (top) Critical temperature for the films prepared with 20 W RF bias power for a range of film thicknesses. The inset shows the superconducting transition recorded for the 18 nm film. (bottom) Dependence of the  $T_c$  of 19 nm thick films on the RF bias power. At low bias powers, the error bars indicate that no superconducting transition was measured above a temperature of 2.4 K.<sup>122</sup> Copyright 2023, AIP Publishing.



application of RF bias during the N<sub>2</sub> plasma step. The ion energy was controlled *via* substrate biasing, where a second radio frequency (13.56 MHz) power supply was connected to the substrate table. By varying the biasing power, the voltage over the plasma sheath was adjusted, enhancing the energy of ions impacting the film. Bias powers between 0 W (grounded table) and 35 W were used, resulting in average ion energies ranging from 20 to 250 eV, allowing precise control over ion energy and bombardment on the growing film. This biasing technique enabled adjustments in film composition, grain size, and resistivity, with the deposition temperature held at 250 °C to optimize the superconducting characteristics of the films. The XPS and elastic backscattering spectrometry (EBS) analyses were used to assess the atomic ratios of Ta, C, and N<sub>2</sub> in the films, revealing how variations in RF bias power affected stoichiometry throughout the film, see figure Fig. 8(e) (top). Their measurements demonstrated that ion energy during deposition significantly influenced the uniformity and consistency of the films' composition, both on the surface and through the bulk. Increased RF bias power was also associated with larger grain sizes, as confirmed by lateral grain size and surface roughness measurements, leading to improved crystallinity and reduced resistivity without significantly compromising surface smoothness—key for superconducting device integration.<sup>122</sup>

The group<sup>122</sup> also examined the relationship between lateral grain size and RMS surface roughness in the films, as illustrated in Fig. 8(e) (bottom). Their findings indicated that the lateral grain size increases with processing conditions such as higher RF bias power, reflecting enhanced crystallinity and reduced grain boundary density, which contribute to improved electrical properties like lower resistivity. While the RMS surface roughness, shown in red, may increase slightly with grain size due to larger crystalline domains, this increase is modest. This suggests that the films maintain a relatively smooth surface, which is crucial for high-quality interfaces in applications like superconducting quantum devices. Thus, the ability to enhance crystallinity and conductivity without significantly increasing surface roughness is essential for practical device integration. The high-angle annular dark-field scanning transmission electron microscopy (HAADF-STEM) images provide insights into the microstructure of TaC<sub>x</sub>N<sub>1-x</sub> films under varying RF bias power, as shown in Fig. 8(f). The film with 0 W RF bias exhibits a fine-grained structure and lower crystallinity, while the 20 W RF bias film shows larger, more defined grains, indicating enhanced grain growth and crystallinity. Cross-sectional images of the 20 W film reveal a uniform and dense structure with well-defined grain boundaries. Increasing the RF bias to 35 W results in even larger grains, suggesting enhanced columnar growth. These results highlight the critical impact of RF bias power on improving the films' crystallinity and grain growth, essential for their electrical and superconducting properties. The  $T_c$  of TaC<sub>x</sub>N<sub>1-x</sub> films prepared with 20 W RF bias across various thicknesses is shown in Fig. 8(g) (top). The  $T_c$  remains stable around 7 K, indicating that the superconducting properties are well-maintained regardless of thickness. The inset reveals a sharp drop in resistivity to zero for an 18 nm thick film,

confirming its superconducting behavior and suggesting high film quality with minimal defects.<sup>122</sup>

The influence of RF bias power on  $T_c$  was also examined in 19 nm thick samples, as depicted in Fig. 8(g) (bottom). The groups findings revealed a significant increase in  $T_c$  with higher RF bias power. At low bias powers, the lack of measurable superconducting transitions above 2.4 K indicates insufficient superconducting properties, likely due to poorer crystallinity or higher impurity levels. However, as RF bias power rises,  $T_c$  approaches 7 K, highlighting the critical role of RF bias in enhancing superconducting properties through improved film quality, increased grain size, and reduced impurities. The enhanced ion energy from higher RF bias likely facilitates a more homogeneous and well-ordered film structure conducive to superconductivity.

#### 4.2.3 Binary carbides

**4.2.3.1 NbC.** Niobium carbide (NbC) has attracted considerable research attention due to its unique combination of high chemical stability, high thermal stability, low electrical resistance and superconductivity.<sup>130,131</sup> Stoichiometric NbC crystallizes in a rock-salt structure, where niobium atoms form a cubic lattice, and carbon atoms occupy the octahedral interstitial sites.<sup>131</sup> NbC can be synthesized using various techniques, such as Pulsed laser ablation,<sup>132</sup> CVD,<sup>133</sup> sputtering<sup>134</sup> and ALD,<sup>32</sup> with only one group reported the superconducting properties of ALD grown NbC films.<sup>32</sup> A study by Klug *et al.*<sup>32</sup> examines the synthesis of these films through ALD using TMA, NbF<sub>5</sub>, and NbCl<sub>5</sub> as precursors, within a deposition temperature range of 125–350 °C.

To ensure the purity of the grown films, the authors<sup>32</sup> conducted XPS and RBS measurements, revealing varying amounts of impurities, including amorphous carbon(a-C), AlF<sub>3</sub>, NbF<sub>x</sub>, and NbCl<sub>x</sub>, were found in all samples, see Fig. 9(a) and (b). Films synthesized from TMA and NbF<sub>5</sub> contained Al, C, F, Nb, and O, with concentrations varying by deposition temperature. XPS analysis showed a decrease in Al (6 to 2 atom%) and F (55 to 6 atom%) concentrations as the temperature increased from 125 °C to 350 °C, while C (20 to 44 atom%) and Nb (15 to 28 atom%) increased. Oxygen peaked at 27 atom% at 300 °C, then dropped to 20 atom% at 350 °C. RBS detected no oxygen at 150 °C or 350 °C, suggesting that the oxygen observed by XPS resulted from surface oxidation post-deposition. Both XPS and RBS showed similar trends for Al, C, F, and Nb concentrations, and adjusting XPS for surface oxides provided results comparable to RBS, with the corrected composition at 350 °C being 2.4 atom% Al, 61–63 atom% C, 8.3–8.6 atom% F, and 26–28 atom% Nb. Additionally, XPS analysis across the 125 °C to 350 °C temperature range indicated that niobium was primarily in the Nb–C bonding state, characteristic of niobium carbide, with fluorine attributed to the use of NbF<sub>5</sub> as precursor. Despite variations in fluorine content, the stoichiometry of niobium carbide remained consistent, suggesting that fluorine did not significantly disrupt the formation of the desired carbide phase.<sup>32</sup>

The authors<sup>32</sup> investigated the effect of deposition temperature on film growth rate and surface roughness using XRR and AFM (Fig. 9c). The growth rate, as determined by XRR, remained



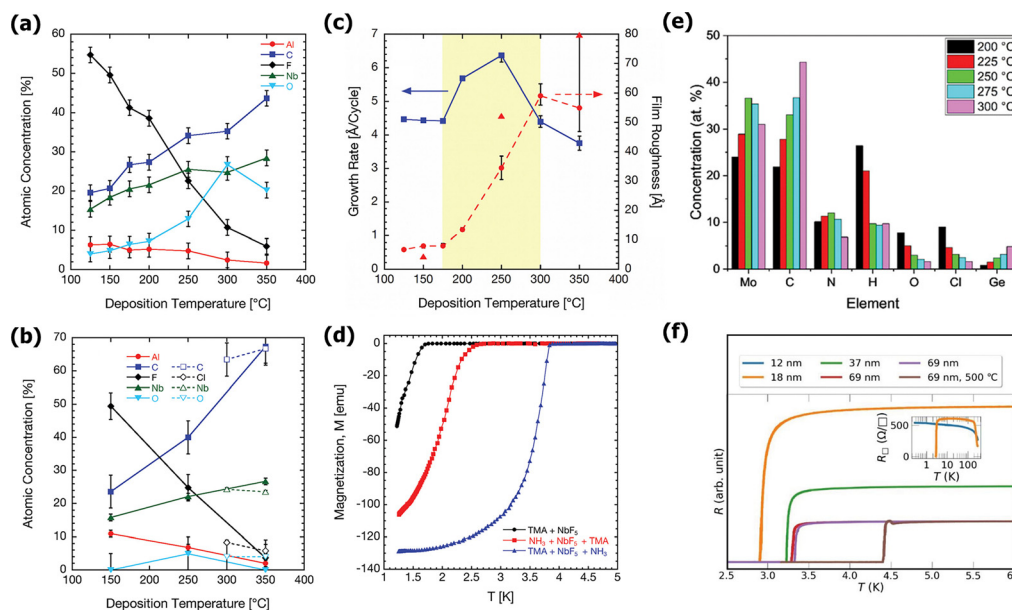


Fig. 9 NbC film composition measured by (a) XPS and (b) RBS vs. deposition temperature between 125 and 350 °C. XPS spectra were acquired following a 5–10 min Ar ion-milling step to remove surface contamination. Data from films grown with  $\text{NbF}_5$  and  $\text{NbCl}_5$  are represented by filled and open shapes, respectively. (c) The film growth rate determined by XRR (squares) and roughness determined by XRR (circles) and AFM (triangles) as a function of deposition temperature. (d) SQUID measurements of superconducting critical temperature  $T_c$  for films grown on Si(001) with the precursor sequence TMA +  $\text{NbF}_5$  (circles),  $\text{NH}_3$  +  $\text{NbF}_5$  + TMA (squares), and TMA +  $\text{NbF}_5$  +  $\text{NH}_3$  (triangles).<sup>32</sup> Copyright 2011, ACS Publishing. (e) ToF-ERDA compositional analysis of  $\text{MoC}_x$  films deposited at various temperatures (f) resistance of six  $\text{MoC}_x$  samples as functions of temperature. The red and violet lines show measurements of two nominally similar 69 nm samples cleaved from the same larger chip. The brown line shows the measurement of a third sample cleaved from the same 69 nm chip, which was annealed at 500 °C before the cryogenic measurement. The inset shows the absolute sheet resistances of 12 nm and 18 nm films, deposited on non-conductive substrates, as a function of temperature up to 300 K. The orange line is from the same measurement as in the main panel.<sup>36</sup> Copyright 2024, Wiley Online Library Publishing.

constant (4.5 Å per cycle) up to 175 °C, increased to 6.3 Å per cycle at 250 °C, and decreased to 3.8 Å per cycle at 350 °C. This nonmonotonic trend was attributed to possible temperature-dependent changes in surface species or active site density. Surface roughness, determined by XRR, stayed below 0.8 nm below 175 °C but increased significantly above 175 °C, from 1.3 nm at 200 °C to 5.9 nm at 300 °C. Due to XRR's limitations with Gaussian roughness assumptions, AFM was used for validation, showing roughness values of 0.4 nm at 150 °C, 5.2 nm at 250 °C, and 8.0 nm at 350 °C.<sup>32</sup>

The superconducting properties of films grown with  $\text{NbF}_5$  measured by SQUID are shown in Fig. 9(d). Only films deposited at temperatures of 350 °C or higher displayed a superconducting transition above 1.2 K, with the maximum transition temperature recorded at  $T_c = 1.8$  K (represented by circles) for a 75 nm thick film grown at 350 °C using 200 cycles of TMA and  $\text{NbF}_5$  on Si(001). This  $T_c$  is notably lower than that of bulk NbC, which has a  $T_c$  of 12 K,<sup>130</sup> largely due to a high level of impurities present in the films. However, the introduction of  $\text{NH}_3$  into the ALD process significantly improved the superconducting characteristics. When the sequence was modified to  $\text{NH}_3$  +  $\text{NbF}_5$  + TMA (squares), the  $T_c$  increased significantly to 2.5 K. Further enhancement of the  $T_c$  was achieved with the sequence TMA +  $\text{NbF}_5$  +  $\text{NH}_3$  (triangles), resulting in a  $T_c$  of 3.8 K. The enhanced transition temperatures in films grown with  $\text{NH}_3$  can be attributed to a reduced fluorine content from the reducing agent.<sup>32</sup> These measurements

indicate that the introduction and positioning of  $\text{NH}_3$  in the precursor sequence can effectively tune the superconducting properties of the films.

**4.2.3.2 MoC.** Molybdenum carbide ( $\text{MoC}$ ) thin films exhibit superconductivity with  $T_c$  in the range of 2.8–14.7 K.<sup>36,41,135–138</sup> They have been deposited by both physical and chemical deposition methods, including PVD,<sup>139</sup> carburization,<sup>140</sup> CVD,<sup>141</sup> and ALD.<sup>36,41,142,143</sup> Recent research by Kärkkäinen *et al.*<sup>36</sup> has delved into the superconducting properties of molybdenum carbide thin films ( $\text{MoCl}_5$ ) synthesized through ALD by utilizing  $\text{MoCl}_5$  as the metal precursor and  $(\text{Me}_3\text{Ge})_2\text{DHP}$  as the carbon source. The ALD process was conducted at temperatures between 200 and 300 °C, achieving a growth rate of 1.5 Å per cycle. This resulted in smooth films with a root mean square (RMS) roughness ranging from 0.3 to 0.6 nm across various substrates, including Si, TiN, and  $\text{HfO}_2$ . Notably, film growth was continuous even after just five cycles.<sup>36</sup>

Compositional analysis of the  $\text{MoC}_x$  films, as measured by Time-of-Flight Elastic Recoil Detection Analysis (ToF-ERDA), indicated that carbon content varied with deposition temperature, see Fig. 9(e). Lower deposition temperatures favored carbon incorporation from the precursor, while higher temperatures reduced carbon content due to enhanced desorption of volatile species and more efficient Mo–C bond formation. Chlorine contamination, a residual from the precursor, also decreased with increasing deposition temperature, indicating more complete





reactions, while minimal oxygen presence suggested low oxidation levels, preserving the films' electrical and structural integrity. Cryogenic measurements of molybdenum carbide films of various thicknesses (12, 18, 37, and 69 nm) deposited at 275 °C revealed superconductivity as shown in Fig. 9(f). Two samples from a 69 nm film exhibited consistent  $T_c$  values of approximately 3.3 K, while a 37 nm sample showed  $T_c$  of about 3.2 K and an 18 nm film had  $T_c$  of 2.9 K.<sup>36</sup> Annealing a third chip from the same 69 nm film at 500 °C under nitrogen increased  $T_c$  to 4.4 K, suggesting that annealing can enhance superconducting properties by improving micro-structure. However, attempts to anneal the 69 nm films at 650 °C resulted in peeling and they argued it as an indication for compromised adhesion or structural integrity at higher temperatures. For the 12 nm and 18 nm films on non-conductive substrates, the inset of the data of Fig. 9(f) showed that both exhibited increasing resistivity as the temperature decreased, with a RRR of less than 1, typical for disordered metals. The 12 nm film remained resistive down to 0.3 K, indicating it did not transition to a superconducting state within the measured range.<sup>36</sup> These results highlight the influence of film thickness and annealing on superconducting properties, with thicker and annealed films demonstrating better superconductivity.

Moreover, various molybdenum carbide materials, prepared using different techniques aside from ALD, exhibit superconducting properties, with their  $T_c$  depending on their crystal structure and synthesis methods. The cubic  $\delta$ -MoC<sub>0.681</sub>, synthesized from stoichiometric carbon and Mo powder under high pressure (6 GPa), features numerous disordered carbon vacancies and has a  $T_c$  of 12 K.<sup>119</sup> In contrast, the hexagonal-layered  $\eta$ -Mo<sub>3</sub>C<sub>2</sub>, fabricated from powders pressed at 1700 °C under 6 GPa, shows a  $T_c$  of 8.5 K.<sup>120</sup> Molybdenum carbide films, particularly in the  $\alpha$ -Mo<sub>2</sub>C and  $\beta$ -Mo<sub>2</sub>C phases, demonstrate superconductivity with  $T_c$  values ranging from 5.1 to 8.9 K.<sup>121</sup> Notably, the highest reported  $T_c$  for molybdenum carbide is 14.7 K, observed in a single-cubic  $\delta$ -MoC<sub>1-x</sub> film, synthesized *via* arc melting solidification with a composition between MoC<sub>0.65</sub> and MoC<sub>0.75</sub>.<sup>138</sup> While molybdenum carbide thin films deposited by ALD exhibit lower  $T_c$  values, their superconducting properties are promising and can be finely tuned through controlled deposition and post-deposition treatments, potentially matching or even surpassing currently reported best values.

#### 4.2.4 Other binary compounds

**4.2.4.1 NbSi.** Niobium and silicon are known to form bulk binary intermetallic niobium silicides that exhibit a range of stable compositions.<sup>144,145</sup> From these compositions different polymorphs of Nb<sub>3</sub>Si and NbSi exhibited superconductivity.<sup>144,146,147</sup> Nb<sub>x</sub>Si<sub>1-x</sub> films with various compositions can be deposited using a variety of methods including electron beam powder bed fusion,<sup>148</sup> sputtering,<sup>149</sup> CVD,<sup>150</sup> and ALD.<sup>146</sup>

Proslier *et al.*<sup>146</sup> demonstrated a successful synthesis of superconducting NbSi films with 1 : 1 stoichiometry using ALD. The researchers used niobium pentafluoride (NbF<sub>5</sub>) and disilane (Si<sub>2</sub>H<sub>6</sub>) as precursors, conducting experiments at various temperatures (150–400 °C) to explore the effects on film growth, structure, and superconductivity. The cross-sectional SEM images of NbSi films deposited on silicon trench structures at

200 °C using 300 NbSi cycles revealed that the films are highly uniform, conformal, and pinhole-free, showing the effectiveness of the ALD process in achieving excellent coverage, even on complex 3D structures, see Fig. 10(a).<sup>146</sup>

Proslier *et al.*<sup>146</sup> utilized RBS measurements to assess the composition of the NbSi films, revealing that for all studied temperatures, the films consistently maintained an Nb:Si ratio of 1 : 1 across the sample area with no detectable fluorine impurities, see Fig. 10(b). This uniform composition was observed even at deposition temperatures above 275 °C, where usually the growth shift towards CVD behavior. The researchers attributed this consistency to a stable growth mechanism involving silicon deposition during Si<sub>2</sub>H<sub>6</sub> exposure and partial silicon etching during NbF<sub>5</sub> exposure. In addition to RBS measurements, XPS analysis showed that the binding energies of the niobium and silicon peaks remained stable across different growth temperatures, see Fig. 10(c). This confirmed that the chemical composition and bonding were preserved throughout the deposition process, ensuring reliable film properties. The temperature dependence of the resistance between 2 and 50 K, measured on a NbSi film grown on a Si(100) substrate using 100 ALD cycles at 200 °C, is shown in Fig. 10(d). The graph exhibits a sharp decrease in resistance below the critical temperature  $T_c = 3.1$  K, indicating a superconducting transition. This marked the first instance of a superconducting NbSi film with a 1 : 1 stoichiometry, a significant milestone in the field.<sup>146</sup> Fig. 10(e) represents the sample magnetization  $M$ , as measured by SQUID, under an external magnetic field of 10 mG applied perpendicular to the sample as a function of the temperature. Fig. 10 (e:top) shows SQUID measurements of a multilayer structure grown at 200 °C, indicating a broad superconducting transition below 3.1 K, consistent with the maximum  $T_c$  measured by resistivity. They attributed the broad  $T_c$  distribution to the possible compositional inhomogeneities, although RBS indicated a uniform 1 : 1 NbSi ratio. Hydrogen trapped in the films may also cause broad transitions, as hydrogen is known to affect superconductivity. In contrast, a sharper transition was observed for NbSi films grown at 400 °C in the CVD regime. Similar results were seen in films grown at 225 °C and 275 °C, see Fig. 10 (e: middle and bottom). Annealing the samples at 400 °C in Ar or N<sub>2</sub> atmospheres significantly sharpened the transitions, suggesting hydrogen diffusion out of the films improved superconducting homogeneity.<sup>146</sup> NbSi films grown at 200 °C and capped with ALD Al<sub>2</sub>O<sub>3</sub> were further annealed at 600 °C. Post-treatment, XPS detected oxygen in the films, and SQUID measurements showed a suppressed  $T_c$  down to 2 K, see Fig. 10 (e: top). Films grown at 225 °C and 275 °C became insulating and changed color after the same treatment, possibly due to nitrogen incorporation forming a silicon/niobium nitride alloy.<sup>146</sup>

**4.2.4.2 CuO.** Tamm *et al.*<sup>35</sup> reported the synthesis and characterization of the first superconducting cupric oxide (CuO) thin films using ALD on both planar and three-dimensional substrates. The study aimed to optimize the ALD process for CuO films and assess their superconducting



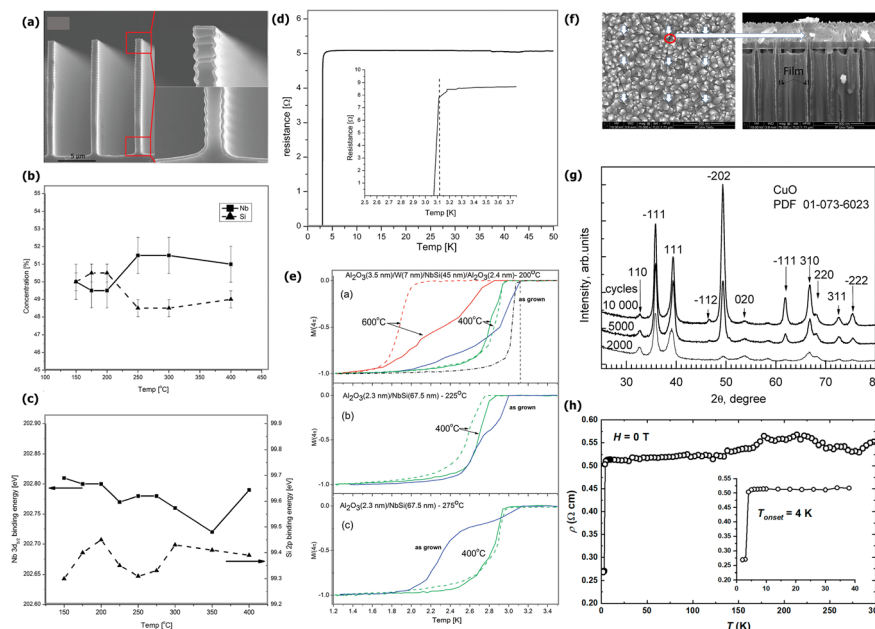


**Fig. 10** (a) SEM image of a NbSi film grown on Si(100) wafer at 200 °C using timing sequence 2-10-1-10 and 300 ALD cycles. (b) Composition of NbSi films measured by RBS and (c) binding energy of the Nb and Si peaks as a function of the growth temperature of films grown on Si(100) with 100 cycles using the same timing sequence. (d) Resistance versus temperature of a NbSi film grown at 200 °C on Si(100). The insert is an expanded view near the superconducting transition, indicated by a dashed line. (e) SQUID magnetometry measurements on NbSi films grown on Si(100) using the same timing sequence. The curves labeled "as grown" correspond to measurements done on as grown films, and the dashed lines correspond to measurement done after a postannealed films in Ar and the dotted lines in N<sub>2</sub>. The postannealing temperatures 400 or 600 °C are shown next to the corresponding curves.<sup>146</sup> Copyright 2011, ACS Publishing. (f) SEM images of 3D structures, called stacks, in the left top view of the stack; in the right, the CuO film inside 3D substrate (stack) are shown. (g) X-ray diffraction patterns of CuO thin films grown on SiO<sub>2</sub>/Si substrate by using different number of deposition cycles indicated by labels. (h) Electrical resistivity of CuO film grown after 5000 ALD cycles, with the thickness of 94 nm. The inset shows the low-temperature region.<sup>35</sup> Copyright 2020, MDPI Publishing.

properties at low temperatures. Copper(II)-bis(dimethylamino-2-propoxide) [Cu(dmap)<sub>2</sub>] and ozone were used as precursors, with ALD cycles ranging from 500 to 10 000. Film growth occurred within a temperature range of 112 °C to 165 °C, with 140 °C identified as the optimal temperature for high-purity film deposition.

The grazing incidence X-ray diffraction (GIXRD) patterns of CuO thin films grown at 140 °C using varying numbers of ALD cycles is shown in Fig. 10(g). The XRD data reveal that the films crystallized predominantly in the CuO phase, as indicated by the diffraction peaks corresponding to CuO. The intensity of the peaks increases with the number of deposition cycles, reflecting the growth in film thickness and improved crystallinity as the deposition progresses.<sup>35</sup> The influence of the number of cycles on the morphology of CuO films grown on both 2D and 3D structures is illustrated in Fig. 10(f). Notably, even with a large number of cycles, the films exhibit significant coverage on three-dimensional substrates with an aspect ratio of 1:20. Unlike planar Si(111) substrates, these 3D substrates have etched vertical channels perpendicular to the surface. Achieving adequate coverage is essential for effectively coating arbitrarily shaped nanostructures with functional films, particularly for applications in quantum-computer-related technologies. Electrical resistivity measurements were carried out using the two-probe method at low temperatures ranging from 1.8 K to 300 K, see Fig. 10(h). At room temperature, the CuO

films demonstrated a resistivity of approximately 0.55 Ω cm, with a slight temperature dependence in the 10–300 K range. However, a significant resistivity drop was observed at around 4 K, where the resistivity fell by 50%, reaching about 0.27 Ω cm at 2 K. This abrupt change may suggest the emergence of low-temperature superconductivity in the CuO films. However, they remark the need of further investigation to confirm this phenomenon and rule out other potential causes, such as film shrinkage or thermal expansion mismatches.<sup>35</sup>

#### 4.2.5 Complex oxides

*La<sub>2-x</sub>Sr<sub>x</sub>CuO<sub>4-y</sub>*. Sønsteby *et al.*<sup>42</sup> conducted a pioneering study that demonstrated the successful deposition of the first complex oxide thin film with superconducting properties using ALD. Their research focused on the deposition of the compound *La<sub>2-x</sub>Sr<sub>x</sub>CuO<sub>4-y</sub>* (LSCO), a complex cuprate oxide with a layered perovskite structure. LSCO has attracted attention for its superconducting properties, making it a valuable material for applications in advanced electronic systems. The study aimed to control the stoichiometry and structural properties of the LSCO films, investigating how these factors influence superconductivity. They successfully deposited LSCO thin films using the ALD process with La(thd)<sub>3</sub> and Cu(acac)<sub>2</sub> precursors and ozone. The films were grown at a temperature of 250 °C on LaAlO<sub>3</sub> (LAO) substrates, chosen for their structural compatibility with LSCO's layered perovskite structure. The researchers carefully controlled the stoichiometry of the films by adjusting the ratios of La, Sr,



and Cu precursor pulses. Initially, the films were amorphous, but post-deposition annealing at temperatures between 400 °C and 1000 °C induced crystallization. XRD analysis revealed that crystallization occurred at 650 °C into the Ruddlesden–Popper (RP) phase, essential for achieving LSCO's superconducting properties. This precise control over the deposition parameters was critical in producing the desired superconducting behavior in the LSCO films.

The study<sup>42</sup> utilized X-ray fluorescence (XRF) to measure the cation percentage of strontium (Sr) in the LSCO films as a function of the Sr precursor pulse ratio during ALD, see Fig. 11(a). The results indicated that the actual Sr content in the films did not increase linearly with the pulse ratio and was lower than expected at higher pulse percentages, suggesting non-ideal uptake or saturation effects. This finding highlights the complexity of achieving precise dopant control in ALD processes and emphasized the need for careful calibration to obtain the desired stoichiometry in complex oxide films. To verify the epitaxial growth and orientation of the LSCO films, cross-sectional STEM was employed, see Fig. 11(b). The analysis confirmed a high degree of epitaxial alignment between the LSCO films and the LAO substrate, with the crystalline planes of the film aligning well with those of the substrate. This structural coherence is critical for the superconducting properties observed in the study. Furthermore, the specific resistivity of the LSCO films was examined as a function of Sr content, see Fig. 11(c). It was found that the resistivity is highly dependent on the Sr doping level. Films with lower Sr concentrations exhibited insulating behavior with higher resistivity, while an increase in Sr content to  $\approx 5$ –6% resulted in a decrease in resistivity, indicating a transition to metallic behavior. Notably, near the composition  $\text{La}_{1.8}\text{Sr}_{0.15}\text{CuO}_{4-y}$ , the resistivity dropped sharply at low temperatures, signaling the onset of superconductivity. In addition, the specific resistivity of a 40 nm  $\text{La}_{1.81}\text{Sr}_{0.19}\text{CuO}_{4-y}$  thin film was measured, revealing metallic behavior at higher temperatures, with resistivity decreasing as temperature decreased, see Fig. 11(d). A sharp transition occurred around 20 K, where the resistivity dropped to near zero, indicating the onset of superconductivity with a  $T_c$  of approximately 20 K. However, this  $T_c$  is lower than that observed in bulk cuprate systems with  $x = 0.15$ , which exhibit higher  $T_c$  values around 40 K.<sup>151</sup>

While ALD LSCO thin films have demonstrated superconducting properties with a maximum  $T_c$  of 20 K, this relatively low  $T_c$  presents a significant barrier to widespread practical applications, especially when compared to high- $T_c$  superconductors such as YBCO ( $T_c \approx 93$  K)<sup>152</sup> and iron-based superconductors  $T_c \approx 55$  K.<sup>153</sup> The low  $T_c$  limits the efficiency and applicability of LSCO films in technologies where higher operating temperatures are desirable. In addition to this limitation, challenges such as achieving optimal stoichiometry and phase purity during and after deposition, as well as the inherent material properties, further hinder performance at higher temperatures and restrict broader applications. To address these challenges, strategies such as optimizing ALD process parameters (e.g., adjusting precursor selection and deposition temperature),

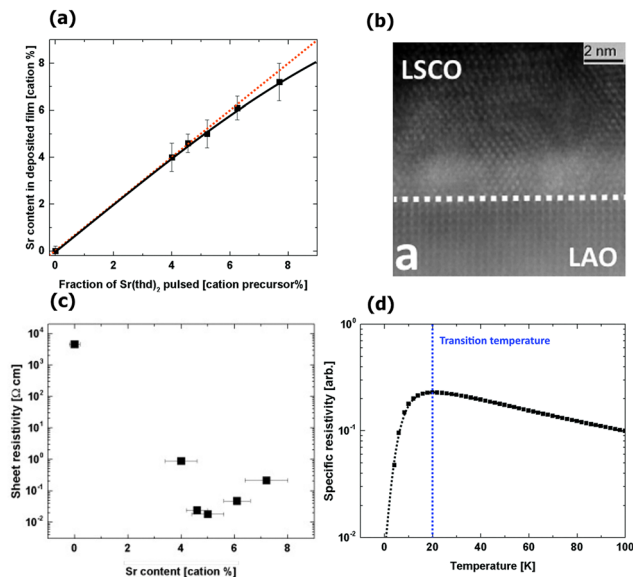


Fig. 11 (a) Cation percentage of Sr in the deposited film measured by X-ray fluorescence as a function of the cation percentage of strontium pulses in the process. The orange dotted line represents a theoretically linear response, while the black line corresponds to the observed response. (b) Cross-section HAADF-STEM image of  $\text{La}_{1.8}\text{Sr}_{0.15}\text{CuO}_{4-y}$  on a  $\text{LaAlO}_3(100)$  substrate. (c) Specific resistivity as a function of Sr content in the films. All data was collected for a sample annealed at 700 °C for 15 minutes in air. (d), Specific resistivity as a function of temperature for a 40 nm  $\text{La}_{1.81}\text{Sr}_{0.19}\text{CuO}_{4-y}$  thin film deposited on  $\text{LAO}(100)$ . The dotted blue line indicates the temperature where the resistivity starts to drop.<sup>42</sup> Copyright 2018, Royal Society of Chemistry Publishing.

introducing chemical dopants (e.g., Ba, Ca, Li, and  $\text{Mg}^{154,155}$ ) to modify the electronic structure, and applying strain engineering through substrate selection can help improve  $T_c$ . Additionally, constructing layered heterostructures, implementing post-deposition annealing to control oxygen content, and exploring nanostructuring techniques can further enhance the  $T_c$ , providing potential pathways to improve material performance and expand its practical applications. These strategies are not only applicable to LSCO but also hold potential for other superconducting complex oxides that can be synthesized *via* ALD.

### 4.3 Summary

The quest for higher-quality superconducting thin films characterized by fewer defects, greater uniformity, and enhanced homogeneity remains a fundamental goal in thin film preparation. ALD plays a crucial role in achieving these qualities, as it offers precise control over film thickness, composition, and uniformity factors critical for optimizing the superconducting transition temperature ( $T_c$ ). Moreover, higher deposition temperatures during ALD generally lead to improved film crystallinity, reduced impurity incorporation, and enhanced surface smoothness, all of which contribute to superior superconducting properties. In addition, post-annealing treatments can further refine the films microstructure, relieve residual stress, and enhance phase purity, leading to improved electrical transport properties and a potential increase in  $T_c$ . ALDs atomic-level precision, combined with



optimized deposition temperatures and post-deposition annealing, ensures uniformity across large areas and makes it an indispensable technique for advancing superconducting thin film technology.

Furthermore, ALD particularly through the use of supercycle approaches, has enabled the fabrication of complex, multicomponent superconductors such as LSCO and NbTiN. These supercycling techniques facilitate precise control over composition and thickness, making them especially well-suited for engineering layered heterostructures or nanolaminates with tailored superconducting properties. For instance, non-superconducting AlN layers deposited in vacuum by PEALD have been used as a buffer or interface layer for the epitaxial growth of NbTiN on silicon substrates, improving crystallinity and performance.<sup>40</sup> Moreover, ALD has been employed to create protective capping layers—offering conformal coverage and oxidation resistance for air-sensitive superconducting materials.<sup>156</sup> The capability of ALD to deposit uniform, pinhole-free layers on complex 3D topographies makes it a uniquely advantageous technique for constructing superconducting heterostructures, interface engineering, and protective layering, often beyond the capabilities of traditional methods such as sputtering or PLD.

Table 3 summarizes various ALD processes for producing superconducting thin films, detailing various materials, precursors, substrates, deposition temperatures, and resulting  $T_c$ . It showcases a diverse range of materials, including TiN, NbTiN, and complex

oxides like  $\text{La}_{2-x}\text{Sr}_x\text{CuO}_{4-y}$ . Deposition conditions vary significantly, with temperatures ranging from 80 °C to 500 °C and GPC values from 0.1 to 4.5 Å. The highest  $T_c$  reported is 20 K for  $\text{La}_{2-x}\text{Sr}_x\text{CuO}_{4-y}$ . The table also highlights the impact of different precursors and substrates on the quality and properties of the deposited films, as well as the need for specific crystallization conditions to attain optimal superconducting performance.

Fig. 12 summarize the highest reported  $T_c$  of various thin films deposited by ALD. The different materials deposited by ALD exhibit a wide range of  $T_c$  values, from approximately 1.8 K to 20 K. The highest  $T_c$  is observed for  $\text{La}_{2-x}\text{Sr}_x\text{CuO}_{4-y}$  films, while other materials like NbN and NbTiN also show relatively high  $T_c$  values. The diversity in  $T_c$  values reflects the influence of material choice and deposition conditions on the superconducting properties of thin films produced *via* ALD.

## 5 Applications

### 5.1 Multipacting mitigation for SRF cavities

Multipacting is a phenomenon that occurs in superconducting radio frequency (SRF) cavities where secondary electron emission causes an avalanche of electrons, leading to resonant electron buildup.<sup>16,158,159</sup> This can severely degrade the performance of SRF cavities by increasing power losses, creating local heating, and potentially damaging the cavity surfaces.<sup>16,158,159</sup>

**Table 3** ALD processes reported for superconducting thin films. The superconducting transition temperatures ( $T_c$ ) are the highest value reported for each material

	Atomic layer deposition							
	Precursors							
Material	Precursor A	Precursor B	Substrate	Dep. temp. /(°C)	GPC/(Å)	Cryst. req.	T <sub>c</sub> (K)	Ref.
TiN	TiCl <sub>4</sub>	NH <sub>3</sub>	Si	450	0.24	As-dep.	3.4	5
TiN	TiCl <sub>4</sub>	NH <sub>3</sub>	Si	350–450	0.23–0.33	As-dep.	3.8	26
TiN	TiCl <sub>4</sub>	N <sub>2</sub> /H <sub>2</sub> -plasma	Si	400	0.45	As-dep.	3.6	27
TiN	TDMAT	N <sub>2</sub> /H <sub>2</sub> -plasma	Si	350		As-dep.	2.09	157
TiN	TDMAT	N <sub>2</sub> /Ar-plasma	Si	300	0.65	As-dep.	4.35	77
TiN	TDMAT	N <sub>2</sub> -plasma	Si	270	0.9	As-dep.	4.62	38
NbN	NbCl <sub>5</sub>	NH <sub>3</sub>	SG	500	—	As-dep.	≈ 10	30
NbN	NbCl <sub>5</sub>	NH <sub>3</sub> + Zn	SG	450	0.2	As-dep.	5	31
NbN	TBTDEN	Ar-plasma	Si	250–300	0.51–0.62	As-dep.	10.9	99
NbN	TBTDEN	H <sub>2</sub> -plasma	Si	350	0.46	As-dep.	13.8	101
NbN	TBTDEN	H <sub>2</sub> /Ar-plasma	Si	250	0.12	As-dep.	13.5	103
NbN	TBTDEN	H <sub>2</sub> /N <sub>2</sub> -plasma	Si	100–300	0.35–0.76	As-dep.	13.7	104
NbN	TBTDEN	H <sub>2</sub> /NH <sub>3</sub> -plasma	Si	350	0.55 ± 0.02	As-dep.	12.3	105
NbN	TBTDEN	H <sub>2</sub> /NH <sub>3</sub> -plasma	Si	240–400	0.1–0.25	1000-Ar	13.8	39
NbTiN	NbF <sub>5</sub> ,TiCl <sub>4</sub>	NH <sub>3</sub> + Zn	Sa	450		As-dep.	13.4	33
NbTiN	NbCl <sub>5</sub> ,TiCl <sub>4</sub>	NH <sub>3</sub>	Nb, Sa	450	0.24 ± 0.03	850-vac.	15.5	34
NbTiN	TBTDEN, TDMAT	H <sub>2</sub> /N <sub>2</sub> -plasma	Si	250	0.62	1000-vac.	15.9	40
NbC	NbF <sub>5</sub>	TMA	Si, FS	350	3.75	As-dep.	1.8	32
NbC	NbF <sub>5</sub>	TMA + NH <sub>3</sub>	Si, FS	350	3.75	As-dep.	3.8	32
NbSi	NbF <sub>5</sub>	Si <sub>2</sub> H <sub>6</sub> ,SiH <sub>4</sub>	Si, Sa	150–400	4.5	As-dep.	3.1	146
CuO	Cu(dmap) <sub>2</sub>	O <sub>3</sub>	Si	112–165	0.16–0.39	As-dep.	4	35
MoN	MoCl <sub>5</sub>	NH <sub>3</sub>	BSG	450	0.31 ± 0.02	As-dep.	11.3 ± 0.05	33
MoC <sub>x</sub>	MoCl <sub>5</sub>	(Me <sub>3</sub> Ge) <sub>2</sub> DHP	Si,TiN, HfO <sub>2</sub>	200–300	0.36–0.56	As-dep.	2.9–4.4	36
MoC <sub>0.4–5</sub> N <sub>0.8</sub>	( <sup>t</sup> BuN) <sub>2</sub> (NMe <sub>2</sub> ) <sub>2</sub> Mo	H <sub>2</sub> /N <sub>2</sub> -plasma	Si	80–300	0.36–0.56	As-dep	8.8	41
TaC <sub>x</sub> N <sub>1–x</sub>	TBTDMT	Ar/N <sub>2</sub> -plasma	Si	250	0.35–0.55		7	122
La <sub>2–x</sub> Sr <sub>x</sub> CuO <sub>4–y</sub>	La(thd) <sub>3</sub> , Cu(acac) <sub>2</sub>	O <sub>3</sub>	Si	250	0.35–0.55	700-air	20	42

Si = silicon, BSG = borosilicate glass, QZ = quartz, FS = fused silica, Sa = sapphire. SG = soda glass, Nb = niobium, As-dep. = As deposited, vac. = vacuum.





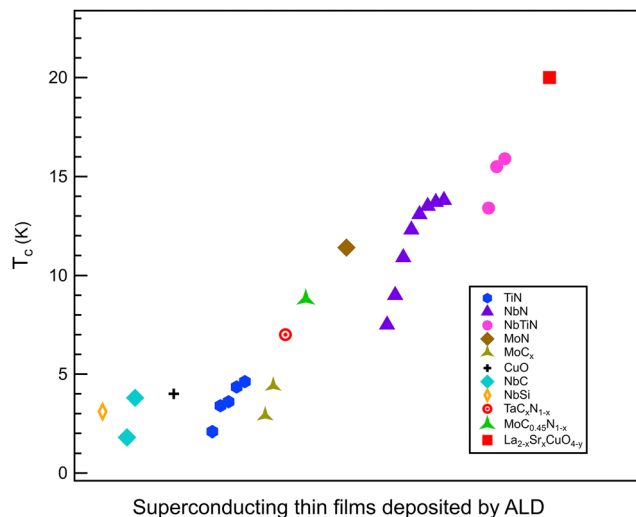


**Fig. 12** The  $T_c$  of different superconducting thin films deposited by ALD. The  $T_c$  are the highest values reported for each processing conditions and the processing conditions are summarized in Table 3.

Mitigating multipacting is crucial for enhancing the efficiency and longevity of SRF cavities, which are vital components in particle accelerators. Beyond SRF cavities, multipacting also affects a variety of RF devices, such as divertors in tokamaks,<sup>160</sup> satellite systems,<sup>161</sup> power couplers,<sup>162</sup> and antennas, emphasizing its widespread impact on RF technologies.<sup>163</sup>

Recent study by Kalboussi *et al.*<sup>164</sup> have explored the role of ALD in mitigating multipacting by optimizing the properties of superconducting thin TiN coatings. They explored how the thickness of ALD-grown TiN films influences the total electron emission yield (TEEY), chemical composition, and resistivity. To test their approach for mitigating multipacting, they initially deposited a 10 nm layer of  $\text{Al}_2\text{O}_3$  inside a 1.3 GHz cavity, followed by post-annealing at 650 °C for 10 hours in high vacuum conditions (approximately  $10^{-6}$  mbar). This procedure was intended to reduce two-level system dissipations in 3D superconducting niobium resonators.<sup>163</sup> The experiment was repeated twice on the same cavity, with surface resets achieved through chemical etching between  $\text{Al}_2\text{O}_3$  depositions and annealing cycles. Both RF tests conducted after deposition and post-annealing showed a strong, reproducible multipacting barrier between 15 and 18  $\text{MV m}^{-1}$ , which could not be processed further, preventing higher accelerating fields from being reached, see Fig. 13. A baseline RF test performed before the ALD deposition achieved a maximum accelerating field ( $E_{\text{acc}}$ ) of 32  $\text{MV m}^{-1}$ .<sup>164</sup>

The significant multipacting barrier observed was attributed to the three orders of magnitude higher electron emission from the  $\text{Al}_2\text{O}_3$  surface compared to the bare niobium surface, with a  $\text{TEEY}_{\text{MAX}}$  of 4.6 for  $\text{Al}_2\text{O}_3$  compared to 2.3 for niobium. To address this issue, they applied two different TiN film thicknesses 5 nm and 1.6 nm on top of a 10 nm  $\text{Al}_2\text{O}_3$  layer. The RF tests conducted after applying the 5 nm TiN coating revealed a significant degradation in the quality factors ( $Q_0$ ), with values dropping by over two orders of magnitude to  $10^8$ , and a

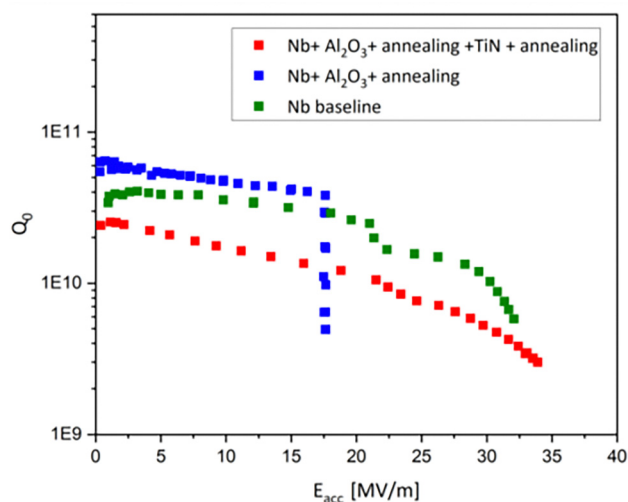


**Fig. 13** RF tests at 1.45 K of an ALD coated 1.3 GHz Nb cavity with different surface treatments. The green curve, baseline measurement, blue RF tests after 10 nm coatings of  $\text{Al}_2\text{O}_3$  and post-annealed at 650 °C in high vacuum, and red with additional 1.6 nm TiN film + annealing<sup>113,164</sup> Copyright 2024, AIP Publishing.

corresponding increase in surface resistance to 2200  $\text{n}\Omega$ .<sup>164</sup> Subsequent RF testing with a thinner 1.6 nm TiN coating showed a substantial improvement. The quality factor increased to the range of  $10^{10}$ , see Fig. 13. Additionally, the surface resistance decreased from 2200  $\text{n}\Omega$  to 10.8  $\text{n}\Omega$  at low temperatures upon reducing the TiN thickness. Notably, the multipacting barrier at 18  $\text{MV m}^{-1}$  disappeared, enabling the accelerating gradient to extend from 18  $\text{MV m}^{-1}$  to 35  $\text{MV m}^{-1}$ , effectively restoring the performance of the cavity to its baseline levels achieved with bare niobium.

## 5.2 Superconducting electronics and quantum devices

**5.2.1 Superconducting nanowire single-photon detectors (SNSPDs).** Superconducting nanowire single-photon detectors (SNSPDs)<sup>165</sup> have gained significant attention in photonic detection technologies due to their outstanding attributes, including high detection efficiency,<sup>166</sup> rapid response times,<sup>167</sup> low timing jitter,<sup>168</sup> and minimal dark count rates.<sup>169</sup> These features make SNSPDs particularly suitable for use in quantum optics, quantum communications, and quantum information processing.<sup>170</sup> Moreover, their ability to integrate seamlessly with on-chip nanophotonics circuits and to resolve both photon number and spectral information further extends their applicability in advanced optical systems.<sup>171,172</sup>

SNSPDs are typically fabricated as narrow nanowires, ranging from 20 nm to 150 nm in width, using ultrathin superconducting films between 3 nm and 10 nm thick. Two main classes of materials are used in their construction: polycrystalline nitride superconductors, like  $\text{NbN}$ <sup>171</sup> and  $\text{NbTiN}$ ,<sup>173</sup> known for their high critical temperatures and fast response times, and amorphous alloy superconductors, such as  $\text{WSi}$ ,<sup>166</sup>  $\text{MoSi}$ ,<sup>174</sup> and  $\text{MoGe}$ ,<sup>175</sup> valued for their high internal efficiencies and uniform structure. The choice of material depends on specific application needs, with polycrystalline nitrides offering

higher critical currents and faster detection capabilities, while amorphous alloys provide superior photon detection efficiency and are ideal for large-area detector arrays.

In their paper, Cheng *et al.*<sup>102</sup> present a detailed study on the fabrication and characterization of superconducting SNSPDs using PEALD NbN films. The fabricated detectors demonstrate broad saturated plateaus in the efficiency curves that are comparable with amorphous detectors, while simultaneously maintaining high switching currents. The authors fabricate 450 SNSPDs on each NbN chip, with nanowires of 50 nm, 75 nm, and 100 nm widths. These nanowires are patterned into circular shapes with a 15  $\mu\text{m}$  diameter for the active detection area, surrounded by floating nanowires for proximity effect correction during electron-beam exposure, forming a larger 25  $\mu\text{m}$  diameter circle, see Fig. 14(a) and (b). SEM reveals that the 50 nm-width nanowires exhibit exceptional uniformity, with less than 5 nm variation across the detection area, see Fig. 14(c). TEM provides cross-sectional images showing a nanowire thickness of 9.5 nm, including a 2 nm native oxide

layer, further emphasizing the precision and quality of the 140-cycle NbN films used in fabrication, see Fig. 14(d). Fig. 14(e) presents a compelling plot of normalized photon counts as a function of the relative bias current ( $I_{\text{bias}}/I_{\text{SW}}$ ) for SNSPDs with varying widths (100 nm, 75 nm, and 50 nm). The results showcase the intrinsic switching current  $I_{\text{SW}}$  for each detector type, illustrating the relationship between bias current and photon detection efficiency. The broad saturation plateaus observed in the photon counting curves indicate high internal efficiencies across the different designs, which is a crucial characteristic for the practical application of SNSPDs. The green dashed lines denoted the saturation current ( $I_{\text{sat}}$ ), reinforcing the importance of operating above this threshold to achieve optimal performance. As can be seen in Fig. 14(e) the detectors fabricated from the 140-cycle NbN films (with a thickness of 9.5 nm) has superior performance compared to the 130-cycle films. Notably, the 100 nm-width detectors from the 140-cycle film show a well-saturated efficiency with  $I_{\text{SW}}$  values exceeding 20  $\mu\text{A}$ , showcasing their potential for faster response

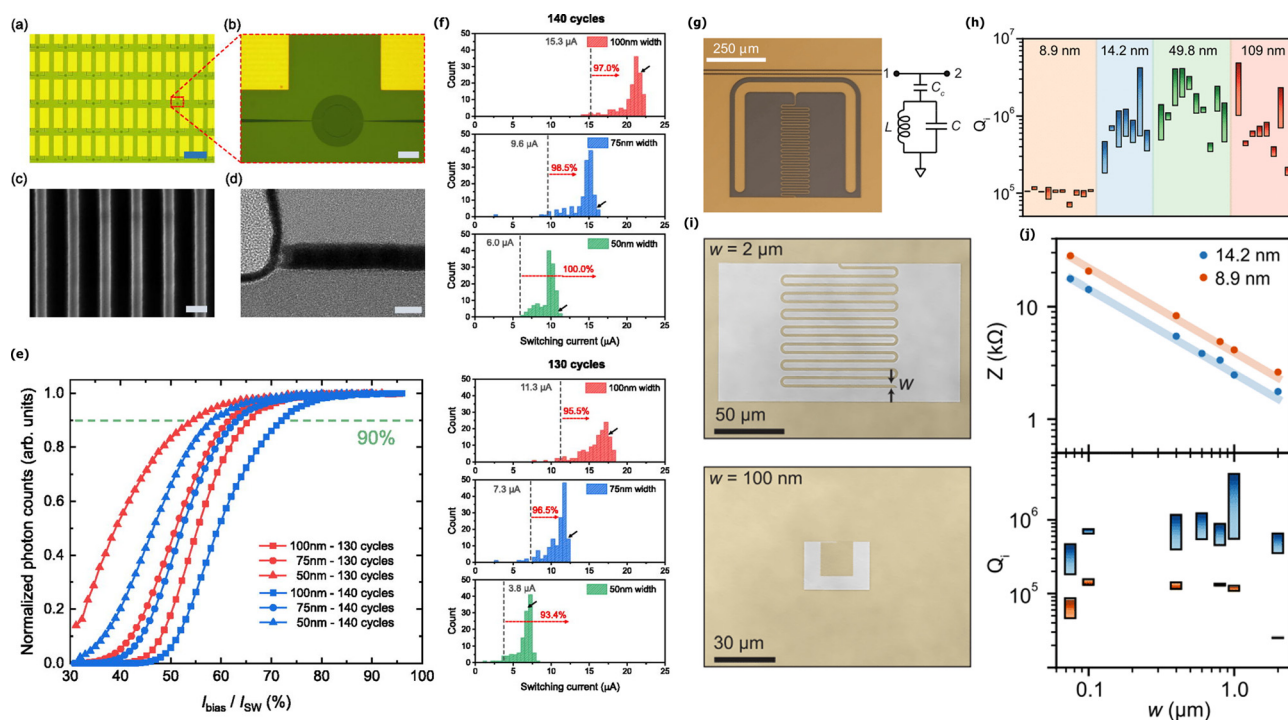


**Fig. 14** High quality SNSPD from NbN films.<sup>102</sup> (a) Optical micrograph of the fabricated SNSPD array. Scale bar: 200  $\mu\text{m}$ . (b) Close-up view of the nanowire detection area of an SNSPD. Scale bar: 10  $\mu\text{m}$ . (c) Close-up SEM image of an SNSPD with 50 nm width nanowires. The pitch of the nanowires is kept three times the width. Scale bar: 100 nm. (d) TEM image taken at the edge of the nanowire cross section patterned from the 140-cycle NbN film. (e) Normalized photon counts vs. the relative bias current ( $I_{\text{bias}}/I_{\text{SW}}$ ) for SNSPDs of varying width and thickness. The saturation current  $I_{\text{sat}}$  is defined as the current where 90% of the maximum counting rate is reached. (f) Histogram of  $I_{\text{bias}}/I_{\text{SW}}$  measured from SNSPDs of varying width and thickness. The gray dashed lines represent  $I_{\text{sat}}$  for each type of devices, and the calculated throughput yields are shown by the red dashed arrows.  $I_{\text{bias}}/I_{\text{SW}}$  of the reference detectors shown in plot (e) are marked using the black solid arrows.<sup>102</sup> Copyright 2019, AIP Publishing. Microwave characterization of high quality factor resonators from TiN films.<sup>38</sup> (g) Optical micrograph of a typical resonator ( $t = 49.8$  nm) used in this work, which can be described by the circuit model shown on the right. The transmission was measured from port 1 to port 2. (h) Internal quality factors of all resonators in this study, grouped by film thickness. For a single film thickness, each resonator's internal quality factor increases with power, visualized as a bar. The bottom of each bar corresponds to single photon  $Q_i$ , whereas the top corresponds to the high power saturated  $Q_i$  or the  $Q_i$  just below bifurcation (if bifurcation was observed). The average of these resonators ranges from  $1.1 \times 10^5$  ( $t = 109$  nm) to  $9.4 \times 10^5$  ( $t = 4.2$  nm). (i) Optical micrographs of high impedance TiN (false-colored yellow) microwave resonators with inductor wire width  $w = 2$   $\mu\text{m}$  (top) and  $w = 100$  nm (bottom). Note the different scale bars. (j) Internal quality factor (top) at 20 mK and characteristic impedance (bottom) of the resonator designs shown in (a) as a function of  $w$ . Resonators are fabricated on TiN films  $t = 8.9$  nm thick (red) and  $t = 14.2$  nm thick (blue).<sup>38</sup> Copyright 2019, AIP Publishing.



times and reduced timing jitter. Fig. 14(f) illustrates the high homogeneity and exceptional uniformity of the NbN films through an  $I_{\text{SW}}$  histogram for SNSPDs with different designs. The histogram shows a tightly clustered distribution of  $I_{\text{SW}}$ , with only a few nanowires exhibiting reduced  $I_{\text{SW}}$  values, likely due to fabrication constrictions. To estimate the detector throughput yield, the authors compare  $I_{\text{SW}}$  values with those of reference detectors, as shown in Fig. 14(e), defining the  $I_{\text{sat}}$  as the point where 90% of the maximum counting rates are reached, marked by green dashed lines in Fig. 14(e) and gray dashed lines in Fig. 14(f). The throughput yield is then calculated as the proportion of detectors with  $I_{\text{SW}}$  values greater than  $I_{\text{sat}}$ . The results reveal impressive throughput yields exceeding 93% for all detector types, with the 50 nm-width detectors from the 140-cycle NbN film achieving a remarkable 100% yield. This high yield is attributed to the broader saturation plateau and enhanced uniformity of the thicker 140-cycle film compared to the 130-cycle film.<sup>102</sup> Red dashed arrows highlight the throughput yields, while black solid arrows indicate the  $I_{\text{SW}}$  values of reference detectors, providing context for assessing the performance of the newly fabricated devices against established standards. This significant achievement underscores the effectiveness of the PEALD technique in producing high-quality SNSPDs with consistent performance.<sup>102</sup>

Similar results have been reported for ALD-grown NbN<sup>107,176,177</sup> and TiN<sup>178</sup> detectors. The quest for higher-quality thin films, characterized by fewer defects, greater uniformity, and enhanced homogeneity, remains a fundamental goal in the preparation of superconducting nanowires. Furthermore, ALD holds potential for growing amorphous alloy superconductors, including WSi, MoSi, and MoGe, which could further enhance the fabrication of SNSPDs.

**5.2.2 Microwave resonators.** Microwave resonators are crucial in circuits, aiding in tasks like filtering and boosting electromagnetic wave interactions with quantum systems.<sup>179</sup> Superconducting materials greatly enhance their performance by reducing energy losses and increasing quality factors, allowing for flexible designs. The integration of Josephson junctions and SQUIDS<sup>180</sup> enables tunable frequencies, leading to wide applications in wave detection,<sup>181</sup> parametric amplification,<sup>182</sup> and quantum information processing.<sup>183</sup> Recent progress has improved coupling of these resonators with quantum objects, including qubits, spin ensembles magnons, nanomechanical resonators, and cold atoms.<sup>184–187</sup>

Most resonators have been made using low- $T_c$  superconducting materials like Nb, NbTi, NbN, NbTiN and TiN deposited through sputtering techniques.<sup>188–191</sup> To achieve uniform wafer-scale thin films, researchers now use ALD, which improves device performance by reducing microwave frequency losses.<sup>27,38,99</sup> ALD's precision enables higher quality factors, essential for sensitive applications like superconducting qubits and microwave kinetic inductance detectors (MKIDs), where low-loss resonators ensure better coherence times and signal stability.<sup>38,99</sup>

Shearrow *et al.*<sup>38</sup> reported high KI microwave resonators fabricated from 9 nm to 110 nm thick TiN films that are grown *via* ALD. Through a combination of the deposition method, resonator designs, and fabrication procedure, they achieve high

internal quality factors ( $Q_i$ ) exceeding one million at single photon powers for resonators on thicker TiN films. They designed a series of lumped element microwave resonators to verify that their TiN films are low-loss at microwave frequencies. Each film was patterned into resonators that incorporated a meandering inductor and an explicit capacitor to ground, as shown in Fig. 14(g). Each chip contained between eight and ten resonators, and these resonators were separated from a microwave feedline. The gap and pin width of the feedline was adjusted to match the 50  $\Omega$  impedance of the printed circuit board (PCB) and amplifier chain. All resonators on a single chip were designed with equal capacitance, meaning that the resonance frequency ( $f_0$ ) was varied by adjusting the length of the inductor, while keeping its width constant at 3  $\mu\text{m}$ .<sup>38</sup>

The authors studied resonators with TiN film thicknesses ranging from 8.9 nm to 109 nm, with their  $T_c$  detailed in Section 4. They plotted the internal quality factor ( $Q_i$ ) for four chips with different film thicknesses, as shown in Fig. 14(h). All resonators had  $Q_i$  values exceeding  $1.1 \times 10^5$ , with the highest values observed for the  $t = 49.8$  nm sample, where seven of ten resonators had  $Q_i(n_{\text{ph}} = 1) > 10^5$ . Most resonators, except those on the thinnest film ( $t = 8.9$  nm), showed increasing  $Q_i$  with power, suggesting  $Q_i$  is limited by two-level systems at 20 mK and  $n_{\text{ph}} = 1$ . For the thinnest film,  $Q_i$  was limited by suppressed superconductivity, but it still achieved  $Q_i \approx 10^5$ . To optimize the resonators for cavity QED experiments, the authors increased the characteristic impedance ( $Z$ ) to enhance the coupling strength ( $g$ ). They achieved this by using a meandering wire structure instead of a capacitor, relying on stray capacitance, as shown in Fig. 14(i). By reducing the wire width from 2  $\mu\text{m}$  to 75 nm, they significantly increased the impedance, improving the resonator's quantum performance. Fig. 14(j) shows the impedance and  $Q_i$  as a function of wire width for  $t = 8.9$  nm (red) and 14.2 nm (blue). The highest impedance,  $Z = 28$  k $\Omega$ , was achieved for the thinnest film and narrowest wire, boosting the coupling strength by 24 times compared to a standard 50  $\Omega$  resonator. Even the thickest film and widest wire achieved  $Z = 1.76$  k $\Omega$ , much higher than conventional resonators. Notably,  $Q_i$  remained stable across all wire widths, indicating the high impedance did not compromise resonator quality.

**5.2.3 Superconducting through-silicon vias.** Superconducting vias compatible with high-coherence qubits represent a crucial advancement toward larger quantum processors.<sup>192–195</sup> These vias are essential not only for routing but also for *via* stitching, which is necessary to shunt nominally grounded planes across different layers. This process helps control and elevates the frequencies of harmful parasitic microwave modes that can become problematic in large chips. However, traditional integrated circuit vias are designed for high normal-state conductivity and reduced parasitic capacitance rather than for superconductivity and extremely low microwave loss, which are critical for qubit compatibility. Additionally, integrating the fabrication of these vias with qubits presents challenges related to material compatibility and the low thermal budget of aluminum-based qubits.<sup>192–195</sup> ALD is vital for the growth of





these vias, providing precise control over film thickness and uniformity, crucial for enhancing superconducting properties and reducing microwave losses.

Grigoras *et al.*<sup>3</sup> developed superconducting through-silicon vias (TSVs) using a multi-step process. The process starts by depositing a tantalum electrode layer on a silicon wafer, followed by etching to form a hollow *via* with metallized walls. A metal membrane covers the *via*, and the backside is also metallized. TiN is applied to the TSV's inner walls using ALD, ensuring uniform coating to reduce microwave losses. The TSV structure includes an electrode layer, hollow *via* with metallized walls, a metal membrane covering the *via*, and a metallized back side. Fig. 15(a)–(c) displays SEM images and cross-sections showing the structure and integration of the TSV into the

device. Fig. 15(d)–(f) show various coplanar waveguide (CPW) resonator layouts incorporating TSVs, demonstrating how TSV design impacts device performance.

Grigoras *et al.* found that resonator chips with sparse TSV stitching achieved internal quality factors above  $10^6$  at single-photon powers. Fig. 15(g)–(i) show power dependence and  $Q_i$  measurements for these resonators, which perform similarly to planar reference resonators. The results indicate that transmon qubits on the same electrode layer can achieve state-of-the-art coherence without degrading qubit performance, even with TSVs. By comparing the best TSV chips to the best reference chips, which show similar performance, they affirm their findings. However, they acknowledge that certain uniformity and yield issues remain unresolved. Fig. 15(h) shows a

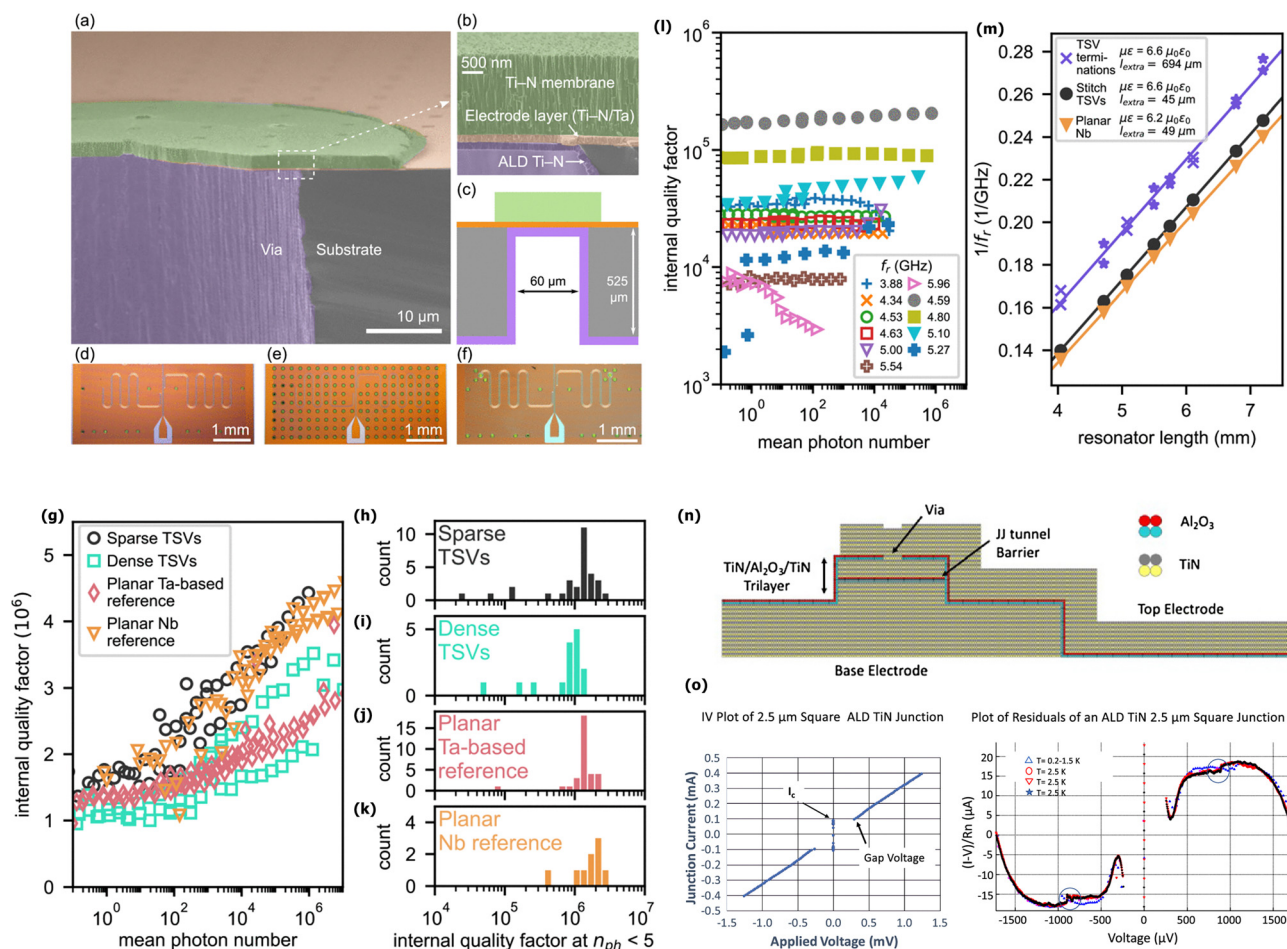


**Fig. 15** Superconducting through-silicon vias: (a) and (b) false-color scanning electron microscope images of a TSV. (c) Schematic cross section of TSV structure (not to scale), with color-coding as in (a) and (b). (d)–(f) Optical micrographs showing layouts of CPW test resonators with different densities and roles of TSVs (green circles). (d) Sparse *via* stitching. (e) Dense *via* stitching. (f) TSV-terminated resonators. Quality factor measurements for via-stitched TSV chips. (g) Measured  $Q_i$  at 10 mK as a function of photon number  $n_{ph}$  circulating in the resonator for resonators with sparse stitch TSVs (black circles), dense stitch TSVs (green squares), planar reference resonators with the same Ta-based electrode layer (diamonds), and planar reference resonators with an Nb electrode layer (triangles). (h)–(k) Histogram of measured internal quality factors at low photon numbers for all measured resonators of the types shown in panel (g). (l)  $Q_i$  vs.  $n_{ph}$  for TSV-terminated resonators. (m) Inverse resonance frequencies of several chips with TSV-terminated resonators (crosses and stars), resonator with sparse *via* stitching (circles), and reference Nb resonators (triangles) versus length of the coplanar part. Crosses (stars) indicate a TSV termination with three (four) ground vias around the terminating TSV. Solid lines indicate fits to (l) with parameters given in the legend.<sup>3</sup> Copyright 2022, IEEE Publishing. (n) Sketch of a crosssection of a TiN Josephson Junction. (o) Left is a current–voltage plot of an ALD Josephson Junction. The measured tunneling current is 100  $\mu$ A. The gap voltage is observed at 320  $\mu$ V. Right is a plot of the above-gap region with the resistive component subtracted, showing the possibility of a second gap (circled) near 900  $\mu$ V.<sup>5</sup> Copyright 2020, Springer Publishing.



small fraction of outlier resonators with anomalously low quality factors, which are relatively independent of power. These outliers are occasionally found in both the Ta- and Nb-based planar reference devices. Furthermore, resonators near the edges of the 150 mm wafers demonstrate  $Q_i$  values below  $10^6$ , even for the sparse TSV design. The study also reports a decline in  $Q_i$  for chips with dense TSVs and TSV-terminated resonators, which showed internal quality factors ranging from  $10^4$  to  $2 \times 10^5$ , see Fig. 15(l). These resonators exhibited asymmetrical line shapes at lower photon numbers, linked to weak superconducting spots in the ALD TiN, causing  $Q_i$  to decrease as current approached the critical level.

Despite these challenges, the best-performing TSV-terminated resonators matched the performance of TSV-interrupted devices. Additionally, the resonance frequencies were consistent with other designs after accounting for an added CPW-equivalent length of approximately 650  $\mu\text{m}$ , see Fig. 15(m). The measurements aligned well with theoretical predictions, showing only minor deviations. Furthermore, the tantalum-based electrode layer exhibited low kinetic inductance, demonstrating its compatibility with niobium-based superconducting qubits.

**5.2.4 Josephson junction.** The second quantum revolution is currently unfolding, and it is crucial to harness the broad applications of superconducting quantum devices.<sup>196</sup> One key component is the Josephson junction, which consists of two superconductors separated by a thin insulating barrier, only a few nanometers thick. This tunnel junction, known for its low loss and strong nonlinearity, plays a vital role in various quantum devices, including superconducting qubits, single microwave photon detectors, and quantum-limited amplifiers.<sup>197–199</sup> Since the qubit's frequency is directly related to the junctions normal-state resistance ( $R_N$ ), variations in  $R_N$  can cause frequency collisions between qubits in multi-qubit systems. Moreover, non-uniform critical current can introduce unwanted reflections in Josephson traveling wave parametric amplifiers, degrading device performance.<sup>200</sup> Therefore, achieving high uniformity and stability in Josephson junctions at the wafer scale using standard fabrication techniques is essential for advancing quantum technologies.

Josephson junctions can be fabricated using several deposition methods, including sputtering,<sup>201</sup> electron beam lithography,<sup>202,203</sup> *in situ* combined magnetron sputtering and ALD,<sup>204,205</sup> and more recently, standalone ALD.<sup>5</sup> ALD, in particular, enables the production of highly uniform and defect-free thin films at the wafer level, which are critical for the effective operation of Josephson junctions.

The fabrication of Josephson junctions from ALD grown trilayer of TiN/ $\text{Al}_2\text{O}_3$ /TiN at 450 °C with thicknesses of 1500 Å/10 Å/500 Å reported by Jhabvala *et al.*<sup>5</sup> The base electrode and junction were deposited in a single run, followed by photolithographic patterning and inductively coupled plasma etching. Fig. 15(n) illustrates the structure of a completed TiN Josephson junction, showing a cross-sectional sketch of the junction. The Josephson junctions were tested at cryogenic temperatures using an adiabatic demagnetization refrigeration system with a base temperature of 100 mK. Their TiN's superconducting transition temperature was 3.4 K. For a 2.5  $\mu\text{m}$

square Josephson junction, they measured a critical current ( $I_c$ ) of 100  $\mu\text{A}$ , yielding a calculated critical current density of approximately 500  $\text{A cm}^{-2}$ , see Fig. 15 (o-left). The measured gap voltage was 320  $\mu\text{V}$ , lower than the expected 900  $\mu\text{V}$  based on BCS theory, see Fig. 15 (o-right). This led the authors to hypothesize the existence of multiple superconducting transitions in the TiN films.<sup>5</sup>

### 5.3 Interesting potential applications

**5.3.1 SIS coatings for SRF cavities.** The Superconductor-Insulator-Superconductor (SIS) structure enhances the performance of superconducting radio frequency (SRF) cavities.<sup>206–209</sup> While niobium (Nb) is the dominant material due to its favorable properties, the SIS configuration, consisting of alternating superconducting (S) and insulating (I) nanometric layers, enables higher maximum operation gradients ( $E_{\text{max}}$ ).<sup>6,40,210</sup> When the superconducting layer thickness ( $d_S$ ) is much smaller than its penetration depth ( $\lambda$ ), the cavity can support elevated magnetic fields beyond bulk Nb limits. The insulating layer inhibits vortex penetration and must be thick enough to avoid Josephson junction effects. The use of high energy gap superconductors, like NbTiN, reduces BCS resistance, and optimized SIS structures can significantly increase  $Q$ -values and external magnetic fields. This multilayer approach can boost  $E_{\text{max}}$  by 20% to 100% compared to Nb, promising substantial cost savings for accelerators, although challenges persist in achieving high-quality layers and understanding surface effects.<sup>206–208</sup>

ALD plays a crucial role in coating SIS structures because of its ability to deliver uniform deposition on intricate geometries. Unlike other deposition techniques, ALD is a self-limiting process that allows precise control of atomic-level thickness without requiring a direct line of sight to the substrate. This makes it particularly well-suited for coating nanostructured surfaces, despite its slower deposition rates. Recent progress has showcased the successful deposition of insulating layers *via* ALD in 1.3 GHz cavities.<sup>8,156,163,164</sup> Although ALD encounters difficulties in producing metallic superconductors, there has been notable advancement with materials like NbN, NbTiN, MoN, and TiN on planar samples. Kalboussi *et al.*<sup>113,163,164</sup> have already fabricated SIS structures using ALD, and ongoing studies are focused on improving the RF performance of SIS-coated cavities. Beyond superconducting alloys, ALD's precision and capabilities extend to other applications, such as reducing secondary electron yield, creating diffusion barriers, developing dopant sources, and enhancing the adhesion and stability of coatings on copper. Moreover, ALD can be used to engineer intermediate layers that accommodate differences in thermal expansion, further boosting the performance of SRF cavities.<sup>210</sup>

**5.3.2 Other applications.** Looking ahead, ALD holds significant promise for advancing superconducting thin films in a range of emerging applications. In infrared sensors,<sup>211</sup> ALD's precision in creating defect-free films could greatly enhance sensitivity for thermal imaging, environmental monitoring, and astronomy.<sup>212</sup> For quantum circuits, the need for



high-quality superconducting materials, like NbN and TiN, will be met by ALDs ability to fabricate qubits and quantum gates with longer coherence times and greater reliability.<sup>2,213,214</sup> Its capacity to deposit uniform films on complex geometries will also benefit magnetic bearings and separation systems, supporting frictionless, energy-efficient industrial processes.<sup>215,216</sup> In chip interconnects,<sup>217</sup> ALDs precise deposition techniques will be critical for developing superconducting interconnects that reduce signal loss, key for quantum computing and next-generation microchips. Furthermore, in MRI systems, ALD can significantly improve detector sensitivity and resolution through its control over superconducting film properties. As ALD technology evolves, its role in enabling advancements in quantum technology, medical diagnostics, and industrial systems will become increasingly pivotal.

## 6 Prospect, future challenges and conclusive remarks

### 6.1 Prospect

The future of ALD in the fabrication of superconducting thin films holds immense promise for transforming various high-tech fields, including quantum computing, energy-efficient electronics, and advanced sensing technologies. ALD's key advantage lies in its ability to produce ultra-thin films with atomic precision, uniformity, and excellent conformality, even on complex geometries. This capability is critical for the development of superconducting devices, where the thickness, composition, and interface quality of films directly influence performance characteristics such as critical temperature, electrical resistance, and current-carrying capacity.

As research in ALD continues to advance, the technology has the potential to enable the integration of superconducting thin films into compact, high-performance devices. The development of new superconducting materials with higher critical temperatures, combined with ALDs precision, can lead to breakthroughs in fields like quantum computing, where ultra-sensitive devices like qubits rely on the stability and uniformity that ALD can provide. Additionally, the scalability of ALD offers opportunities for large-area deposition, essential for commercializing superconducting technologies in energy systems and medical applications, such as in superconducting magnets for MRI machines or advanced power grids.

Moreover, with further refinement in ALD precursor chemistry, especially for complex superconductors, and the integration of hybrid techniques, ALD is set to expand the range of materials and devices it can be used for. The continued evolution of ALD will play a pivotal role in the next generation of superconducting materials, potentially driving innovations that can lead to more energy-efficient electronics, faster computational devices, and more sensitive magnetic sensors.

Another important avenue for future research on ALD-grown superconducting thin films is the need for a thorough investigation of their superconducting parameters beyond the transition temperature. While  $T_c$  is well-documented, other critical

properties such as the critical magnetic field ( $H_c$ ), superconducting gap  $\Delta$ , surface resistance, London penetration depth, and coherence length remain largely unexplored for ALD films. These parameters are vital for assessing the full potential of ALD-deposited films in practical applications. The review by Anne-Marie Valente-Feliciano<sup>6</sup> offers a comprehensive analysis of these superconducting parameters for films grown *via* other deposition methods, demonstrating the detailed characterization available for non-ALD techniques. Conducting similar studies for ALD-grown films would bridge this knowledge gap, enabling direct comparisons between ALD and other deposition methods. A systematic exploration of these parameters, including their dependence on film thickness, and deposition conditions, would offer valuable insights into optimizing ALD for high-performance superconducting materials. Addressing this gap will enhance the understanding of ALD-grown films and expand their potential applications in advanced superconducting technologies.

Furthermore, strain engineering has proven to be a powerful tool for enhancing the superconducting properties of thin films, especially in materials deposited by techniques such as PLD,<sup>218</sup> HPCVD,<sup>219</sup> and CSD.<sup>220</sup> By inducing strain through lattice mismatch between the substrate and the thin film, it is possible to manipulate key superconducting parameters like  $T_c$ ,  $H_c$  and  $J_c$ . Despite its success in other deposition methods, strain engineering has yet to be explored extensively in ALD-grown superconducting films. Given ALD's remarkable ability to deposit highly uniform, conformal, and precise layers, integrating strain into ALD processes, as already shown for non-superconductive materials,<sup>221–223</sup> could provide a new path for tuning superconducting properties. Investigating parameters such as substrate selection, deposition temperature, and post-deposition annealing could help tailor the lattice strain, leading to improvements in superconductivity.

### 6.2 Future challenges

**6.2.1 Material complexity.** One of the primary challenges in applying ALD to superconducting thin films lies in the intrinsic complexity of these materials, particularly high-temperature superconductors (HTS) with intricate crystal structures, such as cuprates and iron-based superconductors.<sup>224,225</sup> These materials exhibit complex phase behavior, where multiple competing phases can form during growth, complicating the deposition process. Optimizing ALD for such systems requires extensive research into precursor chemistry and fine-tuning of deposition parameters to achieve precise phase and composition control. High-temperature superconductors, for instance, often feature multi-component oxide structures that demand strict stoichiometric control over elements like copper, oxygen, and rare earths.<sup>226</sup> Given ALDs sequential precursor delivery, achieving this level of control presents significant challenges. Similarly, the supercycle ALD processes such as for NbTiN, which involves alternating NbN and TiN sub-cycles, exemplifies the difficulties in depositing multicomponent superconducting films. While this approach enables precise composition control and uniform deposition, the inherent material complexity introduces additional challenges in



achieving optimal superconducting properties. Small deviations in the Nb-to-Ti ratio can significantly affect the superconducting transition temperature and resistivity. Furthermore, ALDs inherently slow deposition rate—exacerbated by the need for multiple sub-cycles—makes maintaining consistent film quality over large areas difficult.<sup>34,40</sup> Variations in precursor reactivity and diffusion further complicate the uniform incorporation of Nb and Ti, potentially leading to phase inhomogeneities that degrade performance. Addressing these issues requires deeper investigation into precursor chemistry and reaction mechanisms to refine ALD processes for these complex materials and ensure the high crystallinity essential for superconductivity.

**6.2.2 Plasma.** A significant number of superconducting thin films are deposited using PEALD due to its enhanced reactivity and lower deposition temperatures. However, the use of plasma introduces several challenges that must be addressed to achieve optimal film quality. One major concern is plasma-induced damage, particularly in sensitive materials, where high-energy ions and radicals can create defects, alter film stoichiometry, or introduce unwanted impurities. Another challenge is deposition non-uniformity in complex 3D structures, as plasma species may have limited penetration into high aspect ratio features, leading to variations in film thickness and composition. Additionally, precise control over plasma parameters such as power, gas composition, and exposure time is crucial, as even slight variations can significantly impact film properties. To overcome these challenges, optimizing plasma conditions is essential. Strategies such as employing low-energy plasmas, remote plasma configurations, or pulsed plasma techniques can help minimize damage. Improved reactor designs that enhance plasma uniformity and precursor delivery can also mitigate non-uniform deposition issues. Furthermore, advanced *in situ* monitoring techniques provide real time feedback, allowing fine tuning of plasma parameters to ensure consistent and high-quality film growth. Addressing these challenges will enable PEALD to be further optimized for high-performance applications in superconducting films, semiconductors, and other advanced material systems.

**6.2.3 Interface Quality.** The quality of the interface between the superconducting thin film and its underlying substrate is another critical factor influencing the film's performance. In superconducting thin films, the film-substrate interface can introduce strain or defects that alter the films superconducting properties, particularly its critical temperature. Imperfections at the interface, such as poor adhesion, roughness, or mismatch in thermal expansion, can create localized non-superconducting regions or degrade the uniformity of the superconducting phase. Ensuring a high-quality interface requires not only precise control of the ALD process but also careful selection and preparation of the substrate material. Additionally, the interaction between the film and the substrate at the atomic level must be optimized to minimize the formation of defects or unwanted phases. This is particularly important in applications such as quantum computing, where even small imperfections at the interface can lead to significant performance degradation.

**6.2.4 Scalability.** ALD is inherently scalable due to its sequential deposition process, which can coat large and complex surface areas with uniform films. However, the challenge lies in maintaining the quality and uniformity of superconducting films as the process is scaled to larger areas or integrated into complex device architectures. As superconducting devices shrink in size and become more complex, the demand for high-quality, defect-free films across large surface areas grows. The difficulty of ensuring uniform film thickness, composition, and crystallinity over large substrates, particularly in high-throughput industrial applications, presents a significant challenge. Moreover, as device architectures become more intricate, integrating ALD-deposited superconducting films into these structures without compromising their performance requires advanced process control and integration strategies. Ensuring that ALD can consistently deliver high-quality films at an industrial scale is critical for the widespread adoption of superconducting thin films in practical applications.

**6.2.5 Development of new precursors.** A key area of research focuses on developing novel precursors that not only enhance existing ALD processes but also enable the synthesis of materials previously unattainable due to the lack of suitable precursors. Many current ALD precursors require elevated temperatures, limiting their compatibility with temperature-sensitive substrates. This is particularly critical for superconducting films, where high temperatures can degrade both their superconducting properties and the integrity of the substrates. The lack of suitable precursors remains a major challenge for the successful ALD synthesis of  $\text{MgB}_2$ . Unlike transition metal oxides, which benefit from a broad range of volatile and reactive precursors,  $\text{MgB}_2$  requires precursors that ensure the precise incorporation of both Mg and B while maintaining ALDs self-limiting growth characteristics. Key challenges include precursor thermal stability, volatility, and reactivity with co-reactants such as plasma species. Additionally, achieving the correct stoichiometry is critical, as deviations in the Mg:B ratio can significantly impact superconducting properties. Notably, the ALD of  $\text{MgB}_2$  has been reported only once, in a patent by scientists from Argonne National Laboratory,<sup>227</sup> where bis(cyclopentadienyl) magnesium(II)  $\text{Mg}(\text{Cp})_2$ , water, and Trimethyl borate  $\text{B}(\text{OCH}_3)_3$  were used to deposit  $\text{MgB}_2$  and  $\text{MgB}_2$ -containing films that exhibited superconducting properties above 20 K. Despite this work being reported over a decade ago, no further work on  $\text{MgB}_2$  ALD have emerged, either from the original researchers or elsewhere. Similarly, the ALD synthesis of  $\text{Nb}_3\text{Sn}$ , another promising superconducting material, has faced significant challenges due to the absence of suitable precursors that can facilitate low-temperature deposition while maintaining precise stoichiometry. Overcoming the limitations of  $\text{MgB}_2$  and  $\text{Nb}_3\text{Sn}$  ALD through precursor design and alternative approaches—such as plasma-enhanced ALD or hybrid ALD-CVD processes—could pave the way for the successful fabrication of these superconducting thin films with enhanced performance. Furthermore, the development of novel precursors remains crucial for expanding ALD technology to a broader range of superconducting and other advanced



materials. These precursors must be chemically stable, easy to handle, and capable of producing high-purity films with precise stoichiometry, ensuring reliability and quality in both existing and newly feasible ALD processes. Advancing precursor chemistry could also open new avenues for the synthesis of novel superconducting materials with exceptional properties.

**6.2.6 *In situ* characterization.** Real-time, *in situ* characterization techniques are essential for optimizing film growth, ensuring reproducibility, and accurately assessing the superconducting properties of deposited films. Current ALD processes rely on post-deposition analysis to evaluate film properties, which can result in lengthy optimization cycles. *In situ* techniques, such as spectroscopic ellipsometry, quartz crystal microbalance (QCM), *in situ* XRD, or *in situ* resistivity measurements, would allow researchers to monitor film growth in real-time, providing immediate feedback on parameters such as film thickness, composition, crystallinity, and electrical properties critical to superconductivity. This approach enables precise control over the deposition process, ensuring that superconducting films meet the required specifications for critical applications. Furthermore, *in situ* characterization could help detect and correct any deviations in the films growth, such as the formation of unwanted phases, defects, or variations in superconducting properties, before they impact the overall quality and performance of the film.

**6.2.7 Integrating deposition techniques.** A promising approach to overcoming the limitations of ALD in superconducting film fabrication is its integration with other deposition techniques, such as sputtering. This method is particularly effective for coating SIS Nb–Al/ALD–Al<sub>2</sub>O<sub>3</sub>/Nb Josephson tunnel junctions using an integrated ALD-UHV sputtering system.<sup>204,205</sup> By combining deposition techniques, researchers can leverage the strengths of each method to enhance film properties and improve deposition rates. While ALD offers exceptional atomic precision and uniformity, its slow deposition speed can be a drawback. In contrast, sputtering enables much faster film deposition but may lack the conformality and precision of ALD. The integration of these techniques allows for the optimization of film quality while increasing throughput. Furthermore, hybrid approaches facilitate the deposition of multilayer structures or heterostructures, enabling the seamless combination of superconducting and non-superconducting layers to enhance device performance. This strategy holds significant potential for developing complex, multifunctional superconducting devices, overcoming the limitations of individual deposition methods, and expanding the applications of superconducting materials.

## 7. Conclusive remarks

This comprehensive review has highlighted the significant advancements and potential of ALD in the fabrication of superconducting thin films. ALD's ability to offer atomic-scale precision, excellent uniformity, and conformality over complex geometries makes it a highly promising technique for developing

high-performance superconducting materials. These characteristics are particularly crucial for applications in quantum computing, superconducting electronics, and advanced sensing technologies, where the precise control of material properties is essential for device performance.

Despite its numerous advantages, several challenges remain that need to be addressed to fully realize the capabilities of ALD in this field. The complexity of depositing high-temperature superconductors, which often have intricate crystal structures, requires further optimization of both ALD processes and precursor chemistry. Similarly, ensuring high-quality interfaces between superconducting films and substrates is critical for preserving superconducting properties such as  $T_c$  and low electrical resistance. Furthermore, while ALD is inherently scalable, maintaining the quality of superconducting films over large areas and within increasingly complex device architectures remains a significant technical challenge.

Looking forward, addressing these challenges will require continued innovation in precursor development, the integration of advanced *in situ* characterization techniques for real-time monitoring, and exploration of hybrid deposition methods to enhance deposition rates and film properties. The development of low-temperature ALD processes, in particular, will expand the range of substrates and applications for these films, potentially transforming industries that rely on superconducting technology.

In conclusion, while ALD has already demonstrated its potential to significantly advance the field of superconducting thin films, further research and technological innovations will be essential to overcome existing limitations. As these challenges are addressed, ALD is poised to play an increasingly pivotal role in the development of future superconducting materials, enabling breakthroughs in quantum technologies, energy-efficient systems, and next-generation electronics.

## Data availability

No primary research results, software or code has been included and no new data were generated or analysed as part of this review.

## Conflicts of interest

The authors declare no competing interests.

## Acknowledgements

This work was supported by the BMBF under the research grants 05H21GURB2 and 05K22GUD.

## References

- 1 R. L. Fagaly, *Rev. Sci. Instrum.*, 2006, 77(10), 101101.
- 2 I. Siddiqi, *Nat. Rev. Mater.*, 2021, 6, 875–891.





- 3 K. Grigoros, N. Yurttagül, J.-P. Kaikkonen, E. T. Mannila, P. Eskelinen, D. Lozano, H.-X. Li, M. Rommel, D. Shiri and N. Tiencken, *et al.*, *IEEE Trans. Quant. Eng.*, 2022, **3**, 1–10.
- 4 A. Krasnok, P. Dhakal, A. Fedorov, P. Frigola, M. Kelly and S. Kutsaev, *Appl. Phys. Rev.*, 2024, **11**(1), 011302.
- 5 C. A. Jhabvala, P. C. Nagler and T. R. Stevenson, *J. Low Temp. Phys.*, 2020, **200**, 331–335.
- 6 A.-M. Valente-Feliciano, *Supercond. Sci. Technol.*, 2016, **29**, 113002.
- 7 J. A. Oke and T.-C. Jen, *J. Mater. Res. Technol.*, 2022, **21**, 2481–2514.
- 8 G. K. Deyu, T. Parikh, M. Wenskat, I. Gonzalez Diaz-Palacio, R. H. Blick, R. Zierold and W. Hillert, *Chem. Mater.*, 2024, **36**, 2846–2856.
- 9 M. Wenskat, G. K. Deyu, I. G. Daz-Palacio, R. H. Blick, R. Zierold and W. Hillert, *Supercond. Sci. Technol.*, 2022, **36**, 015010.
- 10 P.-G. De Gennes, *Superconductivity of metals and alloys*, CRC Press, 2018.
- 11 M. Tinkham, *Introduction to superconductivity*, Courier Corporation, 2004.
- 12 W. Meissner and R. Ochsenfeld, *Naturwissenschaften*, 1933, **21**, 787–788.
- 13 F. London and H. London, *Proc. R. Soc. A*, 1935, **149**, 71–88.
- 14 C. J. Gorter and H. Casimir, *Z. Tech. Phys.*, 1934, **15**, 539–542.
- 15 J. Bardeen, L. N. Cooper and J. R. Schrieffer, *Phys. Rev.*, 1957, **108**, 1175.
- 16 H. Padamsee, J. Knobloch and T. Hays, *RF superconductivity for accelerators*, John Wiley & Sons, 2008.
- 17 W. Singer, A. Ermakov and X. Singer, *TTC Rep.*, 2010, **2**, 02.
- 18 S. M. George, *Chem. Rev.*, 2010, **110**, 111–131.
- 19 R. L. Puurunen, *J. Appl. Phys.*, 2005, **97**, 9.
- 20 H. Profijt, S. Potts, M. Van de Sanden and W. Kessels, *J. Vac. Sci. Technol., A*, 2011, **29**(5), 050801.
- 21 G. K. Deyu, J. Hunka, H. Roussel, J. Brötz, D. Bellet and A. Klein, *Materials*, 2019, **12**, 2232.
- 22 V. Cremers, R. L. Puurunen and J. Dendooven, *Appl. Phys. Rev.*, 2019, **6**(2), 021302.
- 23 M. Weidner, A. Fuchs, T. J. Bayer, K. Rachut, P. Schnell, G. K. Deyu and A. Klein, *Adv. Funct. Mater.*, 2019, **29**, 1807906.
- 24 T. J. Bayer, A. Wachau, A. Fuchs, J. Deuermeier and A. Klein, *Chem. Mater.*, 2012, **24**, 4503–4510.
- 25 R. W. Johnson, A. Hultqvist and S. F. Bent, *Mater. Today*, 2014, **17**, 236–246.
- 26 T. Proslir, Atomic Layer Deposition of Thin Superconducting Films and Multilayers: Coupons and Cavity Tests, *SRF*, JACoW Publishing, 2013, [https://accelconf.web.cern.ch/srf2013/talks/weioc03\\_talk.pdf](https://accelconf.web.cern.ch/srf2013/talks/weioc03_talk.pdf).
- 27 P. Coumou, M. Zuiddam, E. Driessen, P. De Visser, J. Baselmans and T. Klapwijk, *IEEE Trans. Appl. Supercond.*, 2012, **23**, 7500404.
- 28 R. L. Puurunen, *Chem. Vap. Deposition*, 2003, **9**, 249–257.
- 29 E. Knehr, M. Ziegler, S. Linzen, K. Ilin, P. Schanz, J. Plentz, M. Diegel, H. Schmidt, E. Ilichev and M. Siegel, *J. Vac. Sci. Technol., A*, 2021, **39**, 052401.
- 30 L. Hiltunen, M. Leskelä, M. Mäkelä, L. Niinistö, E. Nykänen and P. Soininen, *Thin Solid Films*, 1988, **166**, 149–154.
- 31 T. Proslir, J. Klug, N. C. Becker, J. W. Elam and M. Pellin, *ECS Trans.*, 2011, **41**, 237.
- 32 J. A. Klug, T. Proslir, J. W. Elam, R. E. Cook, J. M. Hiller, H. Claus, N. G. Becker and M. J. Pellin, *J. Phys. Chem. C*, 2011, **115**, 25063–25071.
- 33 N. R. Groll, J. A. Klug, C. Cao, S. Altin, H. Claus, N. G. Becker, J. F. Zasadzinski, M. J. Pellin and T. Proslir, *Appl. Phys. Lett.*, 2014, **104**(9), 092602.
- 34 Y. Kalboussi, B. Delatte, F. Miserque, D. Dragoe, M. Asaduzzaman, L. Maurice, M. Baudrier, G. Jullien, C. Boulch, T. Vacher *et al.* 21th International Conference on RF Superconductivity (SRF'23), Grand Rapids, MI, USA, 25–30 June 2023, 2023, pp. 615–620.
- 35 A. Tamm, A. Tarre, V. Verchenko, H. Seemen and R. Stern, *Crystals*, 2020, **10**, 650.
- 36 P. R. Kärkkäinen, G. Popov, T. Hatanpää, A. Kemppinen, K. Kohopää, M. Bagheri, H.-P. Komsa, M. Heikkilä, K. Mizohata and M. Chundak, *et al.*, *Adv. Mater. Interfaces*, 2024, **11**, 2400270.
- 37 D. R. Boris, V. D. Wheeler, N. Nepal, S. B. Qadri, S. G. Walton and C. C. R. Eddy, *J. Vac. Sci. Technol., A*, 2020, **38**(4), 040801.
- 38 A. Shearrow, G. Koolstra, S. J. Whiteley, N. Earnest, P. S. Barry, F. J. Heremans, D. D. Awschalom, E. Shirokoff and D. I. Schuster, *Appl. Phys. Lett.*, 2018, **113**(21), 212601.
- 39 L. Tian, I. Bottala-Gambetta, V. Marchetto, M. Jacquemin, A. Crisci, R. Reboud, A. Mantoux, G. Berthomé, F. Mercier and A. Sulpice, *et al.*, *Thin Solid Films*, 2020, **709**, 138232.
- 40 I. González Daz-Palacio, M. Wenskat, G. K. Deyu, W. Hillert, R. H. Blick and R. Zierold, *J. Appl. Phys.*, 2023, **134**(3), 035301.
- 41 A. Bertuch, B. D. Keller, N. Ferralis, J. C. Grossman and G. Sundaram, *J. Vac. Sci. Technol., A*, 2017, **35**(1), 01B141.
- 42 H. H. Sønsteby, T. Aarholt, Ø. Prytz, H. Fjellvåg and O. Nilsen, *Chem. Commun.*, 2018, **54**, 8253–8256.
- 43 D. Munoz-Rojas and J. MacManus-Driscoll, *Mater. Horiz.*, 2014, **1**, 314–320.
- 44 A. Y. Kovalgin, M. Yang, S. Banerjee, R. O. Apaydin, A. A. Aarnink, S. Kinge and R. A. Wolters, *Adv. Mater. Interfaces*, 2017, **4**, 1700058.
- 45 J. Park, S. J. Kwak, S. Kang, S. Oh, B. Shin, G. Noh, T. S. Kim, C. Kim, H. Park and S. H. Oh, *et al.*, *Nat. Commun.*, 2024, **15**, 2138.
- 46 G. K. Deyu, D. Muñoz-Rojas, L. Rapenne, J.-L. Deschanvres, A. Klein, C. Jiménez and D. Bellet, *Molecules*, 2019, **24**, 2797.
- 47 J. A. Oke and T.-C. Jen, *J. Mater. Res. Technol.*, 2022, **21**, 2481–2514.
- 48 C. Lohaus, C. Steinert, G. Deyu, J. Brötz, W. Jaegermann and A. Klein, *Appl. Phys. Lett.*, 2018, **112**(15), 152105.
- 49 M. N. Sayeed, U. Pudasaini, C. E. Reece, G. Ereemeev and H. E. Elsayed-Ali, *J. Alloys Compd.*, 2019, **800**, 272–278.



- 50 A. Saito, A. Kawakami, H. Shimakage and Z. Wang, *Jpn. J. Appl. Phys.*, 2002, **41**, L127.
- 51 A. E. Dane, A. N. McCaughan, D. Zhu, Q. Zhao, C.-S. Kim, N. Calandri, A. Agarwal, F. Bellei and K. K. Berggren, *Appl. Phys. Lett.*, 2017, **111**, 122601.
- 52 S. Zhang, C.-Y. Deng, X. Wang, Y.-P. Wu, Y. Fu and X.-H. Fu, *Thin Solid Films*, 2015, **584**, 300–304.
- 53 X. Xi, A. Pogrebnyakov, S. Xu, K. Chen, Y. Cui, E. Maertz, C. Zhuang, Q. Li, D. Lamborn, J. Redwing, Z. Liu, A. Soukiassian, D. Schlom, X. Weng, E. Dickey, Y. Chen, W. Tian, X. Pan, S. Cybart and R. Dynes, *Phys. C*, 2007, **456**, 22–37.
- 54 K. Endo, H. Yamasaki, S. Misawa, S. Yoshida and K. Kajimura, *Nature*, 1992, **355**, 327–328.
- 55 S. Ueda, T. Yamagishi, S. Takeda, S. Agatsuma, S. Takano, A. Mitsuda and M. Naito, *Phys. C*, 2011, **471**, 1167–1173.
- 56 Y. Harada, M. Uduka, Y. Nakanishi, N. Yoshimoto and M. Yoshizawa, *Phys. C*, 2004, **412–414**, 1383–1386.
- 57 M. E. Yakinci, Z. D. Yakinci, M. A. Aksan and Y. Balci, *Cryogenics*, 2012, **52**, 749–754.
- 58 M. Kawai, T. Kawai, H. Masuhira and M. Takahashi, *Jpn. J. Appl. Phys.*, 1987, **26**, L1740.
- 59 A. Yasuda, K. Moriya, S. Takahashi, S. Abiko, Y. Narita, G. Abe, K. Tanaka and T. Sasaki, *Phase Transitions*, 2021, **94**, 910–917.
- 60 K. Moriya, K. Igarashi, H. Watanabe, H. Hasegawa, T. Sasaki and A. Yasuda, *Results Phys.*, 2018, **11**, 364–367.
- 61 V. Grosse, C. Pansow, A. Steppke, F. Schmidl, A. Undisz, M. Rettenmayr, A. Grib and P. Seidel, *J. Phys.: Conf. Ser.*, 2010, 012015.
- 62 T. Kobayashi, H. Ogawa, F. Nabeshima and A. Maeda, *Superconductor Science and Technology*, 2022, **35**, 07LT01.
- 63 M. Falter, W. Häßler, B. Schlobach and B. Holzapfel, *Phys. C*, 2002, **372**, 46–49.
- 64 M. Chae, M. Simnad, M. Maple, S. Anders, A. Anders and I. Brown, *Phys. C*, 1996, **270**, 173–179.
- 65 J. Langner, M. Sadowski, P. Strzyzewski, R. Mirowski, J. Witkowski, S. Tazzari, L. Catani, A. Cianchi, J. Lorkiewicz, R. Russo, T. Paryczak, J. Rogowski and J. Sekutowicz, 2006 International Symposium on Discharges and Electrical Insulation in Vacuum, 2006, pp. 535–538.
- 66 D. Papaconstantopoulos, W. Pickett, B. Klein and L. Boyer, *Phys. Rev. B: Condens. Matter Mater. Phys.*, 1985, **31**, 752.
- 67 N. Pessall, R. Gold and H. Johansen, *J. Phys. Chem. Solids*, 1968, **29**, 19–38.
- 68 Y. Zou, X. Qi, C. Zhang, S. Ma, W. Zhang, Y. Li, T. Chen, X. Wang, Z. Chen and D. Welch, *et al.*, *Sci. Rep.*, 2016, **6**, 22330.
- 69 J. Zasadzinski, R. Vaglio, G. Rubino, K. Gray and M. Russo, *Phys. Rev. B: Condens. Matter Mater. Phys.*, 1985, **32**, 2929.
- 70 I. Pentin, Y. Vakhtomin, V. Seleznev and K. Smirnov, *Sci. Rep.*, 2020, **10**, 16819.
- 71 B. Johansson, J.-E. Sundgren, J. Greene, A. Rockett and S. Barnett, *J. Vac. Sci. Technol.*, A, 1985, **3**, 303–307.
- 72 K. Ilin, M. Hofherr, D. Rall, M. Siegel, A. Semenov, A. Engel, K. Inderbitzin, A. Aeschbacher and A. Schilling, *J. Low Temp. Phys.*, 2012, **167**, 809–814.
- 73 K. Reichelt, W. Nellen and G. Mair, *J. Appl. Phys.*, 1978, **49**, 5284–5287.
- 74 M. Müller, R. Hoepfl, L. Liensberger, S. Geprägs, H. Huebl, M. Weiler, R. Gross and M. Althammer, *Mater. Quantum Technol.*, 2021, **1**, 045001.
- 75 A. Bezing, K. Yvon, J. Muller, W. Lengaeur and P. Ettmayer, *Solid State Commun.*, 1987, **63**, 141–145.
- 76 W. Lu, H. Zhai, Q. Li and C. Chen, *J. Phys. Chem. Lett.*, 2021, **12**, 1985–1990.
- 77 J. Femi-Oyetoro, S. Sypkens, H. LeDuc, M. Dickie, A. Beyer, P. Day and F. Greer, *Appl. Phys. Lett.*, 2024, **125**(6), 062601.
- 78 A. A. Hossain, H. Wang, D. S. Catherall, M. Leung, H. Knoop, J. R. Renzas and A. J. Minnich, *J. Vac. Sci. Technol.*, A, 2023, **41**(6), 062601.
- 79 K. Grigoros, S. Simbierowicz, L. Grönberg, J. Govenius, V. Vesterinen, M. Prunnila and J. Hassel, 2019 IEEE 21st Electronics Packaging Technology Conference (EPTC), 2019, pp. 81–82.
- 80 E. F. Driessen, P. Coumou, R. Tromp, P. De Visser and T. Klapwijk, *Phys. Rev. Lett.*, 2012, **109**, 107003.
- 81 W. Escoffier, C. Chapelier, N. Hadacek and J.-C. Villégier, *Phys. Rev. Lett.*, 2004, **93**, 217005.
- 82 S. Wang, D. Antonio, X. Yu, J. Zhang, A. L. Cornelius, D. He and Y. Zhao, *Sci. Rep.*, 2015, **5**, 13733.
- 83 D. Papaconstantopoulos, W. Pickett, B. Klein and L. Boyer, *Nature*, 1984, **308**, 494.
- 84 W. Pickett, B. Klein and D. Papaconstantopoulos, *Phys. B+C*, 1981, **107**, 667–668.
- 85 K. Balasubramanian, L. Huang and D. Gall, *J. Appl. Phys.*, 2017, **122**(19), 195101.
- 86 H. Jehn and P. Ettmayer, *J. Less-Common Met.*, 1978, **58**, 85–98.
- 87 N. Savvides, *J. Appl. Phys.*, 1987, **62**, 600–610.
- 88 K. Inumaru, K. Baba and S. Yamanaka, *Phys. Rev. B: Condens. Matter Mater. Phys.*, 2006, **73**, 052504.
- 89 F. F. Klimashin, N. Koutná, H. Euchner, D. Holec and P. H. Mayrhofer, *J. Appl. Phys.*, 2016, **120**(18), 185301.
- 90 I. Jauberteau, A. Bessaoudou, R. Mayet, J. Cornette, J. L. Jauberteau, P. Carles and T. Merle-Méjean, *Coatings*, 2015, **5**, 656–687.
- 91 K. Inumaru, K. Baba and S. Yamanaka, *Chem. Mater.*, 2005, **17**, 5935–5940.
- 92 L. Hallett, I. Charaev, A. Agarwal, A. Dane, M. Colangelo, D. Zhu and K. K. Berggren, *Supercond. Sci. Technol.*, 2021, **34**, 035012.
- 93 Y. Zhang, N. Haberkorn, F. Ronning, H. Wang, N. A. Mara, M. Zhuo, L. Chen, J. H. Lee, K. J. Blackmore and E. Bauer, *et al.*, *J. Am. Chem. Soc.*, 2011, **133**, 20735–20737.
- 94 T. Proslier, J. Klug, N. C. Becker, J. W. Elam and M. Pellin, *ECS Trans.*, 2011, **41**, 237.
- 95 K.-E. Elers, M. Ritala, M. Leskelä and E. Rauhala, *Appl. Surf. Sci.*, 1994, **82**, 468–474.
- 96 M. Ritala, T. Asikainen, M. Leskelä, J. Jokinen, R. Lappalainen, M. Utriainen, L. Niinistö and E. Ristolainen, *Appl. Surf. Sci.*, 1997, **120**, 199–212.
- 97 N. Van Hoornick, H. De Witte, T. Witters, C. Zhao, T. Conard, H. Huotari, J. Swerts, T. Schram, J. Maes and S. De Gendt, *et al.*, *J. Electrochem. Soc.*, 2006, **153**, G437.



- 98 P. Alén, M. Ritala, K. Arstila, J. Keinonen and M. Leskelä, *Thin Solid Films*, 2005, **491**, 235–241.
- 99 C. Sheagren, P. Barry, E. Shirokoff and Q. Y. Tang, *J. Low Temp. Phys.*, 2020, **199**, 875–882.
- 100 M. Ziegler, L. Fritzsch, J. Day, S. Linzen, S. Anders, J. Toussaint and H.-G. Meyer, *Supercond. Sci. Technol.*, 2012, **26**, 025008.
- 101 S. Linzen, M. Ziegler, O. Astafiev, M. Schmelz, U. Hübner, M. Diegel, E. Il'ichev and H. Meyer, *Supercond. Sci. Technol.*, 2017, **30**, 035010.
- 102 R. Cheng, S. Wang and H. X. Tang, *Appl. Phys. Lett.*, 2019, **115**(24), 241101.
- 103 C. Lennon, Y. Shu, J. Brennan, D. K. Namburi, V. Varghese, D. Hemakumara, L. Longchar, S. Srinath and R. H. Hadfield, *Mater. Quantum Technol.*, 2023, **3**, 045401.
- 104 M. J. Sowa, Y. Yemane, J. Zhang, J. C. Palmstrom, L. Ju, N. C. Strandwitz, F. B. Prinz and J. Provine, *J. Vac. Sci. Technol., A*, 2017, **35**(1), 01B143.
- 105 M. Shibalov, A. Mumlyakov, I. Trofimov, E. Timofeeva, A. Sirotnina, E. Pershina, A. Tagachenkov, Y. Anufriev, E. Zenova and N. Porokhov, *et al.*, *Supercond. Sci. Technol.*, 2021, **34**, 085016.
- 106 T. Shiino, S. Shiba, N. Sakai, T. Yamakura, L. Jiang, Y. Uzawa, H. Maezawa and S. Yamamoto, *Supercond. Sci. Technol.*, 2010, **23**, 045004.
- 107 E. Knehr, A. Kuzmin, D. Y. Vodolazov, M. Ziegler, S. Doerner, K. Ilin, M. Siegel, R. Stolz and H. Schmidt, *Supercond. Sci. Technol.*, 2019, **32**, 125007.
- 108 M. Williams, K. Ralls and M. Pickus, *J. Phys. Chem. Solids*, 1967, **28**, 333–341.
- 109 L. Toth, *Transition metal carbides and nitrides*, Elsevier, 2014.
- 110 Y. Yemane, M. Sowa, J. Zhang, L. Ju, E. Deguns, N. Strandwitz, F. Prinz and J. Provine, *Supercond. Sci. Technol.*, 2017, **30**, 095010.
- 111 R. Di Leo, A. Nigro, G. Nobile and R. Vaglio, *J. Low Temp. Phys.*, 1990, **78**, 41–50.
- 112 M. C. Burton, M. R. Beebe, K. Yang, R. A. Lukaszew, A.-M. Valente-Feliciano and C. Reece, *J. Vac. Sci. Technol., A*, 2016, **34**(2), 021518.
- 113 Y. Kalboussi, *PhD thesis*, Université Paris-Saclay, 2023.
- 114 B. Warcholinski, A. Gilewicz, T. Kuznetsova, T. Zubar, S. Chizhik, S. Abetkovskaia and V. Lapitskaya, *Surf. Coat. Technol.*, 2017, **319**, 117–128.
- 115 J. Qian, S. Li, J. Pu, Z. Cai, H. Wang, Q. Cai and P. Ju, *Surf. Coat. Technol.*, 2019, **374**, 725–735.
- 116 E. Mohimi, K. Canova, Z. Zhang, S. Liu, J. L. Mallek, G. S. Girolami and J. R. Abelson, *J. Vac. Sci. Technol., A*, 2019, **37**(2), 021503.
- 117 A. Molina, I. E. Campbell, T. N. Walter, A. D. Agyapong and S. E. Mohny, *Appl. Phys. Lett.*, 2021, **119**(10), 102102.
- 118 W. Kang, J. S. Ahn and J. H. Han, *J. Vac. Sci. Technol., A*, 2023, **41**(6), 062401.
- 119 C. Sathish, Y. Guo, X. Wang, Y. Tsujimoto, J. Li, S. Zhang, Y. Matsushita, Y. Shi, H. Tian and H. Yang, *et al.*, *J. Solid State Chem.*, 2012, **196**, 579–585.
- 120 K. Yamaura, Q. Huang, M. Akaishi and E. Takayama-Muromachi, *Phys. Rev. B: Condens. Matter Mater. Phys.*, 2006, **74**, 184510.
- 121 M. K. Kolel-Veetil, S. B. Qadri, M. Osofsky and T. M. Keller, *Chem. Mater.*, 2005, **17**, 6101–6107.
- 122 S. A. Peeters, C. T. Lennon, M. J. Merckx, R. H. Hadfield, W. Kessels, M. A. Verheijen and H. Knoop, *Appl. Phys. Lett.*, 2023, **123**(13), 132603.
- 123 E. Thorwarth, M. Dietrich and C. Politis, *Solid State Commun.*, 1976, **20**, 869–872.
- 124 Y. Yan, Q. Wei, H. Yan, Z. Wu and M. Zhang, *Comput. Mater. Sci.*, 2022, **214**, 111728.
- 125 J. Schaeffer, C. Capasso, R. Gregory, D. Gilmer, L. Fonseca, M. Raymond, C. Happ, M. Kottke, S. Samavedam and P. Tobin, *et al.*, *J. Appl. Phys.*, 2007, **101**(1), 014503.
- 126 T. J. Park, J. H. Kim, J. H. Jang, K. D. Na, C. S. Hwang, J. H. Kim, G.-M. Kim, J. H. Choi, K. J. Choi and J. H. Jeong, *Appl. Phys. Lett.*, 2007, **91**(25), 252106.
- 127 G.-h. Cho and S.-W. Rhee, *Electrochem. Solid-State Lett.*, 2010, **13**, H426.
- 128 C. Hossbach, S. Teichert, J. Thomas, L. Wilde, H. Wojcik, D. Schmidt, B. Adolph, M. Bertram, U. Mühle and M. Albert, *et al.*, *J. Electrochem. Soc.*, 2009, **156**, H852.
- 129 M.-K. Song and S.-w. Rhee, *J. Electrochem. Soc.*, 2008, **155**, H823.
- 130 E. Pechen, S. Krasnosvobodtsev, N. Shabanova, E. Ekimov, A. Varlashkin, V. Nozdrin, A. Tschovrebov and A. Golovashkin, *Phys. C*, 1994, **235**, 2511–2512.
- 131 L. Wu, Y. Wang, Z. Yan, J. Zhang, F. Xiao and B. Liao, *J. Alloys Compd.*, 2013, **561**, 220–227.
- 132 M. Sansone, A. De Bonis, A. Santagata, J. Rau, A. Galasso and R. Teghil, *Appl. Surf. Sci.*, 2016, **374**, 112–116.
- 133 K.-W. Kim, B. J. Kim, S. H. Lee, T. Nasir, H. K. Lim, I. J. Choi, B. J. Jeong, J. Lee, H. K. Yu and J.-Y. Choi, *Coatings*, 2018, **8**, 379.
- 134 C. Zoita, L. Braic, A. Kiss and M. Braic, *Surf. Coat. Technol.*, 2010, **204**, 2002–2005.
- 135 C. Xu, L. Wang, Z. Liu, L. Chen, J. Guo, N. Kang, X.-L. Ma, H.-M. Cheng and W. Ren, *Nat. Mater.*, 2015, **14**, 1135–1141.
- 136 M. K. Kolel-Veetil, S. B. Qadri, M. Osofsky, T. M. Keller, R. Goswami and S. A. Wolf, *J. Phys. Chem. C*, 2007, **111**, 16878–16882.
- 137 L. Toth, E. Rudy, J. Johnston and E. Parker, *J. Phys. Chem. Solids*, 1965, **26**, 517–522.
- 138 N. Athanasiou, *Mod. Phys. Lett. B*, 1997, **11**, 939–947.
- 139 J. Wang, S. Liu, Y. Wang, T. Wang, S. Shang and W. Ren, *J. Mater. Chem. C*, 2020, **8**, 1608–1613.
- 140 C. Tang, H. Zhang, K. Xu, Q. Zhang, J. Liu, C. He, L. Fan and T. Asefa, *J. Mater. Chem. A*, 2019, **7**, 18030–18038.
- 141 J. Lu, H. Hugosson, O. Eriksson, L. Nordström and U. Jansson, *Thin Solid Films*, 2000, **370**, 203–212.
- 142 M.-J. Ha, H. Kim, J.-H. Choi, M. Kim, W.-H. Kim, T. J. Park, B. Shong and J.-H. Ahn, *Chem. Mater.*, 2022, **34**, 2576–2584.
- 143 J. S. Ahn, W. Kang and J. H. Han, *J. Vac. Sci. Technol., A*, 2023, **41**(1), 012405.
- 144 B. Cao, M. Yang, J. Chen, M. Liang, T. Cui and F. Tian, *Mater. Today Commun.*, 2024, **38**, 107666.



- 145 Y. Pan, Y. Lin, Q. Xue, C. Ren and H. Wang, *Mater. Des.*, 2016, **89**, 676–683.
- 146 T. Proslir, J. A. Klug, J. W. Elam, H. Claus, N. G. Becker and M. J. Pellin, *J. Phys. Chem. C*, 2011, **115**, 9477–9485.
- 147 G. Stewart, B. Olinger and L. Newkirk, *Solid State Commun.*, 1981, **39**, 5–9.
- 148 R. Gao, H. Peng, H. Guo and B. Chen, *J. Mater. Process. Technol.*, 2024, **330**, 118488.
- 149 G. Wiech, W. Zahorowski, A. Simunek and O. Sipr, *J. Phys.: Condens. Matter*, 1989, **1**, 5595.
- 150 W. Cheng and C. Lee, *J. Mater. Sci. Lett.*, 1994, **13**, 1204–1205.
- 151 J.-M. Tarascon, L. Greene, W. McKinnon, G. Hull and T. Geballe, *Science*, 1987, **235**, 1373–1376.
- 152 M. K. Wu, J. R. Ashburn, C. J. Torng, P. H. Hor, R. L. Meng, L. Gao, Z. J. Huang, Y. Q. Wang and C. W. Chu, *Phys. Rev. Lett.*, 1987, **58**, 908–910.
- 153 Y. Wang, J. Ying, Z. Zhou, J. Sun, T. Wen, Y. Zhou, N. Li, Q. Zhang, F. Han and Y. Xiao, *et al.*, *Nat. Commun.*, 2018, **9**, 1914.
- 154 S. Muraleedharan, V. Thiruvengatam, S. O. Karayi, K. Karupiah, V. Jawahar and A. M. Ashok, *CrystEngComm*, 2020, **22**, 85–94.
- 155 Y. E. Suyolcu, Y. Wang, F. Baiutti, A. Al-Temimy, G. Gregori, G. Cristiani, W. Sigle, J. Maier, P. A. van Aken and G. Logvenov, *Sci. Rep.*, 2017, **7**, 453.
- 156 M. Wenskat, G. K. Deyu, I. G. Daz-Palacio, R. H. Blick, R. Zierold and W. Hillert, *Supercond. Sci. Technol.*, 2022, **36**, 015010.
- 157 A. Banerjee, R. M. Heath, D. Morozov, D. Hemakumara, U. Nasti, I. Thayne and R. H. Hadfield, *Opt. Mater. Express*, 2018, **8**, 2072–2088.
- 158 J. Knobloch, W. Hartung, H. Padamsee and F. Newman, Proceedings of the 8th Workshop on RF Superconductivity, Padua, Italy, 1997.
- 159 P. Ylä-Oijala, *Part. Accel.*, 1999, **63**, 105–137.
- 160 J. Gunn, *Plasma Phys. Controlled Fusion*, 2012, **54**, 085007.
- 161 A. Streltsov, J.-J. Berthelier, A. Chernyshov, V. Frolov, F. Honary, M. Kosch, R. McCoy, E. Mishin and M. Rietveld, *Space Sci. Rev.*, 2018, **214**, 1–122.
- 162 J. Lorkiewicz, B. Dwersteg, W.-D. Möller, D. Kostin, M. Layalan and A. Brinkmann, *Anti-multipactor TiN coating of RF power coupler components for TESLA at DESY*, Cm-p00047838 technical report, 2004.
- 163 Y. Kalboussi, B. Delatte, S. Bira, K. Dembele, X. Li, F. Miserque, N. Brun, M. Walls, J.-L. Maurice and D. Dragoe, *et al.*, *Appl. Phys. Lett.*, 2024, **124**(13), 134001.
- 164 Y. Kalboussi, S. Dadouch, B. Delatte, F. Miserque, D. Dragoe, F. Eozenou, M. Baudrier, S. Tusseau-Nenez, Y. Zheng and L. Maurice, *et al.*, *J. Appl. Phys.*, 2024, **136**(8), 085306.
- 165 C. M. Natarajan, M. G. Tanner and R. H. Hadfield, *Supercond. Sci. Technol.*, 2012, **25**, 063001.
- 166 F. Marsili, V. B. Verma, J. A. Stern, S. Harrington, A. E. Lita, T. Gerrits, I. Vayshenker, B. Baek, M. D. Shaw and R. P. Mirin, *et al.*, *Nat. Photonics*, 2013, **7**, 210–214.
- 167 A. Vetter, S. Ferrari, P. Rath, R. Alae, O. Kahl, V. Kovalyuk, S. Diewald, G. N. Goltsman, A. Korneev and C. Rockstuhl, *et al.*, *Nano Lett.*, 2016, **16**, 7085–7092.
- 168 B. Korzh, Q.-Y. Zhao, J. P. Allmaras, S. Frasca, T. M. Autry, E. A. Bersin, A. D. Beyer, R. M. Briggs, B. Bumble and M. Colangelo, *et al.*, *Nat. Photonics*, 2020, **14**, 250–255.
- 169 C. Schuck, W. H. Pernice and H. X. Tang, *Sci. Rep.*, 2013, **3**, 1893.
- 170 S.-K. Liao, W.-Q. Cai, W.-Y. Liu, L. Zhang, Y. Li, J.-G. Ren, J. Yin, Q. Shen, Y. Cao and Z.-P. Li, *et al.*, *Nature*, 2017, **549**, 43–47.
- 171 W. H. Pernice, C. Schuck, O. Minaeva, M. Li, G. Goltsman, A. Sergienko and H. Tang, *Nat. Commun.*, 2012, **3**, 1325.
- 172 A. Divochiy, F. Marsili, D. Bitauld, A. Gaggero, R. Leoni, F. Mattioli, A. Korneev, V. Seleznev, N. Kaurova and O. Minaeva, *et al.*, *Nat. Photonics*, 2008, **2**, 302–306.
- 173 C. Schuck, W. Pernice and H. Tang, *Appl. Phys. Lett.*, 2013, **102**(5), 051101.
- 174 Y. P. Korneeva, M. Y. Mikhailov, Y. P. Pershin, N. Manova, A. Divochiy, Y. B. Vakhtomin, A. Korneev, K. Smirnov, A. Sivakov and A. Y. Devizenko, *et al.*, *Supercond. Sci. Technol.*, 2014, **27**, 095012.
- 175 V. B. Verma, A. E. Lita, M. R. Vissers, F. Marsili, D. P. Pappas, R. P. Mirin and S. W. Nam, *Appl. Phys. Lett.*, 2014, **105**(2), 022602.
- 176 P. Luo and Y. Zhao, *Molecules*, 2023, **28**, 6200.
- 177 G. G. Taylor, D. V. Morozov, C. T. Lennon, P. S. Barry, C. Sheagren and R. H. Hadfield, *Appl. Phys. Lett.*, 2021, **118**(19), 191106.
- 178 D. Morozov, A. Banerjee, K. Erotokritou, G. Taylor, N. R. Gemmell, D. Hemakumara, I. Thayne and R. H. Hadfield, *Advanced Photon Counting Techniques XII*, 2018, p. 106590G.
- 179 J. Zmuidzinas, *Annu. Rev. Condens. Matter Phys.*, 2012, **3**, 169–214.
- 180 O. Kennedy, J. Burnett, J. Fenton, N. Constantino, P. Warburton, J. Morton and E. Dupont-Ferrier, *Phys. Rev. Appl.*, 2019, **11**, 014006.
- 181 P. K. Day, H. G. LeDuc, B. A. Mazin, A. Vayonakis and J. Zmuidzinas, *Nature*, 2003, **425**, 817–821.
- 182 N. Bergeal, F. Schackert, M. Metcalfe, R. Vijay, V. Manucharyan, L. Frunzio, D. Prober, R. Schoelkopf, S. Girvin and M. Devoret, *Nature*, 2010, **465**, 64–68.
- 183 Z.-L. Xiang, S. Ashhab, J. You and F. Nori, *Rev. Mod. Phys.*, 2013, **85**, 623–653.
- 184 X. Mi, M. Benito, S. Putz, D. M. Zajac, J. M. Taylor, G. Burkard and J. R. Petta, *Nature*, 2018, **555**, 599–603.
- 185 E. Abe, H. Wu, A. Ardavan and J. J. Morton, *Appl. Phys. Lett.*, 2011, **98**(25), 251108.
- 186 J. T. Hou and L. Liu, *Phys. Rev. Lett.*, 2019, **123**, 107702.
- 187 J.-M. Pirkkalainen, S. Cho, J. Li, G. Paraoanu, P. Hakonen and M. Sillanpää, *Nature*, 2013, **494**, 211–215.
- 188 M. Müller, T. Luschmann, A. Faltermeier, S. Weichselbaumer, L. Koch, G. B. Huber, H. W. Schumacher, N. Ubbelohde, D. Reifert and T. Scheller, *et al.*, *Mater. Quant. Technol.*, 2022, **2**, 015002.





- 189 S. Ohya, B. Chiaro, A. Megrant, C. Neill, R. Barends, Y. Chen, J. Kelly, D. Low, J. Mutus and P. O'Malley, *et al.*, *Supercond. Sci. Technol.*, 2013, **27**, 015009.
- 190 R. Russo, A. Chatel, N. S. Solmaz, R. Farsi, H. Furci, J. Brugger and G. Boero, *Micro Nano Eng.*, 2023, **19**, 100203.
- 191 F. W. Carter, T. Khaire, C. Chang and V. Novosad, *Appl. Phys. Lett.*, 2019, **115**(9), 092602.
- 192 J. Wenner, M. Neeley, R. C. Bialczak, M. Lenander, E. Lucero, A. D. O'Connell, D. Sank, H. Wang, M. Weides and A. N. Cleland, *et al.*, *Supercond. Sci. Technol.*, 2011, **24**, 065001.
- 193 S. K. Tolpygo, V. Bolkhovskiy, T. Weir, L. M. Johnson, W. D. Oliver and M. A. Gouker, *Supercond. Sci. Technol.*, 2014, **27**, 025016.
- 194 M. Kiviranta, O. Brandel, L. Grönberg, J. Kunert, S. Linzen, N. Beev, T. May and M. Prunnila, *IEEE Trans. Appl. Supercond.*, 2016, **26**, 1–5.
- 195 D.-R. W. Yost, M. E. Schwartz, J. Mallek, D. Rosenberg, C. Stull, J. L. Yoder, G. Calusine, M. Cook, R. Das and A. L. Day, *et al.*, *npj Quantum Inf.*, 2020, **6**, 59.
- 196 W. D. Oliver and P. B. Welander, *MRS Bull.*, 2013, **38**, 816–825.
- 197 J. Koch, T. M. Yu, J. Gambetta, A. A. Houck, D. I. Schuster, J. Majer, A. Blais, M. H. Devoret, S. M. Girvin and R. J. Schoelkopf, *Phys. Rev. A: At., Mol., Opt. Phys.*, 2007, **76**, 042319.
- 198 B. Royer, A. L. Grimsom, A. Choquette-Poitevin and A. Blais, *Phys. Rev. Lett.*, 2018, **120**, 203602.
- 199 J. Y. Mutus, T. C. White, R. Barends, Y. Chen, Z. Chen, B. Chiaro, A. Dunsworth, E. Jeffrey, J. Kelly and A. Megrant, *et al.*, *Appl. Phys. Lett.*, 2014, **104**(26), 263513.
- 200 J. B. Hertzberg, E. J. Zhang, S. Rosenblatt, E. Magesan, J. A. Smolin, J.-B. Yau, V. P. Adiga, M. Sandberg, M. Brink and J. M. Chow, *et al.*, *npj Quantum Inf.*, 2021, **7**, 129.
- 201 K. Makise, R. Sun, H. Terai and Z. Wang, *IEEE Trans. Appl. Supercond.*, 2014, **25**, 1–4.
- 202 Y. Zheng, S. Li, Z. Ding, K. Xiong, J. Feng and H. Yang, *Sci. Rep.*, 2023, **13**, 11874.
- 203 A. Dunsworth, A. Megrant, C. Quintana, Z. Chen, R. Barends, B. Burkett, B. Foxen, Y. Chen, B. Chiaro and A. Fowler, *et al.*, *Appl. Phys. Lett.*, 2017, **111**(2), 022601.
- 204 R. Lu, A. J. Elliot, L. Wille, B. Mao, S. Han, J. Z. Wu, J. Talvacchio, H. M. Schulze, R. M. Lewis and D. J. Ewing, *et al.*, *IEEE Trans. Appl. Supercond.*, 2012, **23**, 1100705.
- 205 A. J. Elliot, G. A. Malek, R. Lu, S. Han, H. Yu, S. Zhao and J. Z. Wu, *Rev. Sci. Instrum.*, 2014, **85**(7), 073904.
- 206 A. Gurevich, *Appl. Phys. Lett.*, 2006, **88**(1), 012511.
- 207 S. Posen, M. K. Transtrum, G. Catelani, M. U. Liepe and J. P. Sethna, *Phys. Rev. Appl.*, 2015, **4**, 044019.
- 208 T. Kubo, *Supercond. Sci. Technol.*, 2021, **34**, 045006.
- 209 H. Padamsee, *arXiv*, 2020, preprint, arXiv:2004.06720, DOI: [10.48550/arXiv.2004.06720](https://doi.org/10.48550/arXiv.2004.06720).
- 210 A.-M. Valente-Feliciano, C. Antoine, S. Anlage, G. Ciovati, J. Delayen, F. Gerigk, A. Gurevich, T. Junginger, S. Keckert, G. Keppe *et al.*, *arXiv*, 2022, preprint, arXiv:2204.02536, DOI: [10.48550/arXiv.2204.02536](https://doi.org/10.48550/arXiv.2204.02536).
- 211 A. J. Kreisler and A. Gaugue, *Supercond. Sci. Technol.*, 2000, **13**, 1235.
- 212 T. R. Stevenson, J. S. Adams, W.-T. Hsieh, S. H. Moseley, D. E. Travers, U. Kongpop, E. J. Wollack and J. Zmuidzinas, *et al.*, *IEEE Trans. Appl. Supercond.*, 2009, **19**, 561–564.
- 213 S. Steinhauer, L. Yang, S. Gyger, T. Lettner, C. Errando-Herranz, K. D. Jöns, M. A. Baghban, K. Gallo, J. Zichi and V. Zwiller, *Appl. Phys. Lett.*, 2020, **116**(17), 171101.
- 214 S. Kim, H. Terai, T. Yamashita, W. Qiu, T. Fuse, F. Yoshihara, S. Ashhab, K. Inomata and K. Semba, *Commun. Mater.*, 2021, **2**, 98.
- 215 W. Li, T. Yang and Y. Xin, *IEEE Trans. Appl. Supercond.*, 2024, **3**(5), 1–5.
- 216 A. Cansiz, J. R. Hull, T. M. Mulcahy and B. Lehnndorff, *Adv. Cryog. Eng.*, 2000, 1707–1714.
- 217 J. Niu, L. Zhang, Y. Liu, J. Qiu, W. Huang, J. Huang, H. Jia, J. Liu, Z. Tao and W. Wei, *et al.*, *Nat. Electron.*, 2023, **6**, 235–241.
- 218 X. Ren, J. Li, W.-C. Chen, Q. Gao, J. J. Sanchez, J. Hales, H. Luo, F. Rodolakis, J. L. McChesney and T. Xiang, *et al.*, *Commun. Phys.*, 2023, **6**, 341.
- 219 A. Pogrebnjakov, J. Redwing, S. Raghavan, V. Vaithyanathan, D. Schlom, S. Xu, Q. Li, D. Tenne, A. Soukiassian and X. Xi, *et al.*, *Phys. Rev. Lett.*, 2004, **93**, 147006.
- 220 A. Llordes, A. Palau, J. Gázquez, M. Coll, R. Vlad, A. Pomar, J. Arbiol, R. Guzman, S. Ye and V. Rouco, *et al.*, *Nat. Mater.*, 2012, **11**, 329–336.
- 221 Y. Mei, G. Huang, A. A. Solovov, E. B. Ureña, I. Mönch, F. Ding, T. Reindl, R. K. Fu, P. K. Chu and O. G. Schmidt, *Adv. Mater.*, 2008, **20**, 4085–4090.
- 222 S. Mishra, E. Przewdzicka, W. Wozniak, A. Adhikari, R. Jakiela, W. Paszkowicz, A. Sulich, M. Ozga, K. Kopalko and E. Guziewicz, *Materials*, 2021, **14**, 4048.
- 223 A. R. Akbashev, A. V. Plokhikh, D. Barbash, S. E. Lofland and J. E. Spanier, *APL Mater.*, 2015, **3**, 106102.
- 224 J. Paglione and R. L. Greene, *Nat. Phys.*, 2010, **6**, 645–658.
- 225 J. A. Flores-Livas, L. Boeri, A. Sanna, G. Profeta, R. Arita and M. Eremets, *Phys. Rep.*, 2020, **856**, 1–78.
- 226 A. W. Sleight, *Science*, 1988, **242**, 1519–1527.
- 227 D. J. Mandia, A. Yanguas-gil, D. Choudhury, A. Nassiri, A. U. Mane and J. W. Elam, *Methods for low-temperature p-CVD and thermal ALD of magnesium diboride*, *US Pat.*, 11773488, 2023.

